Charged Current Top Quark Couplings at the LHC

Dissertation zur Erlangung des naturwissenschaftlichen Doktorgrades der Bayerischen Julius-Maximilians-Universität Würzburg

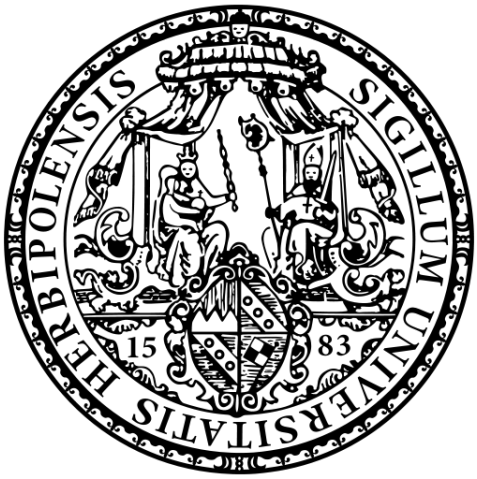

vorgelegt von

Fabian Bach

aus Meiningen

Würzburg 2013

Zusammenfassung

Das Top-Quark spielt eine wichtige Rolle in der aktuellen Teilchenphysik, sowohl aus theoretischer Sicht aufgrund seiner einzigartig großen Masse, aber auch aus experimenteller Sicht wegen der großen Anzahl an Top-Ereignissen, die von den LHC-Experimenten ATLAS und CMS bereits aufgezeichnet wurden. Diese ermöglichen direkte Messungen der Eigenschaften dieses Teilchens, zum Beispiel seine Kopplungen an die anderen Teilchen des Standardmodells (SM), mit einer bis dato unerreichten Genauigkeit. In der vorliegenden Arbeit wird ein Zugang mittels effektiver Feldtheorie verwendet, um eine minimale und konsistente Parametrisierung aller anomalen Top-Kopplungen an die Eichbosonen und Fermionen des SM zu finden, die mit allen SM-Symmetrien kompatibel ist. Zudem werden verschiedene Aspekte und Konsequenzen der zugrundeliegenden Operatorrelationen für diese Kopplungen diskutiert.

Der resultierende Satz von Kopplungen wurde in den Monte Carlo-Ereignisgenerator WHIZARD implementiert, um einen quantitativen Zugang zu den phänomenologischen Implikationen an aktuellen und zukünftigen Teilchenbeschleunigern wie dem LHC oder einem geplanten internationalen Linearbeschleuniger zu ermöglichen. Der phänomenologische Teil dieser Arbeit konzentriert sich auf die geladenen Stromkopplungen des Top-Quarks, beziehungsweise anomale Beiträge zur trilinearen tbW-Kopplung wie zur quartischen Kontaktwechselwirkung der Form $tbff'$, die Einfluss auf die Produktion einzelner Top-Quarks sowie auf deren Zerfall am LHC haben. Die Studie umfasst verschiedene Aspekte der Messung inklusiver Wirkungsquerschnitte, aber auch differentieller Verteilungen einzelner Top-Quarks, die entweder im t-Kanal, $bq \to tq'$, oder im s-Kanal, $u\bar{d} \to t\bar{b}$, produziert wurden. Diskutiert werden sowohl die Modellierung dieser Prozesse auf Parton-Ebene als auch Detektoreffekte, um schließlich zu einer Abschätzung der voraussichtlichen Ausschlussgrenzen des LHC an solche Kopplungen mit 10 bzw. $100\,\mathrm{fb}^{-1}$ an aufgezeichneten Daten bei $\sqrt{s} = 14\,\mathrm{TeV}$ zu kommen.

Abstract

The top quark plays an important role in current particle physics, from a theoretical point of view because of its uniquely large mass, but also experimentally because of the large number of top events recorded by the LHC experiments ATLAS and CMS, which makes it possible to directly measure the properties of this particle, for example its couplings to the other particles of the standard model (SM), with previously unknown precision. In this thesis, an effective field theory approach is employed to introduce a minimal and consistent parametrization of all anomalous top couplings to the SM gauge bosons and fermions which are compatible with the SM symmetries. In addition, several aspects and consequences of the underlying effective operator relations for these couplings are discussed.

The resulting set of couplings has been implemented in the parton level Monte Carlo event generator WHIZARD in order to provide a tool for the quantitative assessment of the phenomenological implications at present and future colliders such as the LHC or a planned international linear collider. The phenomenological part of this thesis is focused on the charged current couplings of the top quark, namely anomalous contributions to the trilinear tbW coupling as well as quartic four-fermion contact interactions of the form $tbff'$, both affecting single top production as well as top decays at the LHC. The study includes various aspects of inclusive cross section measurements as well as differential distributions of single tops produced in the t channel, $bq \to tq'$, and in the s channel, $u\bar{d} \to t\bar{b}$. We discuss the parton level modelling of these processes as well as detector effects, and finally present the prospected LHC reach for setting limits on these couplings with 10 resp. $100\,\mathrm{fb}^{-1}$ of data recorded at $\sqrt{s} = 14\,\mathrm{TeV}$.

Contents

Introduction

In accord with nearly every other article or thesis in the field of particle physics published within the past two or three decades, the beginning of this thesis shall be devoted to the success of the standard model of particle physics (SM), not because of social convention but rather because the SM actually deserves and still goes on living up to its outstanding reputation. Since its formulation by Glashow, Salam and Weinberg in the 1960s [1–3], science history is laced with milestones of experimental evidence for its explanatory as well as predictive power, most prominently the various discoveries of new particles that had been predicted by the SM beforehand. For instance, the implementation of the unified electroweak interaction via a spontaneously broken $\mathbf{SU}(2) \times \mathbf{U}(1)$ gauge symmetry immediately implied the existence of a triplet of heavy gauge bosons $W^{\pm}$ and Z^0, all of which were discovered in the 1980s [4–6]. Similarly, considering the corresponding matter representations which require the left-handed spinors to come in $\mathbf{SU}(2)$ doublets has lead to the postulation of the charm quark as a partner for the strange quark, thus accounting for the suppression of flavor-changing neutral currents (FCNC) via the famed GIM mechanism [7]—experimental confirmation followed already in 1974 with the discovery of the J/Ψ meson [8, 9].

Along the same line of argument, the discovery of the bottom quark in 1977 [10] would make everyone expect a sixth quark to be around the corner to complete the third family doublet, and again this consequence of the SM was confirmed when the top quark was found at the Tevatron in 1995 [11, 12], although turning out to be much heavier than expected. While of course the Tevatron results have further improved until its final shutdown in 2011 [13–16], main attention is now directed towards the LHC which until now has already collected considerable datasets at center-of-mass energies of $\sqrt{s} = 7$ and 8 TeV, respectively. Consequently, top pair production has already been measured in various channels by the LHC multi-purpose experiments ATLAS and CMS with remarkable accuracy [17–22], while single top signals are already established in associated tW production $bg \to tW$ [23, 24] and even definitely observed in the dominant t channel production $bq \to tq'$ [25–27].[1]

Finally, it was just one year ago, and with considerable media attention, when ATLAS and CMS claimed their discovery of a new bosonic resonance around 125 GeV [29, 30], which might indeed be the sole remaining cornerstone of the SM, namely the field excitation of the symmetry breaking scalar sector as proposed by Higgs and others in 1964 [31–34]: the Higgs boson. Although the true nature of the resonance remains unresolved until its exact properties are determined at the LHC (maybe even until a subsequent specially designed collider will be available), first results

[1] It was only very recently that Tevatron's DØ experiment has for the first time claimed evidence of an s channel signal above the 3σ level [28].

tend toward a higgs-like nature. However, the imminent triumph of the SM consists not only of merely containing an appropriate particle, but of providing also a powerful machinery to probe the overall consistency via high precision indirect observables relating the Higgs mass to other model parameters such as the top mass and the broken elektroweak sector.

However, this looming triumph of an almost 50 year old theory, in combination with the continued absence of hints to new physics beyond the SM (BSM) at the LHC, might arguably be considered an even more unsatisfying situation than its actual breakdown, because all the notorious shortcomings of the SM, e. g. the hierarchy problem or the fundamental nature of dark matter, would remain obscure at least within reach of the LHC. Therefore, it is all the more important to go on and refine the searches for deviations from the SM predictions in the whole range of accessible observables. From this point of view, the two latest discoveries, namely the top and the new boson from now on denoted Higgs for brevity, should be regarded not only as a confirmation of the SM, but rather as the most prominent messengers of its possible breakdown, because they are both very massive and hence most likely to "see" any BSM physics around the corner. Furthermore, the top stands out among the matter content of the SM because of its uniquely large mass of the order of the electroweak breaking scale, $m_t \sim v \sim \mathcal{O}(100\,\mathrm{GeV})$, which implies a Yukawa coupling of natural size ~ 1 to the symmetry breaking scalar sector.

One of the questions at the core of this topic is whether the top is indeed the fundamental particle specified by the SM or already a BSM messenger, e. g. a specific representation of an extended electroweak gauge sector or a composite state mixing with an extended symmetry breaking sector, cf. e. g. [35–37]. It was already stated that such new structures could manifest themselves indirectly by small deviations from the properties predicted by the SM, for example anomalous couplings to the other SM particles. While anomalous top–Higgs couplings might first appear as most interesting in this respect, corresponding direct observables suffer greatly from the poor production cross sections at the LHC for Higgs associated single top or top pair production. Therefore, the ttH sector will be discussed during the theoretical part of this thesis, whereas the phenomenological part will be focused on anomalous top couplings to the SM gauge bosons, and among those particularly the charged-current (CC) interaction tbW and associated contact terms $tbff'$, which can be probed directly in all variations of single top production as well as top decays.

In this context, the question must be addressed which kinds of deviations from the SM should reasonably be taken into account at all. The criterion is of course their compatibility at low energies around the Z mass and below with all the global and local symmetries of the SM, which must be incorporated in any new theory as a low energy limit to comply with the plethora of existing experimental bounds in this range. Therefore, a theoretical approach to study such small deviations or anomalies should preferably convey systematic instructions to construct and parametrize observables in accordance with this mandatory criterion. Effective field theory represents a powerful framework in this context, because any observable effects are motivated and at the same time parametrized by effective operators at the Lagrangian level and corresponding Wilson coefficients. These can be systematically

constructed out of the SM field content according to the SM symmetry paradigms and expanded in powers of a heavy new physics scale Λ, thus combining the advantages of being model-independent with respect to the nature of the massive new degrees of freedom while at the same time delivering a natural notion of the quantitative size, and hierarchy, of the contributions to observables. Moreover, considering a fixed effective operator basis facilitates the identification and exploitation of possible operator interrelations imposed by the underlying symmetries and consistency requirements, in order to relate the derived observables and reduce the number of independent parameters in the analysis. Based on the original work by Buchmüller and Wyler, who were the first to present a systematic list and classification of all effective operators parametrizing the leading BSM terms of order Λ^{-1} and Λ^{-2} in 1985 [38], considerable efforts by various authors have gone into the task of finding an optimal—that is most general and yet minimal and consistent—operator basis for an anomalous top sector within the effective theory approach [39–49]. At the heart of most of the arguments is the theorem [50–54] that the equations of motion (EOM) may safely be applied at a fixed order in Λ, and thus be utilized to identify and eliminate redundancies in the operator basis, with errors appearing only at higher orders of Λ.[2]

In this work, we will review in more detail the foundations and features of the effective theory approach, its use to formulate an anomalous top sector and subsequent application of the EOM to identify operator relations and redundancies. Special care will be devoted to the last part which includes drawing conclusions on the number of independent parameters or operator coefficients, because the EOM necessarily generate four-fermion contact interactions (cf. e. g. [45, 46]), and, as has been argued in [55] and will also be further clarified later on, the arguments to drop them from an analysis of anomalous *trilinear* couplings are questionable. Hence, close attention must be paid to the distinction of re*writing* and re*defining* an operator basis and, rather than prematurely disposing of possibly important coupling structures, we will use the rewritten operator set as an optimal starting point for an implementation in the tree level Monte Carlo generator Whizard [56], so that all anomalous couplings which are related to each other by operator coefficients can be probed quantitatively in direct collider observables. Having this toolbox at hand, the phenomenological part will be devoted to Monte Carlo studies of anomalous CC couplings of the top in single top production in the s and t channel, including the modelling of these processes at parton level with Whizard as well as final state reconstruction at detector level, using Pythia 6 [57] for showering and hadronization and Delphes [58, 59] for a fast detector simulation. For the anomalous contributions to the trilinear tbW vertex, special attention will be paid to the interplay of production and decay insertions at matrix element level, also quantifying the repercussions on the coupling limits derived from total cross section measurements. Finally, a study including also the differential distributions in single top events will be presented in order to assess and distinguish the quartic contact interactions of the form $tbff'$, which might affect the top CC sector along with the trilinear ones.

[2] Cf. [49], where this procedure is systematically employed to remove the remaining redundancies in the original list [38] and present a conclusive operator list.

1. Effective Field Theory

1.1. From Fermi Theory to the Standard Model

As an introduction to the topic of effective field theory (EFT), the first section is devoted to a short review of a specific historical example, namely the Fermi theory formulated by Enrico Fermi in 1934 [60] to incorporate the weak charged-current interactions into the particle physics framework. It is well suited to illustrate the construction principles, theoretical merits, and limitations of the general approach, before addressing it more systematically.

1.1.1. Construction

Although this is not strictly following the actual historical development (which would be far beyond the scope of this little interlude), let us assume as initial setting the state of the art in the 1940s, when thanks particularly to R. P. Feynman particle physicists had gained a well-founded understanding of electromagnetism in terms of a relativistic quantum field theory, namely quantum electrodynamics (QED). It employs the principle of local or gauge symmetry to implement the fundamental interaction among charged particles (electrons e, muons μ and protons p at that time, all of them fermions with spin $\frac{1}{2}$) via the exchange of the corresponding gauge field excitations, namely the photons which are vector bosons of spin 1. On the other hand, nuclear interactions could also be described field-theoretically on the basis of H. Yukawa's model, identifying the pseudoscalar pion triplet $\pi^{0,\pm}$ (spin 0) as messenger particles exchanged among the nucleons (the p and the neutron n). However, there was the β decay of neutrons and muons,

$$n \to p^+ e^- \bar{\nu}_e \qquad \text{resp.} \qquad \mu^- \to e^- \bar{\nu}_e \nu_\mu \,, \tag{1.1}$$

introducing new uncharged fermions called neutrinos ν purely to fix momentum and lepton number conservation (after W. Pauli). This interaction still stood apart from the other fundamental interactions known at that time, and it needed Fermi's idea of 1934 [60] to properly incorporate it into theory.

At this point, the layout of the argument will be restricted to the lepton sector, treating the μ decay only, because the basic procedure is independent of the particular type of fermions, and the application to nucleons is straightforward. In terms of a Lagrangian formulation, the theory can be written as

$$\mathcal{L}_{\text{Fermi}} = \mathcal{L}_{\text{QED}} + \Delta\mathcal{L} \,, \tag{1.2}$$

where the term $\Delta\mathcal{L}$ is to be constructed to account for the μ decay, Eq. (1.1), and

$\mathcal{L}_{\text{QED}}$ is the well known QED Lagrangian,

$$\mathcal{L}_{\text{QED}} = \overline{\Psi}\left(\mathrm{i}\not{D} - m_\Psi\right)\Psi - \frac{1}{4}F_{\mu\nu}F^{\mu\nu} \tag{1.3a}$$

$$\equiv \overline{\Psi}\left(\mathrm{i}\not{\partial} - m_\Psi\right)\Psi + \mathrm{e}A_\mu J^\mu_{\text{Q}} - \frac{1}{4}F_{\mu\nu}F^{\mu\nu}\ , \tag{1.3b}$$

with lepton flavors $\Psi = e, \mu, \nu_e, \nu_\mu$ implicitly summed over, the electromagnetic coupling constant e and the field strength $F_{\mu\nu}$ of the corresponding gauge field A_μ (cf. appendix A for details). The Lagrangian (1.3) is by construction invariant under a local $\mathbf{U}(1)$ phase transformation, and Eq. (1.3b) illustrates how this local or gauge invariance implements an interaction term by coupling the gauge field to the electromagnetic current

$$J^\mu_{\text{Q}} = \overline{\Psi}\gamma^\mu Q\Psi = -\bar{e}\gamma^\mu e\ , \tag{1.4}$$

which is indeed the Noether current associated with the conserved $\mathbf{U}(1)$ charge, decomposing the fermions into charged leptons $e \equiv e, \mu$ ($Q = -1$), and the uncharged and hence decoupled neutrinos ν.

Turning to $\Delta\mathcal{L}$, and keeping the electromagnetic vector current coupling in mind, it was Fermi's original idea to couple such currents directly to each other in an invariant way, thus introducing Lagrangian terms which parametrize four-fermion contact interactions. The remaining exercise was to write down all vector currents which might be constructed out of the fermionic degrees of freedom at hand. In this context, it must be noted that the fermion fields further decompose into substates of definite chirality:

$$\Psi_{L,R} = P_{L,R}\Psi = \frac{1 \mp \gamma_5}{2}\Psi\ , \tag{1.5}$$

which becomes equal to the spin alignment or helicity in the massless limit, hence the notation convention referring to "left-handed" and "right-handed" fermions $\Psi_{L,R}$. The main task historically was to infer the correct chiral structure of the new currents by analyzing angular distributions, but for reasons of brevity we will take a shortcut directly to the correct answer: the β decay calls for the existence of charged currents, which come in the purely left-handed form

$$J^+_\mu = \frac{1}{\sqrt{2}}\bar{e}_L\gamma_\mu\nu_L \qquad \text{and} \qquad J^-_\mu = J^{+\dagger}_\mu\ , \tag{1.6}$$

but there is no symmetry principle forbidding the existence also of additional neutral currents apart from J^μ_Q:

$$J^0_\mu = \bar{e}\gamma_\mu\left(\sin^2\theta_w - \frac{1}{2}P_L\right)e + \overline{\nu}_L\gamma_\mu\nu_L \tag{1.7}$$

with the Weinberg angle θ_w addressed in detail in Sec. 1.1.3, together with a physical motivation for the particular shape of Eqs. (1.6) and (1.7). Now $\Delta\mathcal{L}$ can finally be written down in the form

$$\Delta\mathcal{L} = 4\sqrt{2}G_F\left(J^+_\mu J^{-\mu} + J^0_\mu J^{0\mu}\right) \tag{1.8}$$

introducing the Fermi constant G_F, which determines the overall strength of the new interactions.[1] From dimensional analysis, $[\mathcal{L}] = 4$ and $[\Psi] = \frac{3}{2}$, one finds $[G_F] = -2$.

Eq. (1.2) together with Eq. (1.8) can now be used to derive scattering amplitudes accounting for elementary QED as well as weak processes, and the results give a reasonably precise picture of particle physical processes observed at "low" energies well below $\sim 100\,\mathrm{GeV}$. For instance, apart from β decay it accounts for neutrino scattering off fixed atomic targets with a charged lepton in the final states (once colored fermions are included in the theory, after discovery of the nucleon substructure). Furthermore, the neutral current, Eq. (1.7), predicts a deviation from pure QED, e. g. a neutral-current interaction also of the neutrinos, and was thus discovered experimentally long before the actual Z resonance. Conversely, its existence gave a clue as to what symmetry group should be considered to formulate a more fundamental theory out of (1.2) (this thread is resumed in Sec. 1.1.3).

1.1.2. Unitarity and Renormalizability

After mentioning the achievements of Fermi theory in the previous section, its drawbacks and limitations shall now also be addressed. The root of the problem is the mass dimension of the coupling constant, $[G_F] = -2$, or rather of the new operator associated with it, $[J^2] \sim [\Psi^4] = 6$. Because of the lack of other dimensionful structures, the numerator must be governed by the inflow of external momenta of the scattering process, so the respective scattering amplitude will behave like $\sim G_F\, s$, i. e. grow quadratically with the process energy. While this is no problem at small scales, it leads to the breakdown of the theory at sufficiently high energies.

As a first handle on the validity limit of the theory, one can study the scattering amplitudes in terms of unitarity, or probability conservation, at high energies. For example considering the scattering process $e\overline{\nu}_e \to \mu\overline{\nu}_\mu$, the corresponding tree-level Feynman amplitude reads

$$\mathcal{M}(s,\theta) = 2\sqrt{2}G_F\big(\overline{v}(p_{\nu_e})\gamma_\mu P_L u(p_e)\big)\big(\overline{u}(p_\mu)\gamma^\mu P_L v(p_{\nu_\mu})\big)\ , \tag{1.9}$$

employing Dirac spinors u, v with respective momenta. Due to 4-momentum conservation and on-shell conditions, $2 \to 2$ amplitudes generally depend only on two kinematic parameters, here chosen as s and the polar angle in the center-of-mass frame θ. While it is perfectly clear that $\mathcal{M}$ will at some time run into its unitarity limit, one can perform a partial wave analysis to quantify this limit. In terms of the spherical harmonics $P_\ell(\cos\theta)$ labeled by the angular momentum value ℓ, $\mathcal{M}$ can be expanded as

$$\mathcal{M}(s,\theta) = 32\pi \sum_\ell a_\ell(s)(2\ell+1)P_\ell(\cos\theta) \tag{1.10}$$

with partial wave coefficients a_ℓ given by

$$a_\ell(s) = \frac{1}{32\pi}\int_{-1}^{1} \mathrm{d}(\cos\theta)\mathcal{M}(s,\theta)P_\ell(\cos\theta)\ . \tag{1.11}$$

[1] Coincidentally, the contraction of two left-handed bilinears is invariant under Fierz rearrangements, cf. Eq. (B.10), so the chiral structure of the Fermi interaction is uniquely parametrized by Eq. (1.8).

Intuitively it is clear that each a_ℓ must be bounded from above in order to comply with the unitarity requirement for every partial wave. The exact unitarity condition can be looked up in any textbook of choice (e. g. [61]), and reads

$$|a_\ell(s) - \mathrm{i}/2| = 1/2 \,, \tag{1.12}$$

particularly implying $\mathrm{Re}(a_\ell) \leq 1/2$. In the case of the amplitude considered here, Eq. (1.9), this limit is saturated for the s-wave ($\ell = 0$) at $\sqrt{s} \simeq 600\,\mathrm{GeV}$, which is a first physical benchmark for the breakdown scale of the leading order approximation at least.

However, this is not yet a fundamental obstruction to the high-energy validity of the full theory, since it was so far considered only at tree level. If there is a consistent notion of higher perturbative orders, i. e. it is renormalizable, tree-level non-unitarity could just as well imply a strongly coupled theory at a certain scale, which would lead to the invalidity of the perturbation expansion, but not necessarily of the theory itself. For instance, pure QED is manifestly renormalizable in the sense that all infinities from divergent amplitudes at higher orders can be absorbed into the bare Lagrangian parameters (the coupling constant e and fermion masses) by the introduction of just a finite number of counterterms. As a result, one finds physically meaningful renormalized parameters at each perturbative order, which encode all higher-order effects in a residual scale dependence (the renormalization scale). Including the Fermi interaction at one loop order, the coupling constant G_F receives corrections of the form

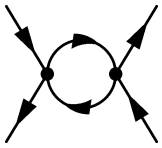

$$\sim \int \frac{\mathrm{d}^4 p}{(4\pi)^2} \frac{\mathrm{tr}[\not{p}\not{p}]}{p^4} \sim \int_0^{\Lambda_\mathrm{UV}} \mathrm{d}p\, p \sim \Lambda_\mathrm{UV}^2 \tag{1.13}$$

from power counting, introducing the cutoff scale Λ_UV. While this divergence alone could formally be fixed by a four-fermion counterterm and hence be absorbed into the bare G_F, one finds yet more divergent amplitudes at one loop level, e. g.

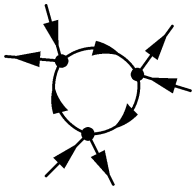

$$\sim \Lambda_\mathrm{UV} \tag{1.14}$$

which requires an additional six-fermion counterterm and a new constant to be absorbed. Similarly, going to ever higher orders the theory will generate an arbitrary number of divergent diagrams which eventually cannot be renormalized by just a finite number of Lagrangian parameters: it is non-renormalizable. At this point latest it is clear that Fermi theory can only be an effective approach to describe a restricted phenomenological pattern in a certain energy range. However, its merits are not confined only to the phenomenological power pointed out in Sec. 1.1.1, because the construction principles of the Fermi interaction already contain hints for the search of a larger theory mending the limitations integral to Fermi theory.

1.1.3. The Standard Model

When trying to address the flaws of Fermi theory, it is fruitful to recollect how the electromagnetic interaction has been implemented in QED in a renormalizable way, namely the principle of gauge invariance, where interaction terms are generated by the conservation laws in the form of Noether currents coupling to the gauge field. The second step already lies within the construction of the Fermi interaction itself, where new vector currents $J^\mu_\pm$ (leaving J^μ_0 aside for another moment) were written down in addition to the QED one J^μ_Q in order to account for the phenomenological need for charged currents. Putting these notions together, the remaining task already seems obvious (as it always does by the time the correct answer has long been textbook knowledge): just find the right symmetry group, put the matter into the correct representations, and gauge it to have Yang-Mills theory do the rest of the job (cf. appendix A).

However, so far this is only half of the answer needed from Fermi phenomenology, because it is still not clear why the interaction is so weak, respectively how the large scale $\sim 1/\sqrt{G_F}$ is created within the theory. Conversely, additional gauge symmetries introduce new *massless* vector bosons which must hence be present in the spectrum at any scale, just like the photon. Since this is not the case, the new bosons must be massive, requiring the corresponding symmetry to be broken down again to the exact remaining $\mathbf{U}(1)_{\text{QED}}$. Specifically, the Fermi interaction must be replaced by Feynman rules such that the corresponding charged-current diagram, Eq. (1.9), at tree level becomes

$\mathcal{M}(e\overline{\nu}_e \to \mu\overline{\nu}_\mu) =$ 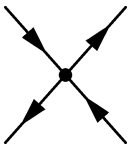 $\to$ 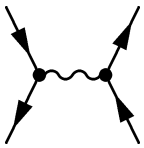 $\sim \dfrac{1}{p^2 - M^2}$ (1.15)

with a new charged gauge boson (call it W^-) of mass M propagating with momentum p in the s channel. This way, at low energies $p^2 \equiv s \ll M^2$ the boson is removed from the dynamic degrees of freedom, and one can identify

$$G_F \sim \frac{g^2}{M^2} \,, \tag{1.16}$$

introducing a new gauge coupling g. (At tree level, obviously. For a more accurate account of this "matching" of parameters, cf. Sec. 1.2.2.) On the other hand, at high energies $s \gg M^2$ the new propagator will heal the bad energy behavior of Eq. (1.9).

Now turning to the actual symmetry group realized in nature, it was S. Glashow who in 1961 proposed a minimal solution [1] to account for the charged currents by way of a $\mathbf{SU}(2)$ broken down to its diagonal τ_3 which generates the $\mathbf{U}(1)$ phase transformations of QED, in order to convey just the heavy $W^\pm$ needed to couple to the $J_\pm$. However, as already mentioned in Sec. 1.1.1, there is no fundamental argument against the existence of weak neutral interactions $\sim J_0$. Their eventual discovery [62] required at least one additional symmetry generator for phase transformations (and hence a massive neutral gauge boson Z), finally leading to the electroweak gauge

group of the SM: $\mathbf{SU}(2)_L \times \mathbf{U}(1)_\Upsilon$, as written down by Weinberg [2] and Salam [3] in 1968. The indices refer to the fact that only the left-handed fermions are charged under the $\mathbf{SU}(2)_L$ in order to comply with the maximally parity violating nature of the charged-current processes, while Υ denotes the hypercharge needed to adjust the neutral couplings such that QED is found again after symmetry breaking.

In order to construct the Lagrangian in an invariant way before symmetry breaking, one introduces new, a priori massless gauge fields $W^\mu \equiv \vec{W}^\mu \cdot \vec{\tau}$ gauging the $\mathbf{SU}(2)_L$ with coupling g ($2\vec{\tau}$ being the set of Pauli matrices), and B^μ gauging the $\mathbf{U}(1)_\Upsilon$ with coupling g':

$$\mathcal{L}_{\text{gauge}} = -\frac{1}{4}\vec{W}^{\mu\nu} \cdot \vec{W}_{\mu\nu} - \frac{1}{4}B^{\mu\nu}B_{\mu\nu} \tag{1.17}$$

(cf. appendix A). Symmetry breaking can now be parametrized without spoiling the invariance of the Lagrangian itself by the introduction of a new field Φ with a nontrivial vacuum expectation value (vev) υ, and carrying the correct quantum numbers such that the other fields can be coupled to it in a renormalizable way, i. e. with dimensionless coupling constants. The most straightforward way is to take a Lorentz scalar in a specific representation of the gauge group: for instance, one could choose the minimal representation in terms of additional parameters,

$$\Phi(x) = \sqrt{2}\upsilon \exp(-\tfrac{\mathrm{i}}{\upsilon}\vec{\tau} \cdot \vec{\pi}(x)) \equiv \Sigma(x)\ , \tag{1.18}$$

i. e. unitary 2×2 matrices with $\Sigma^\dagger\Sigma = 2\upsilon^2$ everywhere, and three real parameters $\vec{\pi}(x)$ (cf. the Nonlinear Sigma Model, e. g. in [63]). These are the Goldstone bosons of the broken symmetry generators. While symmetry breaking is manifest in this representation, making it model-independent in the sense that no assumptions are made on the actual dynamics of the breaking mechanism, it is also non-renormalizable because interactions with arbitrarily many external legs are generated already at the tree level. On the other hand, the minimal linear representation is a complex doublet,

$$\Phi(x) = \frac{1}{\sqrt{2}}\begin{pmatrix} \pi_1(x) + \mathrm{i}\pi_2(x) \\ (\upsilon + h(x)) + \mathrm{i}\pi_3(x) \end{pmatrix} \equiv \phi(x) \tag{1.19}$$

with an additional real degree of freedom $h(x)$ requiring a new scalar particle in the spectrum. In this case, the finite vev can be motivated dynamically by a potential $V(\phi)$ with nontrivial minima. Again, if one asks for the minimal way to accomplish this, then $V(\phi) \sim \phi^4$, which just means adding a ϕ^4 sector to the Lagrangian:

$$\begin{aligned} \mathcal{L}_{\text{scalar}} &= (D_\mu\phi)^\dagger(D^\mu\phi) + \mu^2\phi^\dagger\phi - \lambda(\phi^\dagger\phi)^2 \\ &\text{with } D_\mu = \partial_\mu - \mathrm{i}g\vec{\tau} \cdot \vec{W}_\mu - \mathrm{i}g'\Upsilon B_\mu\ , \end{aligned} \tag{1.20}$$

where the sign of μ^2 breaks the symmetry, leading to a nontrivial minimum $|\phi| = |\mu|/\sqrt{\lambda} \equiv \upsilon$. This is essentially the Higgs mechanism in its classic form [31, 32]. Although it was argued that Eq. (1.18) represents a more model-independent account of symmetry breaking, the recent discovery of a very probably scalar resonance at the LHC [29, 30] favors this version, Eq. (1.19), over Eq. (1.18), and will hence be adopted in the further course of this thesis.

Note that there is always the freedom to fix the gauge such that $\vec{\pi} = 0$ everywhere, making the Goldstone bosons vanish from the spectrum. In this gauge, called *unitarity gauge*, the ground state vector is $\langle\phi\rangle = (0, v)^T$, and inserting it into the kinetic part of Eq. (1.20) generates bilinear, i. e. mass terms for the gauge bosons (after setting the φ hypercharge to $\Upsilon = 1/2$):

$$\mathcal{L}_{\text{scalar}} \sim \frac{v^2}{4}\left[g^2\sum_{i=1}^{2} W_{i\mu}W_i^\mu + (W_{3\mu}, B_\mu)\begin{pmatrix} g^2 & -gg' \\ -gg' & g'^2 \end{pmatrix}\begin{pmatrix} W_3^\mu \\ B^\mu \end{pmatrix}\right] \tag{1.21a}$$

$$\sim m_W^2 W_\mu^+ W^{-\mu} + \frac{1}{2}m_Z^2 Z_\mu Z^\mu \,, \tag{1.21b}$$

where in the second line the bilinear terms were diagonalized in the eigenstates of mass and charge,

$$W^\pm = \frac{1}{\sqrt{2}}(W_1 \mp \mathrm{i}W_2) \,, \quad Z = c_w W_3 - s_w B \,, \quad A = s_w W_3 + c_w B \tag{1.22}$$

with corresponding eigenvalues

$$m_W = \frac{gv}{2} \qquad \text{and} \qquad m_Z = \frac{m_W}{c_w} \tag{1.23}$$

in addition to the massless photon. The factors $\sin\theta_w \equiv s_w$ and $\cos\theta_w \equiv c_w$ are given by the Weinberg angle θ_w defined as

$$\tan\theta_w \equiv \frac{g}{g'} \,, \tag{1.24}$$

which was already used in Eq. (1.7) to parametrize the neutral current, and now gets a deeper physical meaning as the mixing parameter of the two neutral gauge degrees of freedom.

It remains to couple the matter fields to the scalar field ϕ in order to also generate the fermion masses in a gauge invariant way. To that end, one should first fix the quantum numbers of the fermions by analyzing their gauge interactions. These are obtained by rewriting the covariant derivate, cf. Eq. (1.20), in terms of the physical vector boson states and inserting it into the massless matter Lagrangian, Eq. (A.3) with $m_\Psi = 0$. This yields

$$\mathcal{L}_{\text{matter}} = \mathcal{L}_{\text{Dirac}} + g\left(W_\mu^+ J^{-\mu} + W_\mu^- J^{+\mu} + \frac{1}{c_w}Z_\mu J_0^\mu + s_w A_\mu J_Q^\mu\right) \,, \tag{1.25}$$

where the current coupling to the massless A_μ has been identified with the electromagnetic J_Q (implying $gs_w \equiv \mathrm{e}$), so that all the currents are exactly the same as those already introduced in Sec. 1.1.1. The hypercharge Υ of the fermions is thus determined by the relation

$$Q = \tau_3 + \Upsilon \,, \tag{1.26}$$

where the $\mathbf{SU}(2)_L$ charge τ_3 is fixed by chirality, $\tau_3\Psi_L = \pm\frac{1}{2}\Psi_L$ and $\tau_3\Psi_R = 0$, in order to generate the parity violating charged currents, while Q must evaluate to the

usual electromagnetic charge. It is now straightforward to write down the scalar–fermion interaction terms in the spirit of Yukawa theory by combining the right gauge group representations into singlets:

$$\mathcal{L}_{\text{Yukawa}} \sim Y_e \left(\bar{\ell}_L \cdot \phi\right) e_R + \text{h.c.} \xrightarrow{\langle\phi\rangle} m_e \bar{e} e \quad \text{with } m_e = \frac{Y_e v}{\sqrt{2}} \,, \tag{1.27}$$

where the left-handed leptons have been put into $\mathbf{SU}(2)_L$ doublets, $\ell_L = (\nu_L, e_L)^T$, and the Yukawa coupling Y_e can be chosen diagonal in flavor space because of the absence of neutrino masses. At this point, it makes sense to include the quark fields into the discussion, extending the flavor list Ψ by up-type flavors $u = u, c, t$ ($Q = 2/3$) and down-type flavors $d = d, s, b$ ($Q = -1/3$), whose left-handed components can be put into doublets q_L just as in the lepton case. The quark Yukawa terms are constructed analog to the leptonic ones,

$$\mathcal{L}_{\text{Yukawa}} \sim (\bar{q}_L \cdot \phi)\, Y_d d_R + \left(\bar{q}_L \cdot \tilde{\phi}\right) Y_u u_R + \text{h.c.} \tag{1.28}$$

with $\tilde{\phi} = \mathrm{i}\tau_2 \phi$ and $Y_{d,u}$ matrices in flavor space. However, there is a fundamental difference to the lepton terms arising from the fact that this time both the up-type as well as the down-type spinors acquire mass terms, so in the general case it is not possible to diagonalize the mass terms and the charged-current interaction terms simultaneously. Choosing a mass-diagonal basis by unitary transformations

$$U_u Y_u U_u^\dagger = \text{diag}(m_u) \qquad \text{and} \qquad U_d Y_d U_d^\dagger = \text{diag}(m_d) \,, \tag{1.29}$$

one ends up with a nontrivial unitary matrix $V \equiv U_d U_u^\dagger$, the famous CKM matrix, appearing in the charged-current interaction, whose off-diagonal entries induce transitions among the three flavor generations.

Assembling all the pieces of this section, we finally arrive at the SM Lagrangian

$$\mathcal{L}_{\text{SM}} = \mathcal{L}_{\text{matter}} + \mathcal{L}_{\text{gauge}} + \mathcal{L}_{\text{scalar}} + \mathcal{L}_{\text{Yukawa}} \,. \tag{1.30}$$

This theory represents a UV completion of Fermi theory in the sense that it cures all the problems described in Sec. 1.1.2: it is renormalizable and unitary even at tree level, at least with a light enough Higgs, $m_h \lesssim 1\,\text{TeV}$, which might very well be the case according to the recent LHC results. It has been heavily tested over the past decades in a great variety of observables, and a global parameter fit still shows an overwhelming agreement with all data currently available. Nonetheless, in the next section it will be argued why there are good reasons to go beyond the SM.

1.2. Systematic Operator Expansion

1.2.1. General Remarks

After this short historical interlude, the construction principles and properties of the EFT approach shall be addressed now on more general grounds. As illustrated in the previous section, there are basically two different ways to try and incorporate

new physics effects in a systematic and consistent manner into an established and well-confirmed theory or model such as QED in Fermi's case or, from now on, the SM in our case: Either the model building (top-down) approach, or the effective (bottom-up) approach.

In the first case, one would start by postulating an enhanced Lagrangian containing from the beginning all dynamic degrees of freedom, and also conveying a sensible UV completion in the sense that the theory is unitary and renormalizable, i. e. meaningful and well-defined at any energy scale. One could then try to derive from such a theory physical effects to which present or planned experiments might be sensitive. Historically, the electroweak sector of the full SM including the Higgs boson represents an example for such a theory with respect to the original Fermi theory, explaining the weak interactions as well as predicting new degrees of freedom such as the heavy gauge bosons and a scalar.

In the latter (bottom-up) case, one would begin with the established symmetries of the existing and well-understood theory at hand and a priori consider *all* imaginable effects of new physics in the form of effective operators of higher mass dimension, under the sole condition that they must obey these symmetries at the Lagrangian level. The theory thus becomes model-independent in the sense that the question which particular heavy degrees of freedom of the full theory might be present at a higher energy scale Λ to generate these operators is postponed. The gain in generality is traded for the introduction of the explicit "new physics" scale Λ, with all consequences pointed out in Sec. 1.1, namely a hard limit to tree-level unitarity as well as non-renormalizability. However, the bottom-up or effective approach is well suited for the task of describing measurable effects from such a new scale because it confronts new physics completely unbiased, i. e. it parametrizes all possible effects that are manifest at a testable energy scale (considerably smaller than the scale Λ) where the only degrees of freedom are the well known SM particles.

On the other hand, with the SM we already have a UV-complete theory complying with all current experimental data, so what sense does it make to give it up again? The point is, without any new BSM physics, the only remaining relevant scale above v is the Planck scale $\Lambda_\mathrm{P} \sim 10^{18}\,\mathrm{GeV}$, which leads to two very unsatisfactory implications: firstly, bearing in mind all the rich physics structure which was discovered between $\Lambda \sim 10^{-1}\,\mathrm{GeV}$ (the pion mass) and $\Lambda \sim 10^{2}\,\mathrm{GeV}$ (the Z boson mass)—i. e. just three orders of magnitude—only in the 20th century, the idea of an utter void within the subsequent 16 orders of magnitudes does not appear too natural any more. Secondly, the scalar mass m_h receives radiative corrections from higher orders, which are linearly dependent on the cutoff scale, in this case $\delta m_h^2 \sim \Lambda_\mathrm{P}^2$. Hitting the physical value $m_h \simeq 125\,\mathrm{GeV}$ by adjusting the fundamental parameters at Λ_P and evolving them down to LHC energies via the renormalization group equations then requires an incredible, or unnatural, amount of fine tuning. This argument can be turned around to give a rough estimate on the natural size of Λ: the absence of significant fine tuning implies $\delta m_h^2 \lesssim m_h^2$, so including a generic loop suppression this leads to the requirement

$$\frac{\Lambda^2}{16\pi^2} \lesssim v^2 \,. \tag{1.31}$$

Hence, from naturalness one should expect new physics stabilizing m_h against loop corrections around $\Lambda \lesssim 3\,\text{TeV}$, i. e. probably at least indirectly accessible at the LHC.

1.2.2. Construction Principle and Matching

Before moving on to actually apply EFT methods for an effective description of anomalous top effects at the LHC, the following two sections will be devoted to some technical issues of EFT, namely the procedure of its consistent matching to the full theory, and the removal of redundancies contained within an effective operator basis.

Strictly speaking, the matching of the effective theory to the full theory (or another effective theory containing the dynamic degrees of freedom at the scale Λ while introducing a new effective scale $\Lambda' > \Lambda$) only becomes phenomenologically relevant as soon as the heavy physics is known. Although at first glance this is not the case for the effective BSM operators discussed in Sec. 2.1, the topic becomes phenomenologically relevant when the influence of anomalous charged currents on flavor observables such as rare meson decays is taken into account (cf. Sec. (2.5.1)). In this setup, assessing a physics scale $\Lambda \lesssim 10\,\text{GeV}$ (the mass of the B mesons), the effective theory, which can hence be considered as an extended Fermi theory, must be consistently matched to the full SM.

The rest of this section will be held quite general, following the line of argument presented in [52]. Let us begin with a generic effective Lagrangian

$$\mathcal{L}_{\text{eff}}(\phi) = \mathcal{L}(\phi) + \Delta\mathcal{L}(\phi) \tag{1.32}$$

describing the low-energy theory at a scale $\mu < \Lambda$ with a light mode ϕ. This theory shall be matched at $\mu = \Lambda$ to a high-energy theory

$$\mathcal{L}_{\text{full}}(\chi, \phi) = \mathcal{L}_{\text{H}}(\chi, \phi) + \mathcal{L}(\phi) \tag{1.33}$$

comprising in addition to ϕ a heavy mode χ of mass Λ which only appears in $\mathcal{L}_{\text{H}}$. The whole procedure is assumed to be carried out in a perturbative regime where the interactions can be expanded in terms of a small parameter ϵ:

$$\mathcal{L} = \sum_{n=0}^{\infty} \epsilon^n \mathcal{L}^n \,, \qquad \mathcal{L}_{\text{H}} = \sum_{n=0}^{\infty} \epsilon^n \mathcal{L}_{\text{H}}^n \,. \tag{1.34}$$

Now $\Delta\mathcal{L}$ is given by the requirement that both theories describe the same physics at the scale $\mu = \Lambda$, which translates to the condition that the effective actions generated by the low-energy and the high-energy Lagrangian become equal at $\mu = \Lambda$. Equivalently, since the effective action is the generating functional for the one-particle irreducible (1PI) functions, both theories must deliver the same 1PI functions at the matching scale. This can be evaluated order by order in ϵ, starting at $\mathcal{O}(\epsilon)$ because $\Delta\mathcal{L}$ vanishes trivially when the light and the heavy modes decouple,

$$\Delta\mathcal{L} = \sum_{n=1}^{\infty} \epsilon^n \Delta\mathcal{L}^n \,. \tag{1.35}$$

Each specific order in n is then given by

$$\Delta\mathcal{L}^n(\phi) = \sum_m \phi^m \Delta\Gamma^{n,m} \,, \tag{1.36}$$

where, to leading order

$$\Delta\Gamma^{1,m} = \Gamma^{1,m}_{\mathcal{L}_\mathrm{H}+\mathcal{L}} - \Gamma^{1,m}_{\mathcal{L}} \,, \tag{1.37}$$

introducing labels $\Gamma^{n,m}_{\mathcal{L}}$ for general 1PI m-point functions at order n generated by a Lagrangian $\mathcal{L}$. Higher orders in ϵ then recursively evaluate to

$$\Delta\Gamma^{n,m} = \Gamma^{n,m}_{\mathcal{L}_\mathrm{H}+\mathcal{L}} - \Gamma^{n,m}_{\mathcal{L}+\Delta\mathcal{L}_{n-1}} \,, \tag{1.38}$$

where all lower-order results enter via

$$\Delta\mathcal{L}_k \equiv \sum_{n=1}^{k} \epsilon^n \Delta\mathcal{L}^n \,. \tag{1.39}$$

Obviously, going beyond leading order involves loop calculations which require a renormalization scheme to absorb divergences into renormalized parameters. Even if the the high-energy theory is renormalizable, it was shown in Sec. 1.1.2 that the parametrization of nonlocal interactions (from the high energy perspective) in terms of local operators at low energies generally produces non-renormalizable interactions. However, this only means that the low-energy theory cannot be evaluated up to arbitrary orders with just a finite set of parameters. On the other hand, up to a fixed order in ϵ, $\mathcal{L}_\mathrm{eff}$ produces a well-defined finite set of interactions and corresponding parameters, whose values are fixed at $\mu = \Lambda$ by the matching condition. This very procedure is what is commonly being referred to in the literature as "integrating out" the heavy degrees of freedom.

Still, from the UV point of view it is clear that the physics encoded in $\Delta\mathcal{L}$ is essentially nonlocal, because it is generated by propagating heavy modes. However, as stressed in [52], since it is nonlocal *only* in the heavy modes, the corresponding heavy propagators can always be expanded as

$$\frac{1}{p^2-\Lambda^2} = -\frac{1}{\Lambda^2} + \frac{p^2}{\Lambda^4} + \dots \,, \tag{1.40}$$

which allows for the parametrization of the nonlocal physics contained in $\Delta\mathcal{L}$ in terms of an analytical expansion in $1/\Lambda$ times local effective operators $O_i^{(d)}$ of corresponding mass dimension $d > 4$ [38, 64–66]:

$$\Delta\mathcal{L} = \sum_{n=1}^{\infty} \epsilon^n \Delta\mathcal{L}^n \equiv \sum_{d>4,i} \frac{C_i^{(d)}}{\Lambda^{d-4}} O_i^{(d)} + \mathrm{h.c.} \tag{1.41}$$

with dimensionless operator coefficients $C_i^{(d)}$. The validity of this expansion is at the heart of the EFT paradigm. Since the energy scale in the numerator is set by the external momenta resp. the typical energy of the observed process, generically

denoted $\sqrt{s}$, all irrelevant operator contributions will accordingly be suppressed by powers of $\sqrt{s}/\Lambda$, the EFT power counting parameter. Therefore, consistency requires $\sqrt{s} < \Lambda$, and for $\sqrt{s} \ll \Lambda$ considering the leading power counting order is already a good approximation. Finally, note that Eq. (1.41) equates an explicit loop expansion on the left-hand side to a power counting expansion with the loop expansion implicit inside the $C_i^{(d)}$ on the right-hand side in a highly nontrivial way. However, this is completely consistent, which becomes obvious once an appropriate (i. e. mass independent) regularization scheme is chosen: then the loop calculations do not mix power counting orders, so that one can consistently fix the order in each expansion parameter for a given amplitude (cf. e. g. [67]).

Now, even if the full theory is unknown as in the BSM case, the matching procedure still conveys a systematic way to construct the local operators $O_i^{(d)}$ on the right-hand side of Eq. (1.41): If the SM is to represent a good low energy limit once the heavy modes are expanded out (as it obviously does), these effective operators must comply with all local as well as global symmetries imposed on the SM itself. A straightforward way to find a complete basis of such operators is to take the objects appearing in the SM Lagrangian— namely the matter fields $\Psi_{L,R}$, the covariant derivative D_μ, Dirac matrices γ_μ and the field strength tensors as well as the scalar ϕ (cf. Sec. 1.1.3)— and rearrange them in all possible ways to form overall singlets. Hence Eq. (1.41) by definition comprises *all* possible effective operators which may be built according to these rules. A complete list of these operators for $d = 5, 6$ was originally published in [38], cf. the revised minimal list in [49]. Note in this respect that the only possible $d = 5$ operator in such a setup is a neutrino mass term [38], implying that the leading contributions to an anomalous top sector must be $d = 6$ at least, so we will be mainly concerned with the subset $\{O_i^{(6)}\}$ in the further course of this work.

1.2.3. Equivalence Theorem and Redundancies

The last cornerstone to set the stage for an assessment of top physics at the LHC in the next chapter is the systematic treatment of redundancies which are potentially contained in an effective operator basis as defined in Eq. (1.41). Naively, one would like to make use of the classical equations of motion (EOM) to eliminate derivatives and identify redundant structures in the operator basis. Whereas the validity of this procedure is quite obvious at the tree level [38, 50, 51, 53], it is a priori far from clear that it goes through also beyond leading order. While the main concern of the phenomenological part of this thesis is with leading order effects on LHC observables, it is still instructive to see that the procedure is valid up to any fixed perturbative order. (Anyway, it is again a necessary prerequisite to the description of BSM effects on flavor observables, as will be shown later.)

At the heart of the argument lies the equivalence theorem [68–71], stating that the physical effects of a theory must be invariant under field redefinitions. This seems intuitive within the path integral language, because there the fields are only integration variables. Based on this theorem, it was shown that one can always find a particular field redefinition with the very effect of removing derivatives via

the EOM, while leaving the on-shell matrix elements invariant, to any fixed order in perturbation theory [52, 54, 72–75]. To see this in more detail (following the review of the procedure in [54]), one begins with the effective operator expansion, Eq. (1.41), where ϵ is assumed to carry the correct power of the new physics scale corresponding to any given effective operator.

Then, starting with a scalar field ϕ again for simplicity, the terms to be removed from $\Delta\mathcal{L}$ generally have the form $\epsilon^n G[\varphi] D^2\phi$, where φ labels all fields appearing in the theory, and $G[\varphi]$ is any local function of the fields and their derivatives. Up to a fixed order $\mathcal{O}(\epsilon^n)$, the generating functional for the Green's functions with a source j_i for each φ_i reads

$$Z[j] = \int \mathcal{D}\varphi \exp\, \mathrm{i} \int \mathrm{d}^4x \Big\{ \mathcal{L}[\varphi] + \Delta\mathcal{L}_n[\varphi] + j\varphi \Big\} \,, \tag{1.42}$$

where field flavor indices have been suppressed. Now assume that all terms $\propto D^2\phi$ in lower orders than $\mathcal{O}(\epsilon^n)$ have already been removed. By construction of the invariant term $GD^2\phi$, it is clear that $G[\varphi]$ must transform like $\phi^\dagger$, so one can make the change of variables $\phi^\dagger \to (\phi')^\dagger = \phi^\dagger + \epsilon^n G$, finding

$$\begin{aligned} Z'[j] = \int \mathcal{D}\varphi \left| \frac{\delta(\phi')^\dagger}{\delta\phi^\dagger} \right| \exp\, \mathrm{i} \int \mathrm{d}^4x \Big\{ \mathcal{L} + \epsilon^n G \left(\frac{\partial\mathcal{L}}{\partial\phi^\dagger} - \partial_\mu \frac{\partial\mathcal{L}}{\partial\left(\partial_\mu\phi^\dagger\right)} \right) \\ + \Delta\mathcal{L}_n + j\varphi + \epsilon^n j_{\phi^\dagger} G \Big\} \,. \end{aligned} \tag{1.43}$$

Note that the effect of the variable shift in $\mathcal{L}$ has been accounted for to the lowest contributing order $\mathcal{O}(\epsilon^n)$, while any shifts in $\Delta\mathcal{L}_n$ are of $\mathcal{O}(\epsilon^{n+1})$ or higher. Comparing to Eq. (1.42), the changes induced by the transformation are additional terms contributing to $\Delta\mathcal{L}^n$, a Jacobian determinant, and a new term coupling to the source $j_{\phi^\dagger}$. All of them will now be addressed in due order.

Inspecting the new Lagrangian, the variation of $\mathcal{L}$ with respect to $\phi^\dagger$ just gives the Euler-Lagrange equation, multiplied by $\delta\phi^\dagger \equiv \epsilon^n G$. Assuming a canonical kinetic term for ϕ in $\mathcal{L}$, this variation will produce the terms

$$\Delta\mathcal{L}_n \to \Delta\mathcal{L}_{n-1} + \epsilon^n \Delta\mathcal{L}^n + \epsilon^n G \left(-D^2\phi - m^2\phi + \text{terms with more fields} \right) \,, \tag{1.44}$$

where the first term in parentheses exactly cancels the derivative term in $\Delta\mathcal{L}^n$. As emphasized in [52], it is the general feature of the effective approach that *all* other terms produced by the variation must by construction already be present in $\Delta\mathcal{L}^n$, so that they can simply be absorbed into existing operator coefficients. Note that the whole procedure has no effect on any orders lower than $\mathcal{O}(\epsilon^n)$.

In order to study the physical effects of the functional determinant, one can rewrite it in terms of a ghost sector in the Lagrangian introducing Grassmann functions c and $\bar{c}$ (cf. e. g. [63, Eq. (9.69)], giving

$$\mathcal{L}_{\text{ghost}} = \bar{c} \left(1 + \epsilon^n \frac{\delta G}{\delta\phi^\dagger} \right) c \,. \tag{1.45}$$

Now without loss of generality G can be considered to contain just one term (because additive shifts can be carried out consecutively), so in $\mathcal{L}_{\text{ghost}}$ it can only produce either a kinetic term (namely when $G[\varphi] \equiv \partial^m \phi$) or a coupling to the ordinary fields, never both [54]. This means that the ghosts either decouple or do not propagate, so they can be disregarded in any case.

It remains to address the additional source term $\epsilon^n j_{\phi^\dagger} G$ in Eq. (1.43). Its effect is that the original N-point Green's functions

$$\mathcal{G}_N = \langle 0 \,|T\phi(x_1)\cdots\phi(x_N)|\, 0\rangle \tag{1.46}$$

become

$$\mathcal{G}'_N = \langle 0 \,|T(\phi(x_1)+\epsilon^n G(x_1))\cdots(\phi(x_N)+\epsilon^n G(x_N))|\, 0\rangle \ . \tag{1.47}$$

However, it has been shown in [71] (cf. [54]) that this leads to the relation

$$\mathcal{G}'_N = f^N(p)\mathcal{G}_N + \text{terms with} \neq N \text{ poles}, \tag{1.48}$$

where $f(p)$ is some function of the momentum. Therefore, the on-shell amputated Green's functions remain the same up to a renormalization, and the S matrix is not affected.

In conclusion, we have verified that the original generating functional Z, Eq. (1.42), gives the same S matrix as

$$Z[j] = \int \mathcal{D}\varphi \exp\, \mathrm{i} \int \mathrm{d}^4x \Big\{ \mathcal{L}[\varphi] + \big(\Delta\mathcal{L}_n[\varphi] - \epsilon^n G[\varphi] D^2\phi\big) + j\varphi \Big\} \ , \tag{1.49}$$

where the derivative term is removed, quite independent of the particular shape of G. Although this explicit example was carried out with a scalar, it is straightforward to see that the same reasoning applies to terms with derivatives acting on fermion or gauge boson fields. Therefore, whenever terms of the general form $G\not{D}\Psi$ resp. $G^\nu_a D^\mu F^a_{\mu\nu}$ are present in $\Delta\mathcal{L}$, the function G must in each case by construction show the correct transformation behavior to perform the appropriate variable shift and remove those terms. As already argued above, this can be consistently done order by order in ϵ.

As a final remark of this chapter, note that the result of the whole business are nontrivial relations among specific operators: there is just as much physics in a basis with a minimal number of derivative terms as in any other, but one gains the freedom to choose an optimal one (according to whatever criteria), and the number of independent parameters is minimized.

2. Anomalous Top Interactions

Now that the the stage is set in theoretical terms for an effective operator study at the LHC, the question is what sector of the SM should most reasonably be considered to look for anomalous contributions from new physics. As already mentioned in the introduction, the most natural answer to this are the Higgs and the top sector (as well as their interplay via the Yukawa coupling), because the respective particles are the heaviest ones in the SM spectrum and hence hardest to access experimentally. From the theoretical perspective, they are closely related to the symmetry breaking sector of the SM, whose detailed structure remains obscure even with the recent discovery of a higgs-like resonance. While this new particle clearly is a messenger of the dynamics of electroweak symmetry breaking, the top stands out as the only particle which is strongly coupled to it, via its $\mathcal{O}(1)$ Yukawa interaction. But if the top plays a special role in an extended electroweak gauge sector with a more complex breaking pattern, it might very well exhibit non-standard couplings to the other SM particles as well in the low-energy effective theory.

It is the aim of this chapter to develop an effective operator basis for any anomalous top couplings to other SM particles, under the sole restriction that the resulting interactions do not add to an extended flavor sector, i. e. the flavor structure of CC interactions is constrained to the SM version of the CKM matrix introduced in Sec. 1.1.3, and flavor-changing neutral currents (FCNCs) remain loop suppressed via the GIM mechanism [7]. This setup, commonly referred to as "minimal flavor violation" (MFV) in the literature (cf. e. g. [76, 77]), is phenomenologically viable because on one hand the electroweak doublet structure connects anomalous up-type FCNCs with down-type ones, thus enforcing restrictive cancellation patterns in order to comply with rare B decay bounds. On the other hand, LHC searches for an extended top–flavor sector are complementary to those for anomalous CCs, which will be addressed in the further course of this thesis.

After writing down all operators in question, we will use the results of the previous chapter to identify relations among those operators in Sec. 2.1 before discussing their contributions to anomalous couplings, beginning with the trilinear ones to the SM gauge bosons and the Higgs in Sec. 2.2, and moving on to four-fermion contact interactions in Sec. 2.3. Sec. 2.4 summarizes operator relations imposed by SM symmetries as well as existing experimental bounds, while in Sec. 2.5 we present a selection of observables which are potentially sensitive to the extended top sector.

2.1. An Optimal Operator Basis for the Top Sector

In order to parametrize anomalous top couplings, any operator with at least one fermion line will be of interest. However, as already mentioned in the previous chap-

ter, when one naively writes down all possible terms of mass dimension 6 which are singlets under the SM symmetries (i. e. the leading ones in the effective operator expansion, if the lepton number violating Weinberg operator is discarded), the resulting operator basis will contain redundancies, which can generally be made manifest by the application of the EOM. Each identified operator relation will reduce the number of independent parameters in a specific analysis.

As for the question which particular operator basis may turn out to be the optimal one, the answer depends on several considerations. In this respect, even the notion of a "physically motivated" basis is ambiguous, because this could either mean

- a basis which is motivated by a particular realization of the heavy physics at the high-energy end (better termed "model motivated"), or
- a basis which rather corresponds to a particular set of observables or phenomenological behavior at the scale which is actually probed (say "phenomenology motivated").
- Finally, since we aim at performing a Monte Carlo study with the operators, there is the third option of an "implementation motivated" basis (which might coincide with one of the others), cf. Eqs. (2.5) and (2.7)–(2.10) and respective comments below.

Naturally, the second or third approach are the first choice because life is made easiest, and the nature of the heavy physics is unknown anyway. However, whenever the "wrong" basis (in the first sense) is chosen, this will manifest itself in correlated deviation directions from the SM expectation in the parameter space of the analysis. This issue will be taken up again later in more detail.

We will now list all effective $d = 6$ operators which can contribute to anomalous top couplings to the other SM particles, essentially following the listings in [46–48], and at times also referring to [49], which represents a convenient summary of all possible operator rewritings. The particular objects from which the operators are built up (such as fields, derivatives, generators, etc.) were introduced in Sec. 1.1.3, where the naming convention had already been adapted such that it coincides as much as possible with [46–48].

2.1.1. Two-fermion Operators

Starting with the operators containing just one fermion line (up-type or charged-current) and hence inducing anomalous trilinear top couplings to the Higgs h, as well as the SM gauge bosons g, γ, Z, and W, the list obtained from [46, 47] contains operators with fermion bilinears in scalar, vector, tensor and more complicated Lorentz representations. The only possible scalar operator is

$$O_{u\phi}^{ij} = \left(\phi^\dagger \phi\right)\left(\bar{q}_{Li} u_{Rj} \tilde{\phi}\right) \,, \tag{2.1}$$

introducing explicit generation indices $i, j = 1, 2, 3$. Furthermore, one finds the vector operators

$$O_{\phi q}^{(1,ij)} = \left(\phi^\dagger \mathrm{i} \overleftrightarrow{D}_\mu \phi\right)\left(\bar{q}_{Li}\gamma^\mu q_{Lj}\right) , \tag{2.2a}$$

$$O_{\phi q}^{(3,ij)} = \left(\phi^\dagger \mathrm{i} \overleftrightarrow{D}^I_\mu \phi\right)\left(\bar{q}_{Li}\gamma^\mu \tau^I q_{Lj}\right) , \tag{2.2b}$$

$$O_{\phi u}^{ij} = \left(\phi^\dagger \mathrm{i} \overleftrightarrow{D}_\mu \phi\right)\left(\bar{u}_{Ri}\gamma^\mu u_{Rj}\right) , \tag{2.2c}$$

$$O_{\phi\phi}^{ij} = \left(\tilde{\phi}^\dagger \mathrm{i} D_\mu \phi\right)\left(\bar{u}_{Ri}\gamma^\mu d_{Rj}\right) , \tag{2.2d}$$

with Pauli matrices τ^I $(I = 1, 2, 3)$ generating the gauged $\mathbf{SU}(2)_L$ symmetry. Note that the operators (2.2a)–(2.2c) have been constrained to their hermitian subset, using [49]

$$\phi^\dagger \mathrm{i} \overleftrightarrow{D}_\mu \phi \equiv \mathrm{i}\phi^\dagger \left(D_\mu - \overleftarrow{D}_\mu\right)\phi \quad \text{and} \quad \phi^\dagger \mathrm{i} \overleftrightarrow{D}^I_\mu \phi \equiv \mathrm{i}\phi^\dagger \left(\tau^I D_\mu - \overleftarrow{D}_\mu \tau^I\right)\phi , \tag{2.3}$$

because the anti-hermitian combinations are redundant and can be absorbed into the coefficients of the operators $O_{u\phi}$ (2.1) and a similar one $O_{d\phi}$ (which does not contribute to top interactions), as shown explicitly in [47], cf. appendix B.2. Hence also the coefficients of Eqs. (2.2a)–(2.2c) are real-valued. The tensor operators read

$$O_{uW}^{ij} = \left(\bar{q}_{Li}\sigma^{\mu\nu}\tau^I u_{Rj}\right)\tilde{\phi}\, W^I_{\mu\nu} , \tag{2.4a}$$

$$O_{dW}^{ij} = \left(\bar{q}_{Li}\sigma^{\mu\nu}\tau^I d_{Rj}\right)\phi\, W^I_{\mu\nu} , \tag{2.4b}$$

$$O_{uB\phi}^{ij} = \left(\bar{q}_{Li}\sigma^{\mu\nu}\tau^I u_{Rj}\right)\tilde{\phi}\, B_{\mu\nu} , \tag{2.4c}$$

$$O_{uG\phi}^{ij} = \left(\bar{q}_{Li}\sigma^{\mu\nu}\lambda^a u_{Rj}\right)\tilde{\phi}\, G^a_{\mu\nu} . \tag{2.4d}$$

So far, the only new object with respect to Sec. 1.1.3 is the gauge field G^a_μ associated with the $\mathbf{SU}(3)$ gauge symmetry of QCD, generated by the eight Gell-Man matrices λ^a $(a = 1 \cdots 8)$ in the adjoint representation. Of the remaining operators listed in [46] with a more complicated Lorentz structure, the operators

$$O_{Du}^{ij} = \left(\bar{q}_{Li} D_\mu u_{Rj}\right) D^\mu \tilde{\phi} , \tag{2.5a}$$

$$O_{\bar{D}u}^{ij} = \left(\bar{q}_{Li} \overleftarrow{D}_\mu u_{Rj}\right) D^\mu \tilde{\phi} , \tag{2.5b}$$

$$O_{Dd}^{ij} = \left(\bar{q}_{Li} D_\mu d_{Rj}\right) D^\mu \phi , \tag{2.5c}$$

$$O_{\bar{D}d}^{ij} = \left(\bar{q}_{Li} \overleftarrow{D}_\mu d_{Rj}\right) D^\mu \phi \tag{2.5d}$$

also appear to contribute to trilinear top interactions. However, the differences $O_{Du(d)}^{ij} - O_{\bar{D}u(d)}^{ij}$ are entirely redundant as is shown in [46], and the sums $O_{Du(d)}^{ij} + O_{\bar{D}u(d)}^{ij}$ are proportional to the gauge boson momentum $q^\mu = (p_i - p_j)^\mu$ so that amplitudes containing these vertices vanish either for physical on-shell gauge bosons or for on-shell light fermions coupling to them, which is always the case at parton level for all processes to be considered in the phenomenological studies discussed later on.

Finally, in [46] there remain the operators

$$O_{qW}^{ij} = \left(\bar{q}_{Li}\gamma^{\mu}\tau^{I}D^{\nu}q_{Lj}\right)W_{\mu\nu}^{I} \ , \tag{2.6a}$$
$$O_{qB}^{ij} = \left(\bar{q}_{Li}\gamma^{\mu}D^{\nu}q_{Lj}\right)B_{\mu\nu} \ , \tag{2.6b}$$
$$O_{uB}^{ij} = \left(\bar{u}_{Ri}\gamma^{\mu}D^{\nu}u_{Rj}\right)B_{\mu\nu} \ , \tag{2.6c}$$
$$O_{qG}^{ij} = \left(\bar{q}_{Li}\lambda^{a}\gamma^{\mu}D^{\nu}q_{Lj}\right)G_{\mu\nu}^{a} \ , \tag{2.6d}$$
$$O_{uG}^{ij} = \left(\bar{u}_{Ri}\lambda^{a}\gamma^{\mu}D^{\nu}u_{Rj}\right)G_{\mu\nu}^{a} \ . \tag{2.6e}$$

These operators are special because they still contain a derivative which can be replaced by the EOM, but we will show below that the result of the procedure connects top–gauge couplings and four-fermion couplings which contribute to physical matrix elements directly to each other by underlying operator coefficients. This means that, even in a study purely concerned with anomalous trilinear interactions, the operators (2.6) are not entirely redundant, and there is no good reason to drop them from the basis. However, due to their complicated Lorentz and gauge structure, trying to find and implement all interactions generated by them (such as quartic $tbWg$ or even quintet interactions, in addition to the trilinear ones) would be a tedious affair, so rewriting them could be fruitful in the sense of an implementation-motivated optimal basis. A detailed review of the rewriting procedure and discussion will be given in Sec. 2.1.3, after introducing the four-fermion operators in a more general way.

2.1.2. Four-fermion Operators

Turning now to a basis for four-fermion contact interactions, it is instructive to begin with the systematics of the classification, as e. g. presented in [49]. In the spirit of the current–current operators which were already used to describe the Fermi interaction in Sec. 1.1, all contact interactions can systematically be accounted for by combining two fermion bilinears with specific SM quantum numbers in all possible ways that result in overall singlets. One could start by forming bilinears of zero net hypercharge, which only allows for Lorentz vectors or "currents" of definite chirality, which are then further classified according to their net isospin and color quantum numbers, i. e. whether they are weak isospin triplets, or color octets, or both. Contracting these currents to overall singlets finally results in quartic terms of definite chirality $(\overline{L}L)(\overline{L}L)$, $(\overline{R}R)(\overline{R}R)$, and $(\overline{L}L)(\overline{R}R)$. Within the obtained basis, one can make use of the completeness relations of the symmetry generators in combination with appropriate Fierz rearrangements to identify redundancies inside the subsets $(\overline{L}L)(\overline{L}L)$ and $(\overline{R}R)(\overline{R}R)$, cf. appendix B.2.

After this procedure, the only operators remaining in the $(\overline{L}L)(\overline{L}L)$ class are

$$O_{qf}^{(1,ijkl)} = \left(\bar{q}_{Li}\gamma^{\mu}q_{Lj}\right)\left(\bar{f}_{Lk}\gamma_{\mu}f_{Ll}\right) \ , \tag{2.7a}$$
$$O_{qf}^{(3,ijkl)} = \left(\bar{q}_{Li}\gamma^{\mu}\tau^{I}q_{Lj}\right)\left(\bar{f}_{Lk}\gamma_{\mu}\tau^{I}f_{Ll}\right) \tag{2.7b}$$

with $f = q, \ell$, while in the $(\overline{R}R)(\overline{R}R)$ class one finds

$$O_{uf}^{(1,ijkl)} = \left(\bar{u}_{Ri}\gamma^{\mu}u_{Rj}\right)\left(\bar{f}_{Rk}\gamma_{\mu}f_{Rl}\right) , \tag{2.8a}$$

$$O_{ud}^{(8,ijkl)} = \left(\bar{u}_{Ri}\gamma^{\mu}\lambda^{a}u_{Rj}\right)\left(\bar{d}_{Rk}\gamma_{\mu}\lambda^{a}d_{Rl}\right) \tag{2.8b}$$

with $f = u, d, e$. Finally, the mixed class $(\overline{L}L)(\overline{R}R)$ contains the operators

$$O_{qf}^{(1,ijkl)} = \left(\bar{q}_{Li}\gamma^{\mu}q_{Lj}\right)\left(\bar{f}_{Rk}\gamma_{\mu}f_{Rl}\right) \qquad \text{with } f = u, d, e , \tag{2.9a}$$

$$O_{qf}^{(8,ijkl)} = \left(\bar{q}_{Li}\gamma^{\mu}\lambda^{a}q_{Lj}\right)\left(\bar{f}_{Rk}\gamma_{\mu}\lambda^{a}f_{Rl}\right) \qquad \text{with } f = u, d , \tag{2.9b}$$

$$O_{\ell u}^{(1,ijkl)} = \left(\bar{\ell}_{Li}\gamma^{\mu}\ell_{Lj}\right)\left(\bar{u}_{Rk}\gamma_{\mu}u_{Rl}\right) . \tag{2.9c}$$

Whenever it is not possible to form hypercharge singlets already in the bilinears, they come as chirality mixing Lorentz scalars, pseudoscalars, and tensors. The resulting quartic singlet terms are thus in the classes $(\overline{L}R)(\overline{L}R)$ and $(\overline{L}R)(\overline{R}L)$, where tensor contractions can be eliminated by a respective Fierz identity. This leaves the four-quark operators

$$O_{quqd}^{(1,ijkl)} = \left(\bar{q}_{Li}^{p}u_{Rj}\right)\epsilon_{pr}\left(\bar{q}_{Lk}^{r}d_{Rl}\right) , \tag{2.10a}$$

$$O_{quqd}^{(8,ijkl)} = \left(\bar{q}_{Li}^{p}\lambda^{a}u_{Rj}\right)\epsilon_{pr}\left(\bar{q}_{Lk}^{r}\lambda^{a}d_{Rl}\right) \tag{2.10b}$$

(with $\mathrm{i}\tau_2 \equiv \epsilon$) as well as the quark–lepton operators

$$O_{\ell edq}^{ijkl} = \left(\bar{\ell}_{Li}e_{Rj}\right)\left(\bar{d}_{Rk}q_{Ll}\right) , \tag{2.11a}$$

$$O_{\ell equ}^{(1,ijkl)} = \left(\bar{\ell}_{Li}^{p}e_{Rj}\right)\epsilon_{pr}\left(\bar{q}_{Lk}^{r}u_{Rl}\right) , \tag{2.11b}$$

$$O_{\ell equ}^{(3,ijkl)} = \left(\bar{\ell}_{Li}^{p}\sigma_{\mu\nu}e_{Rj}\right)\epsilon_{pr}\left(\bar{q}_{Lk}^{r}\sigma^{\mu\nu}u_{Rl}\right) , \tag{2.11c}$$

where in the last operator the $\sigma_{\mu\nu}$ tensor was not rewritten in order to keep the color contraction inside a single quark bilinear.

Note again that the operator relations obtained by completeness and Fierz relations do not suggest a favored operator basis; for instance, in [48] the four-fermion interactions are equivalently parametrized by operators entirely without isospin or color multiplets, at the cost of nontrivial color flows between the bilinears. The decision to choose the parametrization given in Eqs. (2.7)–(2.10) with explicit adjoint group indices and color-singlet fermion bilinears is again implementation motivated, because coding them in WHIZARD thus becomes straightforward (cf. Sec. 3.2).

2.1.3. Operator Rewriting

The last part of this section will be devoted to a more detailed recapitulation of the rewriting procedure and its consequences for the operators (2.6) as e. g. presented in [46], illustrating the main steps for O_{qW}^{ij} (2.6a): starting from its decomposition into hermitian and anti-hermitian parts, the hermitian part can be partially integrated to give

$$\frac{1}{2}\left[O_{qW}^{ij} + \left(O_{qW}^{ji}\right)^{\dagger}\right] = \frac{1}{2}\left(\bar{q}_{Li}\gamma^{\mu}\tau^{I}q_{Lj}\right)\left(D^{\nu}W_{\nu\mu}\right)^{I} \tag{2.12}$$

(dropping the total derivative), where the EOM of the W field

$$\left(D^\nu W_{\nu\mu}\right)^I = \frac{g}{2}\left(\bar{\ell}_{Li}\gamma_\mu\tau^I\ell_{Li} + \bar{q}_{Li}\gamma_\mu\tau^I q_{Li} + \mathrm{i}\phi^\dagger\overleftrightarrow{D}^I_\mu\phi\right) \tag{2.13}$$

can be applied to replace the derivative. On the other hand, with some algebra [38, 46] the anti-hermitian part can be brought in the form

$$\frac{1}{2}\left[O_{qW}^{ij} - \left(O_{qW}^{ji}\right)^\dagger\right] = -\frac{1}{4}\left(\bar{q}_{Li}\sigma^{\mu\nu}\tau^I\mathrm{i}\not{D}q_{Lj}W^I_{\mu\nu} - \mathrm{h.c.}\right) \tag{2.14}$$

up to total derivatives, where the EOM of the quark field

$$\mathrm{i}\not{D}q_{Li} = Y^u_{ij}u_{Rj}\tilde{\phi} + Y^d_{ij}d_{Rj}\phi \tag{2.15}$$

(introducing Yukawa matrices $Y^{u/d}$) can be inserted. Joining it all together, one arrives at the operator equality

$$O_{qW}^{ij} = +\frac{g}{4}\left[O_{qq}^{(3,ijkk)} + O_{q\ell}^{(3,ijkk)} + O_{\phi q}^{(3,ij)}\right] \tag{2.16a}$$

$$-\frac{1}{4}\left[Y^u_{jk}\,O^{ik}_{uW} + Y^d_{jk}\,O^{ik}_{dW} - Y^{u\dagger}_{ki}\left(O^{jk}_{uW}\right)^\dagger - Y^{d\dagger}_{ki}\left(O^{jk}_{dW}\right)^\dagger\right]\,. \tag{2.16b}$$

Obviously, all the terms on the right-hand side are redundant and can be absorbed into the operators (2.2b), (2.4a), (2.4b), and (2.7b). However, unlike the rewritings previously performed to remove e. g. the non-hermitian part of (2.2a)–(2.2c) or some of the four-fermion terms, the EOM relation this time mixes operators generating trilinear top–gauge interactions with those generating four-fermion interactions. This illustrates the fact that a distinction of trilinear and quartic couplings is ambiguous at the level of physical amplitudes within an effective approach, because it is not possible to consistently define an operator basis generating only trilinear couplings without including either O_{qW}, or $O_{qq}^{(3)}$ and $O_{q\ell}^{(3)}$. This point has been ignored previously, and will hence be further stressed in Sec. 2.2.2 below.

Although clearly either choice of operators will lead to an equally complete parametrization of the underlying physics with the same overall number of independent parameters, the rewriting procedure corresponds to a shift of the original operator coefficients. Setting $i = j = 3$ and dropping all generation superscripts for the moment, these shifts are:

$$\begin{aligned}
\delta C_{\phi q}^{(3)} &= \frac{g}{2}\mathrm{Re}\,C_{qW} = \delta C_{qq}^{(3)} = \delta C_{q\ell}^{(3)}\,,\\
\delta\mathrm{Im}\,C_{uW} &= -\frac{m_t}{\sqrt{2}v}\mathrm{Im}\,C_{qW}\,,\\
\delta\mathrm{Im}\,C_{dW} &= -\frac{m_b}{\sqrt{2}v}\mathrm{Im}\,C_{qW} \simeq 0\,,
\end{aligned} \tag{2.17}$$

assuming an approximate decoupling of the third generation in the Yukawa matrices. This is only to underline once more the statement that the new physics generating an anomalous low-energy behavior need not be aligned with the effective operators chosen to parametrize it, which would manifest itself in a correlated deviation from the SM of several parameters in the chosen basis. The other operators

alike to O_{qW}, Eq. (2.6b)–(2.6e), can be rewritten in a very similar fashion using the EOM (B.1)–(B.3), with the same effect of shifting original operator coefficients, cf. (B.7). However, the EOM relations for the QCD operators (2.6d) and (2.6e) comprise a qualitative difference to the electroweak ones as displayed in Eq. (2.16): consider e. g.

$$O_{uG}^{ij} = + \frac{g_s}{4} \left[O_{qu}^{(8,ijkk)} + O_{uu}^{(8,ijkk)} + O_{ud}^{(8,ijkk)} \right] \tag{2.18a}$$

$$+ \frac{1}{4} \left[Y_{ki}^{u} \, O_{uG\phi}^{kj} - Y_{jk}^{u\dagger} \left(O_{uG\phi}^{ki} \right)^{\dagger} \right] \ . \tag{2.18b}$$

In this case, unlike the electroweak sector, the hermitian part (2.18a) $\sim \mathrm{Re}\, C_{uG}$ of the relation does not manifestly mix trilinear and quartic interactions any more (cf. Eq. (2.16a)), because the QCD symmetry is unbroken.

2.2. Trilinear Interactions

2.2.1. General Procedure

Starting from the effective operator list introduced in the previous section, we can now go on to physical states of the gauge and matter fields and write down the interaction terms generated by it. Specifically, one replaces the interaction eigenstates in the operators by eigenstates of mass and charge in unitarity gauge, using the relations (1.22) found in Sec. 1.1.3 for the gauge bosons and the gauge fixed scalar doublet $\phi(x) = 1/\sqrt{2}(0, v + h(x))^T$. For the fermions, since we are not concerned with non-minimal flavor violation such as FCNCs in the phenomenology chapter, any nontrivial flavor structure will remain limited to the CKM matrix introduced in Se. 1.1.3. In the context of anomalous top couplings, this means that one can decouple the third generation and simply identify it with the heavy flavor doublet $(t, b)^T$.

For illustration, this procedure shall now be sketched cursorily for the operator

$$\begin{aligned} O_{uW}^{ij} &= \left(\bar{q}_{Li} \sigma^{\mu\nu} \tau^I u_{Rj} \right) \tilde{\phi} W_{\mu\nu}^I \\ &= \left(\bar{q}_{Li} \sigma^{\mu\nu} \tau^I u_{Rj} \right) \tilde{\phi} \left(-2\partial_\nu W_\mu^I - g \varepsilon_{IJK} W_\mu^J W_\nu^K \right) \ , \end{aligned} \tag{2.19}$$

where the antisymmetry of the sigma tensor has been used for the Abelian part of the field strength. Now transform the W components and Pauli matrices according to Eq. (1.22) to find

$$O_{uW}^{ij} = \left(\bar{q}_{Li} \sigma^{\mu\nu} 2\tau^- u_{Rj} \right) \tilde{\phi} \left[-2\partial_\nu \frac{1}{\sqrt{2}} W_\mu^- - 2\mathrm{i}g \frac{1}{\sqrt{2}} W_\mu^3 W_\nu^- \right] \tag{2.20a}$$

$$+ \left(\bar{q}_{Li} \sigma^{\mu\nu} \tau^3 u_{Rj} \right) \tilde{\phi} \left[-2\partial_\nu W_\mu^3 - 2\mathrm{i}g W_\mu^- W_\nu^+ \right] \ , \tag{2.20b}$$

where $\tau^+ \tilde{\phi} \equiv 0$ was already dropped. Finally, let $i = j = 3$ and perform the

summation over fundamental $\mathbf{SU}(2)$ indices, which gives

$$O_{uW}^{33} = 2v\Big\{\left(\bar{b}\sigma^{\mu\nu}P_R t\right)\left[-\partial_\nu W_\mu^- - \mathrm{i}gW_\mu^3 W_\nu^-\right] \tag{2.21a}$$

$$+\frac{1}{\sqrt{2}}\left(\bar{t}\sigma^{\mu\nu}P_R t\right)\left[-\partial_\nu W_\mu^3 - \mathrm{i}gW_\mu^- W_\nu^+\right]\Big\} \tag{2.21b}$$

$$\text{with } W_\mu^3 \to c_w Z_\mu + s_w A_\mu \ .$$

Similarly, one finds

$$O_{dW}^{33} = 2v\Big\{\left(\bar{t}\sigma^{\mu\nu}P_R b\right)\left[-\partial_\nu W_\mu^+ - \mathrm{i}gW_\mu^+\left(c_w Z + s_w A\right)_\nu\right] \tag{2.22a}$$

$$+\frac{1}{\sqrt{2}}\left(\bar{b}\sigma^{\mu\nu}P_R b\right)\left[-\partial_\nu W_\mu^3 - \mathrm{i}gW_\mu^- W_\nu^+\right]\Big\} \ , \tag{2.22b}$$

so that in summary there are trilinear CC interactions tbW and NC interactions ttZ/γ as well as associated quartic interactions $ttWW$, $tbWZ/\gamma$, but also respective NC bottom couplings. In conclusion, Eqs. (2.21) and (2.22) highlight the following facts:

- The gauge invariant construction of the effective operators requires quartic couplings to be included along with the trilinear ones;
- irrespective of the overall normalization of the operator coefficients, Eqs. (2.21) and (2.22) fix the relative coefficients of the trilinear and quartic interactions by gauge invariance, which can be explicitly checked by Ward identities, cf. Sec. 3.3;
- the $\mathbf{SU}(2)_L$ structure of the gauge group relates NC and CC interactions as well as top and bottom interactions to each other, and the question how many of them can be independently varied at all depends on the overall number of independent operators and hence coefficients.

In order to find the complete set of operators contributing to a specific interaction over the next sections, one simply considers all operators which naively contribute and repeats the exercise shown above. Adding up hermitian combinations,

$$\Delta\mathcal{L} \sim \frac{1}{\Lambda^2}\sum_i \left(C_i O_i + C_i^* O_i^\dagger\right) \ , \tag{2.23}$$

finally gives a unique mapping of operator coefficients onto anomalous couplings. Relations among the resulting set of couplings will be discussed in Sec. 2.4.

2.2.2. tbW Couplings

Before presenting a list of trilinear tbW interactions generated by a specific subset of effective operators, the overall distinction of trilinear and higher interactions needs some justification, because as argued in Sec. 1.2.2 the effective operators are constructed to reproduce the correct physical amplitudes at each order in the power

counting expansion. Moreover, it was illustrated in Sec. 2.1 that due to EOM relations there is some freedom left to choose a complete operator basis in a minimal way, so that there is no fundamental guiding principle within the EFT approach to pick out a subset of operators, let alone specific interactions. Rather, the restriction to trilinear interactions is phenomenology motivated in the sense that one expects different interactions to correspond to different sensitive observables because of the kinematics. Thus, for certain observables it may be sufficient to consider a subset of operators generating only the relevant couplings, which also reduces the number of independent parameters in the analysis. While there is no general obstruction to this pragmatic approach, special care must be taken when defining the underlying operator basis because of the aforementioned operator relations. For example, in the context of anomalous tbW interactions one clearly should consider all two-fermion operators with a nontrivial $\mathbf{SU}(2)_L$ structure inducing charged currents, namely (2.2b), (2.2d), (2.4a)–(2.4b), and (2.6a). Although there is an EOM relation for the latter one, cf. Eq. (2.16), it connects operator (2.2b) to four-fermion operators via the same Wilson coefficient, so that rather than entirely dropping it from the beginning, we include it to study its influence on the tbW sector.

As outlined in the previous section, one can now insert the scalar vev and physical states of the gauge fields into these operators to identify all contributions to the tbW vertex. The resulting effective tbW interaction Lagrangian can be written as [46]

$$\mathcal{L}_{tbW} = -\frac{g}{\sqrt{2}}\bar{b}\,\gamma^\mu\big(V_L P_L + V_R P_R\big)\,t\,W^-_\mu + \text{h.c.} \tag{2.24a}$$

$$-\frac{g}{\sqrt{2}}\bar{b}\,\frac{\mathrm{i}\sigma^{\mu\nu}q_\nu}{m_W}\big(g_L P_L + g_R P_R\big)\,t\,W^-_\mu + \text{h.c.} \tag{2.24b}$$

$$-\frac{g}{\sqrt{2}}\bar{b}\,\gamma^\mu\frac{q^2-m_W^2}{m_W^2}\big(V_L^{\text{off}} P_L\big)\,t\,W^-_\mu + \text{h.c.}\,, \tag{2.24c}$$

where all couplings except for $V_L \equiv V_{tb} \simeq 1$ vanish in the SM at tree level, and get the following anomalous contributions from operator coefficients[1]:

$$\begin{aligned}
\delta V_L &= \left(C^{(3)}_{\phi q} + \frac{g}{2}\mathrm{Re}\,C_{qW}\right)\frac{v^2}{\Lambda^2}\,, & \delta g_L &= \sqrt{2}C^*_{dW}\frac{v^2}{\Lambda^2}\,,\\
\delta V_R &= \frac{1}{2}C^*_{\phi\phi}\frac{v^2}{\Lambda^2}\,, & \delta g_R &= \sqrt{2}C_{uW}\frac{v^2}{\Lambda^2}\,,\\
\delta V_L^{\text{off}} &= \frac{g}{2}\mathrm{Re}\,C_{qW}\frac{v^2}{\Lambda^2}\,.
\end{aligned} \tag{2.25}$$

The normalization of the couplings has been chosen such that their relation to the SM contribution in Eq. (2.24) is simplified (cf. [46]), and the anomalous coupling values are explicitly suppressed by the power counting parameter $(v/\Lambda)^2$ in the coefficient mapping (2.25) (note that δV_L is purely real and hence CP-conserving). The interaction terms (2.24a) and (2.24b) represent the on-shell parametrization widely used in various phenomenological and experimental studies [78–81], which is

[1] Note that in Eq. (37) of [46] the operator coefficient $C^{33}_{\phi\phi}$ appearing in δV_R should also be complex-conjugated.

retrieved from the operators (2.2b), (2.2d) and (2.4a)–(2.4b). The interaction (2.24c) emerges from the hermitian part of O_{qW} (2.6a),

$$O_{qW} + O_{qW}^\dagger = \big(\bar{q}_{L3}\gamma^\mu\tau^I q_{L3}\big)\big(\partial^2 W_\mu^I\big) + \text{higher contact interactions}, \tag{2.26}$$

cf. Eq. (2.12), which—unlike the anti-hermitian part—cannot be completely recast into a combination of the other four operators. However, the *partial* redundance of O_{qW} has been made explicit in the parametrization (2.24) by defining its on-shell part into V_L so that any contribution $\sim V_L^{\text{off}}$ vanishes when the W goes on the mass shell. Hence it is no surprise that in δV_L of Eq. (2.25) we find again the shift of the coefficient $C_{\phi q}^{(3)}$ already stated in Eq. (2.17) after the operator rewriting. Furthermore, by comparison to Eq. (2.16), one finds that all contributions $\sim V_L^{\text{off}}$ must be in one-to-one correspondence to the four-fermion contact interactions given in (2.16a), which is also highlighted by the fact that in physical amplitudes the kinematic structure of the W propagator is exactly cancelled by the q-dependent vertex.

We have now isolated the non-redundant contribution of O_{qW} to the tbW interaction Lagrangian, and also identified the most convenient way to implement it in a gauge-invariant way, namely by adding the quartic fermion vertices

$$\begin{aligned}\Delta\mathcal{L}_{tbW} =& \frac{g_\times}{\Lambda^2}\big(\bar{b}\gamma^\mu P_L t\big)\Big[\big(\bar{u}_k\gamma_\mu P_L d_k\big) + \big(\bar{\nu}_k\gamma_\mu P_L e_k\big)\Big] + \text{h.c.} \\ &\text{with } g_\times = g\,\text{Re}\,C_{qW}\end{aligned} \tag{2.27}$$

(cf. [48, 82, 83]), giving a relation of coefficients

$$V_L^{\text{off}} = \frac{v^2}{2\Lambda^2}\, g_\times \ . \tag{2.28}$$

Of course, one might ask at this point if such a coupling structure should be counted among the anomalous tbW sector, but then again it must be noted that as a consequence of the common operator basis, the trilinear coupling V_L is related to V_L^{off} through an underlying operator coefficient. Specifically, Eq. (2.25) illustrates that, in contrast to the results presented in [81], a limit on δV_L cannot be unambiguously mapped onto a limit on the operator coefficient $C_{\phi q}^{(3)}$ without also bounding δV_L^{off} or the anomalous NC sector, see Sec. 2.4. Moreover, the operator basis including O_{qW} and the corresponding set of couplings (2.24) parametrize *all* anomalous diagram insertions which can interfere with the SM diagram in a minimal way, making this approach consistent at the amplitude level. Finally, as pointed out in Sec. 5.1.3, the inclusion of the additional coupling also affects the interpretation of current and upcoming experimental results at the LHC.

To conclude this discussion, of course there is no question that the operator rewritings summarized in Eq. (B.7) reveal redundant structures, with the effect of reducing the number of independent coupling parameters: all effects of O_{qW} can be consistently absorbed into other operators which are already existent in the *complete* basis including four-fermion operators, cf. Eq. (2.17). However, this corresponds to a particular choice of the minimal basis which is motivated not by any underlying

heavy physics but by convenience. This may result in a correlation of the couplings $V_L \simeq V_L^{\text{off}}$, indicating that the chosen parametrization, while convenient, is not aligned with the actual physics generating it, a complication which is completely lost when the contact terms are simply dropped from a tbW analysis. Rather than disregarding them, one should study their influence on tbW observables, and also look for suitable observables to tell them apart.

2.2.3. ttZ Couplings

Just as in the case of CC interactions in the previous section, by virtue of the operator rewriting for operators (2.6), cf. Eq. (B.7), the most general anomalous ttZ vertex can be completely parametrized by the Lorentz structures $\propto \gamma^\mu$ and $\propto \sigma^{\mu\nu} q_\nu$, plus NC four-fermion interactions with nontrivial operator relations to the trilinear ones. Starting with the trilinear part, one finds [46]

$$\mathcal{L}_{ttZ} = -\frac{g}{2c_w}\bar{t}\gamma^\mu\big(X_{tt}^L P_L + X_{tt}^R P_R - 2s_w^2 Q_t\big)t\, Z_\mu \tag{2.29a}$$

$$-\frac{g}{2c_w}\bar{t}\frac{\mathrm{i}\sigma^{\mu\nu}q_\nu}{m_Z}\big(d_V^Z + \mathrm{i}d_A^Z\gamma_5\big)t\, Z_\mu\,, \tag{2.29b}$$

where this time the Lagrangian already is manifestly hermitian, making all anomalous coupling parameters real-valued, so that the axial tensor coupling d_A^Z explicitly violates CP. In the SM, at tree level $X_{tt}^L = 1$ and all other couplings vanish. The contributing operators are almost the same as in the tbW sector, plus the purely NC ones proportional to the hypercharge gauge field B_μ, namely (2.4c) and (2.6b)–(2.6c). In addition, the purely CC operator (2.2d) is replaced by the purely NC one (2.2c). The resulting coefficient mapping is

$$\delta X_{tt}^L = \Big[C_{\phi q}^{(3)} - C_{\phi q}^{(1)} + \frac{1}{2}\mathrm{Re}\,\big(gC_{qW} - g'C_{qB}\big)\Big]\frac{v^2}{\Lambda^2}\,, \tag{2.30}$$

$$\delta X_{tt}^R = -\Big[C_{\phi u} + \frac{g'}{2}\mathrm{Re}\,C_{uB}\Big]\frac{v^2}{\Lambda^2}\,, \tag{2.31}$$

$$\delta d_V^Z = \sqrt{2}\,\mathrm{Re}\big[c_w C_{uW} - s_w C_{uB\phi}\big]\frac{v^2}{\Lambda^2}\,, \tag{2.32}$$

$$\delta d_A^Z = \sqrt{2}\,\mathrm{Im}\big[c_w C_{uW} - s_w C_{uB\phi}\big]\frac{v^2}{\Lambda^2}\,. \tag{2.33}$$

Note that the vector couplings receive contributions from the hermitian parts of the partially redundant operators, which also generate contact interactions of the form

$$\Delta\mathcal{L}_{ttZ} = \frac{1}{\Lambda^2}\sum_{A,B=L,R} g_{\times,f}^{AB}\big(\bar{t}\gamma_\mu P_A t\big)\big(\bar{f}_k\gamma^\mu P_B f_k\big)\,, \tag{2.34}$$

where $f = q, \ell$ in the left-handed case and $f = u, d, e, \nu$ right-handed. The couplings $g_{\times,f}^{AB}$ are all independent, but could be aligned with some direction in the X_{tt}^L–X_{tt}^R plane, as well as with the CC couplings.

2.2.4. $tt\gamma$ Couplings

From now on, life becomes considerably easier, because the $\mathbf{U}(1)_{\text{QED}}$ remains exact even after electroweak symmetry breaking. Therefore, the photon gauge field is decoupled from the scalar sector even at the effective operator level, which is constructed to respect this symmetry. Accordingly, the vector-like effective operators (2.2a)–(2.2d) with a covariant derivate acting on the scalar do not contribute to this vertex. The result is that the electromagnetic charge Q coupling via γ^μ does not receive effective contributions from $d = 6$ operators on-shell, while off-shell contributions $\propto q^2\gamma^\mu$ from operators (2.6a)–(2.6c) can be consistently absorbed into the four-fermion sector, with no trailing connection to any on-shell trilinear coupling. The only relevant contributions $\propto \sigma^{\mu\nu}q_\nu$ stem from the field strength operators (2.4a) and (2.4c). The photon sector of the effective interaction Lagrangian then reads [46]

$$\Delta\mathcal{L}_{tt\gamma} = -\mathrm{e}Q_t\bar{t}\gamma^\mu t\,A_\mu - \mathrm{e}\bar{t}\frac{\mathrm{i}\sigma^{\mu\nu}q_\nu}{m_t}\left(d_V^\gamma + \mathrm{i}d_A^\gamma\gamma_5\right)t\,A_\mu \tag{2.35}$$

including the SM interaction with $Q_t = 2/3$, as well as the top magnetic and electric dipole moments $d_{V,A}^\gamma$, the latter purely imaginary and CP violating. Both moments vanish in the SM at tree level, and can be mapped onto operator coefficients as follows:

$$\delta d_V^\gamma = \frac{\sqrt{2}}{\mathrm{e}}\,\mathrm{Re}\left[s_w C_{uW} + c_w C_{uB\phi}\right]\frac{m_t v}{\Lambda^2}\,, \tag{2.36}$$

$$\delta d_A^\gamma = \frac{\sqrt{2}}{\mathrm{e}}\,\mathrm{Im}\left[s_w C_{uW} + c_w C_{uB\phi}\right]\frac{m_t v}{\Lambda^2}\,. \tag{2.37}$$

2.2.5. ttg Couplings

The discussion of trilinear top–gauge couplings is concluded by the effective ttg vertex. Including the SM coupling, the effective vertex reads [46]

$$\Delta\mathcal{L}_{ttg} = -g_s\bar{t}\frac{\lambda^a}{2}\gamma^\mu t\,G_\mu^a - g_s\bar{t}\lambda^a\frac{\mathrm{i}\sigma^{\mu\nu}q_\nu}{m_t}\left(d_V^g + \mathrm{i}d_A^g\gamma_5\right)t\,G_\mu^a \tag{2.38}$$

with the top chromomagnetic and chromoelectric dipole moments $d_{V,A}^g$, which again vanish in the SM at tree level. As in the case of anomalous top–photon couplings, the effective ttg vertex does not receive on-shell corrections $\propto \gamma^\mu$, because the QCD charge is protected by the exact symmetry, and the off-shell terms rewritten in terms of contact interactions are completely independent of the $d_{V,A}^g$, cf. Eq. (2.18). The coupling relations to operator coefficients are

$$\delta d_V^g = \frac{\sqrt{2}}{g_s}\,\mathrm{Re}\,C_{uG\phi}\frac{m_t v}{\Lambda^2}\,, \qquad \delta d_A^g = \frac{\sqrt{2}}{g_s}\,\mathrm{Im}\,C_{uG\phi}\frac{m_t v}{\Lambda^2}\,. \tag{2.39a}$$

2.2.6. tth Couplings

The last remaining trilinear vertex of relevance within an effective approach to anomalous top couplings without new degrees of freedom is an anomalous top–Higgs

coupling tth. Following the standard procedure, we identify the potentially relevant operators as (2.1) and (2.2a)–(2.2c). However, as already explained in Sec. 2.1.1, the anti-hermitian part of (2.2a)–(2.2c) was shown to be redundant, cf. appendix B.2, while the hermitian part vanishes when the covariant derivative is replaced by an ordinary one [47]. What remains are anomalous contributions to the ordinary top–scalar Yukawa interaction coming from the operator (2.1), so that the effective $d = 6$ vertex reads [47]

$$\mathcal{L}_{tth} = -\frac{1}{\sqrt{2}}\bar{t}\big(Y_t^V + \mathrm{i}Y_t^A\gamma_5\big)\, t\, h\ , \tag{2.40}$$

where in the SM $Y_t^V \equiv Y_t = \sqrt{2}m_t/v$ is the standard Yukawa coupling and $Y_t^A = 0$ at tree level. The scalar and pseudoscalar couplings $Y_t^{V,A}$ are mapped onto operator coefficients as follows:

$$\delta Y_t^V = -\frac{3}{2}\mathrm{Re}\, C_{u\phi}\frac{v^2}{\Lambda^2}\ , \qquad\qquad \delta Y_t^A = -\frac{3}{2}\mathrm{Im}\, C_{u\phi}\frac{v^2}{\Lambda^2}\ . \tag{2.41}$$

It is by virtue of the rewriting procedure in [47] that the anomalous tth sector becomes as simple as in Eq. (2.40), and is entirely decoupled from the top–gauge sectors presented in the previous sections.

2.3. Contact Interactions

After discussing anomalous trilinear top vertices to gauge and scalar bosons in the previous section, it now remains to address four-fermion contact interactions in a general way, beginning with CC-like couplings and concluding with the NC ones. As a preliminary remark, however, note that the meaning of MFV is not as obvious any more as for the trilinear sector, because generally one can rearrange the spinors using Fierz identities. However, these rearrangements do not affect the physics content of a given basis but rather serve the purpose of choosing a minimal one, just as in the case of the EOM discussed in the previous section, cf. [48, 49]. For instance, one can always use Fierz rearrangements in combination with the completeness relations of the symmetry generators, Eq. (B.9), to rewrite the operators such that all fundamental group representation indices are contracted along with the Dirac indices within the same spinor bilinear. Of course, in the resulting basis the bilinears could be torn apart again by Fierz relations, but then one would either change the group contractions alongside, which just corresponds to a redefinition of the basis, or apply the completeness relations (B.9) afterwards in the hope to find superpositions of other operators already included in the basis: this corresponds to the procedure of redundancy reduction which was already applied to the utmost extent in [49] in order to find a minimal basis, cf. appendix B.2.

This basis has several advantages: firstly, the bilinears now come themselves in adjoint representations of the gauge symmetries, which simplifies the classification of the heavy physics generating the contact interactions in terms of SM quantum numbers, and also makes possible interferences with SM diagrams obvious. Secondly,

Figure 2.1.: Example loop diagrams inducing FCNC $b \to s$ transitions at leading order (heavy flavors indicated with a thick line). The left-hand side originates from a box diagram where one of the Ws gets contracted to a CC contact interaction, and on the right-hand side neutral bosons are contracted to a NC contact interaction inside a penguin, cf. Fig 2.2.

in this basis it is easy to see how to protect the flavor observables, i. e. how to implement MFV in a way quite similar to the Fermi interactions of Sec. 1.1.1. For instance, consider the case where just one heavy flavor is inserted. This often leads to FCNC $b \to s$ transitions at tree level because of the left-handed doublet structure of the SM. And even in the few cases where this restriction is avoided (e. g. when the heavy fermion is a right-handed up-type), all possible operators with one heavy line and many others with two heavy lines spoil the GIM suppression of the penguin and box diagrams generating e. g. rare b decays at leading order in the SM, cf. Fig. 2.1 (for more details, refer to Sec. 2.5.1). The only way to avoid this and thus reinstate MFV is to restrict the basis to those operators where the bilinears are generation diagonal,

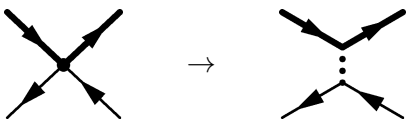

(2.42)

where thick lines indicate heavy flavor, and both continuous lines on the right-hand side are fermion bilinears in a specific group representation "glued together" by some heavy physics indicated by the dot propagator. As in the Fermi case, the result is that the neutral lines conserve flavor in the mass basis, whereas the charged lines become proportional to CKM elements, so that the GIM mechanism remains intact along the FCNC fermion lines in the diagrams of Fig. 2.1. Hence the discussion in the following subsections will be restricted to those operators out of the complete minimal set given in [49] which fulfill this requirement.

2.3.1. Charged Currents

Keeping the preceding arguments in mind, there are indeed not many operators left which potentially induce CC contact interactions. Apart from the contraction of left-handed vector bilinears in a weak isospin triplet, Eq. (2.7b), there are two scalar operators, Eq. (2.10), namely a color singlet and a color octet. (The mixed quark–lepton operators (2.11) can be safely dropped for reasons given in Sec. 2.5.2.) In

summary, the interaction Lagrangian receives the following four-fermion CC terms

$$\begin{aligned}\Delta\mathcal{L}_{\text{CC}} =& \frac{1}{\Lambda^2}\Big[V^{(3)}\big(\bar{b}\gamma_\mu P_L t\big)\big(\bar{u}_k\gamma^\mu P_L d_k\big) + \text{h.c.} && \text{(2.43a)}\\ &+ S_L^{(1)}\big(\bar{b}P_L t\big)\big(\bar{u}_k P_L d_k\big) + S_R^{(1)}\big(\bar{b}P_R t\big)\big(\bar{u}_k P_R d_k\big) + \text{h.c.} && \text{(2.43b)}\\ &+ S_L^{(8)}\big(\bar{b}\lambda^a P_L t\big)\big(\bar{u}_k\lambda^a P_L d_k\big) + S_R^{(8)}\big(\bar{b}\lambda^a P_R t\big)\big(\bar{u}_k\lambda^a P_R d_k\big) + \text{h.c.}\Big] && \text{(2.43c)}\\ &+ (\text{quark–lepton interactions})\,,\end{aligned}$$

where a universal coupling to the summed flavors k is assumed for simplicity. The corresponding relations to operator coefficients are

$$\begin{aligned} V^{(3)} &= 4\big(C_{qq}^{(3,33kk)} + C_{qq}^{(3,kk33)}\big) + g\text{Re}C_{qW}^{33}\,, && && \text{(2.44a)}\\ S_L^{(1)} &= -\big(C_{quqd}^{(1,33kk)}\big)^*\,, && S_R^{(1)} &= -C_{quqd}^{(1,kk33)}\,, && \text{(2.44b)}\\ S_L^{(8)} &= -\big(C_{quqd}^{(8,33kk)}\big)^*\,, && S_R^{(8)} &= -C_{quqd}^{(8,kk33)}\,. && \text{(2.44c)}\end{aligned}$$

Note that the normalization convention differs from the trilinear sector in such a way that now the mass scale is normalized by the (arbitrary) heavy scale Λ so that the connection to a heavy new physics propagator remains explicit, and the couplings in Eq. (2.44) do not receive a natural scale suppression any more. It is no surprise that in an independent assessment of the CC contact interactions we find again the contact term related to the trilinear tbW vertex, cf. Eqs. (2.27) and (2.43a), so that the respective couplings $V^{(3)}$ and V_L^{off} can be interchanged via the relation (2.28), without changing the physics content. This is just once more the statement that the operator basis contains redundancies which can be made explicit by the EOM: we have found three hermitian operator coefficients controlling just two independent coupling structures. However, any general approach to the CC sector should comprise both structures, in order to account for interference effects as well as a possible interrelation via underlying operator coefficients.

2.3.2. Neutral Currents

Obtaining the NC contact interactions is also straightforward, but there are more vector structures because the SM symmetries allow for a mixing of left-handed and right-handed NC currents. Hence, apart from the two scalar operators (2.10), one finds in total ten vector operators, namely two left-handed (2.7), four right-handed (2.8) and four mixed ones (2.9). In addition, the color-singlet operators (2.7), (2.8a) and (2.9a) are related to the trilinear NC sector via the EOM. Dropping the quark–lepton terms again, the overall set of possible coupling structures generated

by these operators is found to be

$$\Delta\mathcal{L}_{\text{NC}} = \frac{1}{\Lambda^2}\Bigg\{ \sum_{A,B=L,R} \sum_{f=u,d} \Big[\chi^{(1)}_{ABf} \big(\bar{t}\gamma_\mu P_A t\big)\big(\bar{f}_k \gamma^\mu P_B f_k\big) \tag{2.45a}$$

$$+ \chi^{(8)}_{ABf} \big(\bar{t}\lambda^a\gamma_\mu P_A t\big)\big(\bar{f}_k \lambda^a\gamma^\mu P_B f_k\big)\Big] \tag{2.45b}$$

$$+ \eta^{(1)}_L \big(\bar{t}P_L t\big)\big(\bar{d}_k P_L d_k\big) + \eta^{(1)}_R \big(\bar{t}P_R t\big)\big(\bar{d}_k P_R d_k\big) \tag{2.45c}$$

$$+ \eta^{(8)}_L \big(\bar{t}\lambda^a P_L t\big)\big(\bar{d}_k \lambda^a P_L d_k\big) + \eta^{(8)}_R \big(\bar{t}\lambda^a P_R t\big)\big(\bar{d}_k \lambda^a P_R d_k\big)\Bigg\} \tag{2.45d}$$

$$+ (\text{quark–lepton interactions}) \,.$$

In total, after resolving the isospin doublet structure (but still remaining universal in the summed flavor k), in addition to the four scalar structures η there are 16 vector structures χ instead of just one in the CC case, where one can choose $\chi^{(8)}_{LLu/d} = \chi^{(8)}_{RRu} = 0$ without loss of generality, because the corresponding operator is redundant, cf. Eq. (B.12). For reasons of brevity, and because the the NC contact couplings are of minor relevance to the further course of this thesis where the main phenomenological concern is with CC structures, the exact mapping of all these couplings onto operator coefficients is deferred to appendix B.3.

2.4. Coupling Relations

Before moving on to the phenomenological implications, the issue of coupling relations within the effective theory approach and the way they are taken into account in the WHIZARD implementation requires a dedicated discussion. Since the original effective operators by construction respect the full electroweak gauge symmetry $\mathbf{SU}(2)_L \times \mathbf{U}(1)_Y$, it is no surprise to find certain relations within the set of anomalous electroweak couplings of the heavy doublet (t, b) after spontaneous symmetry breaking. Starting from the symmetric operators comprising also weak isospin triplet representations, it is clear that anomalous CC and NC interactions are generated simultaneously, with nontrivial interrelations via common operator coefficients. For example, as can be readily verified by comparison of Eqs. (2.25) and (2.30), an anomalous CC contribution to V_L is directly related to the anomalous left-handed NC vector coupling X^L_{tt}. (For simplicity, resolve the EOM redundancy by setting either the coefficients of operators (2.2a)–(2.2c) or of operators (2.6a)–(2.6c) to zero, while turning on the associated contact interactions.) However, in addition one finds a left-handed bbZ vector interaction,

$$\Delta\mathcal{L} \propto X^L_{bb} \bar{b} \not{Z} P_L b \,, \tag{2.46}$$

which is stringently constrained by LEP data. But note that the contributions from the isospin triplet operators to X^L_{bb} switch their sign with respect to X^L_{tt} because of the eigenvalue of the τ_3 generator. Therefore, a cancellation is possible which allows to turn on δV_L, but respecting all existing bounds then necessarily implies [46, 84]

$$\delta X^L_{tt} = 2\delta V_L \,. \tag{2.47}$$

This relation by default is automatically enforced in WHIZARD, but can be switched off optionally.

Similarly, Eqs. (2.25), (2.30) and (2.36) highlight that the anomalous CC and NC tensor couplings are directly related to each other. For instance, consider the complex CC coupling g_R and the four real top NC couplings $d^Z_{V/A}$ and $d^\gamma_{V/A}$, in total six real parameters controlled by just two complex operator coefficients, namely C_{uW} and $C_{uB\phi}$. In WHIZARD, this is by default accounted for by fixing $d^Z_{V/A}$ from the other ones, because they are hardest to access experimentally. The situation for g_L is even more restrictive: If the operator $O_{dB\phi}$, cf. Eq. (B.8a), is dropped because in a strict sense it does not contribute to the anomalous top sector, then all four NC bottom couplings are uniquely fixed by g_L, which can also be enforced in WHIZARD. Once the trilinear tensor couplings are consistently fixed from user input according the rules just stated (no specific restriction applies to the anomalous QCD couplings $d^g_{V/A}$), the associated quartic fermion–gauge couplings such as $tbWA$ or $ttWW$ are also fixed as dictated by the gauge invariance of the underlying operators, cf. Eq. (2.22). The corresponding Ward identities thus convey a possibility to validate the implementation, as explained in Sec. 3.3.

In conclusion, it is impossible to vary the anomalous CC couplings in a consistent way within the effective operator approach without getting anomalous NC top and bottom couplings. In some cases one could include additional operators to fine-tune these effects away, but this generally implies an extended anomalous bottom sector, so that a study which is sensitive to these structures would necessitate a dedicated reassessment of the parametrization.

2.5. Phenomenology

After setting up the effective operator basis and discussing the resulting anomalous top couplings as well as their interrelations, the last section of this chapter shall be devoted to a short general introduction to a selection of sensitive observables, and the phenomenological impact of the anomalous couplings on them.

2.5.1. Flavor Observables

Before turning to direct searches at high energy colliders for the rest of the thesis, the important area of low energy flavor observables shall not remain unmentioned, because the bounds derived from them are complementary to collider results, and the numerical values already obtained from rare B decay constraints [85–87] are competitive to respective LHC results [81]. However, let us first introduce the general procedure, roughly following [67, 85, 88].

As explained in Sec. 1.1.3, within the SM all neutral fermion currents are by construction flavor-diagonal at tree level, while charged currents interacting with the $W^\pm$ bosons can induce generation transitions in the quark sector via the off-diagonal elements of the CKM matrix V (unlike the lepton sector in the limit of vanishing neutrino masses). Hence, neutral decays of b quarks (or rather B mesons containing such a quark) are loop-suppressed in the SM, and therefore expected to

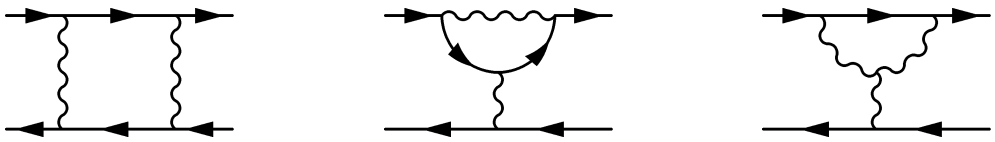

Figure 2.2.: Leading order SM loop diagrams inducing the FCNC transition $b \to s+X$: box diagram (left) and penguin diagrams (center and right). The lower fermion lines correspond to any fixed external quark or lepton mass state, and the neutral gauge boson in the penguins can also be emitted on-shell, if it is a photon.

be extremely rare compared to charged decays. However, if you consider the leading order one-loop diagrams generating this transition, cf. Fig. 2.2, it is clear that an incoming b mass state leads to a sum over all up-type mass states running in the loop, multiplied by CKM elements. Now since V is unitary,

$$V^\dagger V = \mathbf{1} \qquad \to \qquad \sum_{i=u,c,t} V_{ij}^* V_{ik} = \delta_{jk} \,, \tag{2.48}$$

the loop diagrams identically vanish in the limit of degenerate masses, so any finite contribution must be proportional to the splitting of the up-type masses. Since mass insertions flip the chirality, but left-handed currents are needed to couple to the W, one requires two mass insertions at leading order, so the transition will be $\propto V_{tb}V_{ts}^* m_t^2$ at least. This subtle interplay was originally proposed in 1970 by Glashow, Iliopoulos and Maiani [7] (and thereafter called the GIM mechanism) to explain the relative suppression of $\Delta S = 2$ transitions compared to $\Delta S = 1$ ones, while at the same time postulating the existence of a second up-type quark as a doublet partner to the s, namely the charm.

The impact on the rare B decays is twofold: due to the CKM structure required for the mechanism, the decay width becomes extremely sensitive to BSM physics with a non-minimal flavor structure, i. e. allowing for generation transitions which do not explicitly come with CKM elements. But even if the new physics obeys the MFV paradigm, any anomalous contributions to the heavy flavor couplings will also cause large effects because of the large top mass dominating the leading order decay amplitude. In order to quantify this, one first moves on to an effective low energy theory at the B mass scale by integrating out the heavy gauge bosons and the top. As explained in more detail in Sec. 1.2.2, this is done by matching their effects up to a fixed loop order (one loop in this case) onto effective operators at the respective thresholds, whose coefficients can then be evolved down by RGE methods. As a result, one finds the effective low energy Lagrangian [87] (cf. [88])

$$\mathcal{L}_{\text{eff}} = \mathcal{L}_{\text{QCD}\times\text{QED}} + \frac{4G_F}{\sqrt{2}} V_{tb}V_{ts}^* \sum_i C_i O_i \,, \tag{2.49}$$

where the O_i encode effective $\Delta B = 1$ transitions $b \to s+X$ ($X = \gamma, g, \ell\ell, qq$). In the

SM, the C_i are all loop suppressed and finite at leading order due to the additional GIM cancellation.

If the SM is replaced by an effective BSM Lagrangian above m_t, additional non-SM insertions contribute to the loops at the matching scale, making the C_i become themselves functions of the BSM coefficients. For instance, consider anomalous top couplings $\vec{g}$ contributing to the penguin diagram (with an on-shell massless vector boson, for simplicity)

$\delta C_i(\vec{g}) \sim$ 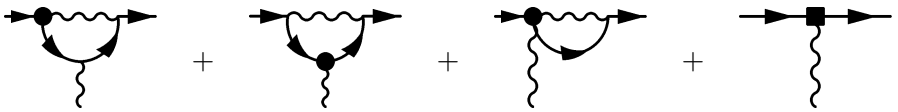 (2.50)

where blobs indicate anomalous coupling insertions. As discussed in Sec. 2.4, trilinear CC insertions can be disentangled neither from NC insertions nor from quartic insertions due to gauge invariance, which has been accounted for in Eq. (2.50). Furthermore, BSM insertions may produce additional loop momenta in the numerator, cf. Eq. (2.24), potentially making the diagrams divergent. Therefore, one in principle has to further extend the operator basis in order to provide the tree-level FCNC counter-term included in Eq. (2.50). However, it is argued in [87] that these operators can be constrained independently, cf. [89], so that the B decays provide a clean signature of new physics obeying MFV. Consequently, UV divergent diagrams can be renormalized at $\mu = m_W$ in a given scheme (typically $\overline{MS}$), while the divergent parts govern the RGE running of the $C_i(\vec{g}, \mu) \sim \log(\mu/m_W)$ down to $\mu = m_b$.

It is then straightforward to express the B decay branching ratios in terms of the respective FCNC insertions $C_i(\vec{g}, \mu)|_{m_b}$, (usually assuming only the SM–NP interferences linear in $\vec{g}$ at leading order in $1/\Lambda^2$) and turn the experimental results into bounds on $\vec{g}$. For instance, consider the decay channels $B \to X_s\gamma$ and $B \to X_s\mu^+\mu^-$, with experimental constraints [90, 91]

$$\mathcal{BR}(B \to X_s\gamma)_{E_\gamma > 1.6\,\mathrm{GeV}} = (3.55 \pm 0.26) \times 10^{-4}\,, \tag{2.51a}$$

$$\mathcal{BR}(B \to X_s\mu^+\mu^-)_{\text{low } q^2} = (1.60 \pm 0.50) \times 10^{-6}\,. \tag{2.51b}$$

Since the SM contributions to the C_i are mostly real [87], the branching ratios constrain the real parts of $\vec{g}$. Resulting bounds based on the numbers in Eq. (2.51) are displayed in Fig. 2.3 taken from [87], where the couplings translate to the ones introduced in Eq. (2.24) as

$$V_L = V_{tb}^* \kappa_{LL}^{(\prime,\prime\prime)*}\,, \quad V_R = V_{tb}^* \kappa_{RR}^*\,, \quad g_L = V_{tb}^* \kappa_{LRb}^*\,, \quad g_R = V_{tb}^* \kappa_{LRt}^{(\prime)}\,, \tag{2.52}$$

The CKM elements appear because naturally in a flavor study the heavy flavors cannot be decoupled as approximated in Sec. 2.2.2. Ref. [87] also provides further details of the study, such as scale dependence, combined bounds, and comparisons to direct LHC constraints. However, ref. [87] does not include the operator $O_{uB\phi}$ (2.4c) but rather fixes the NC couplings from the CC ones. As discussed in Sec. 2.4, including it would relax this relation, thus allowing to shuffle anomalous contributions among the two different final states in Eq. (2.51), which would certainly influence

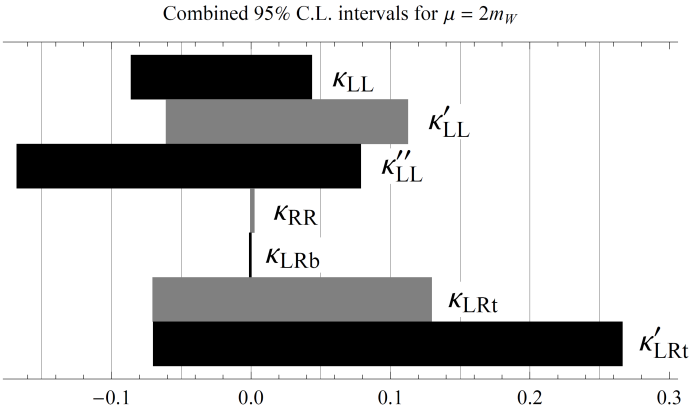

Figure 2.3.: Combined 95 % C.L. bounds from the measurements (2.51) on individual real parts of anomalous tbW couplings for $\mu = m_W$ (taken from [87]), cf. Eq. (2.52) for comparison to Eq. (2.24).

the combined bounds. Finally, one may remark that anomalous four-fermion contact interactions in the MFV scheme as discussed in Sec. 2.3 have not been considered so far in the literature.

2.5.2. Top Decay

After this short excursion to indirect effects on flavor observables, the attention is now shifted towards direct observables related with top production above the mass threshold at high energy colliders. However, before discussing the production mechanisms, we will first address an issue common to all of them, namely the decay mechanism. Due to the structure of the SM which forbids FCNC interactions at tree level, the top decay is governed by the electroweak CC channel $t \to Wb$, where the b flavor dominates the final state because of the approximately decoupled heavy generation in the CKM matrix [92]. The W boson then decays further into fermion pairs, either hadronically or leptonically.

Experimentally, the most feasible decay mode is the one with light leptons, $t \to \ell\nu b$ ($\ell = e, \mu$), because of its clean signature. Therefore, it will be of main interest in the phenomenological part and hence also here. Another feature of this mode is that the lepton angle is sensitive on the W polarization and thus on the chiral structure of the top decay vertex. More precisely, starting in a given top rest frame, consider the angle θ^*_ℓ between the lepton 3-momentum boosted into the W frame and the quantization axis given by the W boson (or minus b quark) 3-momentum. With respect to this angle, the normalized differential decay width reads [93]

$$\frac{1}{\Gamma}\frac{\mathrm{d}\Gamma}{\mathrm{d}\cos\theta^*_\ell} = \frac{3}{8}(1-\cos\theta^*_\ell)^2 F_L + \frac{3}{8}(1+\cos\theta^*_\ell)^2 F_R + \frac{3}{4}\sin^2\theta^*_\ell F_0 \tag{2.53}$$

with the helicity fractions $F_i \equiv \Gamma_i/\Gamma$ which correspond to the individual helicity states of the W, and obey the relation $\sum F_i = 1$. Thus, in principle the helicity structure of the tbW vertex can be extracted in direct top measurements simply

from a fit to the θ_ℓ^* distribution [81]. Within the SM, employing the WHIZARD default parameter setup (cf. appendix C) the helicity fractions at tree level take the values $F_L = 0.698$, $F_0 = 0.302$ and $F_R = 2.9 \times 10^{-4}$.

In terms of anomalous top couplings, the top decay potentially is sensitive to any anomalous CC interaction out of Eqs. (2.24) and (2.43). However, concerning the contact interactions (2.43) it is argued in [48] that the SM–NP interference almost exactly cancels due to a sign change of the W propagator at the pole (which is absent in the contact amplitude), so the leading contribution comes from the squared NP amplitude. Yet this term also is kinematically suppressed $\propto m_W^2/\Lambda^2$, leading to an overall suppression $\Gamma_{\text{NP}}/\Gamma_{\text{SM}} \lesssim 10^{-6}(\text{TeV}/\Lambda)^4$ [48], hence it is usually a good approximation to entirely neglect the contact interactions in an isolated assessment of Γ_t and expand the width as a function of the anomalous trilinear couplings given in Eq. (2.24a)–(2.24b), cf. analytical expressions e. g. in [94]. (This is precisely the reason why the quark–lepton operators contributing only to the decay were dropped in Sec. 2.3.1.) Furthermore, the normalization (i. e. the total decay width) is relatively unconstrained, with the best measured value to date found in [95], whereas the relative helicity fractions F_i can be determined with high precision, so that it is feasible to work in a setup fixing $V_L = 1$ and constraining the relative contributions of V_R and $g_{L,R}$, leaving the overall normalization to another measurement. Using the analytical expressions for the partial widths $\Gamma_i(\vec{g})$ in terms of the anomalous couplings, it is straightforward to convert the limits on the F_i into constraints on $\vec{g}$. For example, the ATLAS collaboration published a measurement [81]

$$F_0 = 0.67 \pm 0.03\,(\text{stat.}) \pm 0.06\,(\text{syst.})\,, \tag{2.54a}$$
$$F_L = 0.32 \pm 0.02\,(\text{stat.}) \pm 0.03\,(\text{syst.})\,, \tag{2.54b}$$
$$F_R = 0.01 \pm 0.01\,(\text{stat.}) \pm 0.04\,(\text{syst.})\,. \tag{2.54c}$$

which yields the following 95 % C.L. limits on the anomalous couplings

$$\text{Re}(V_R) \in [-0.20, 0.23]\,, \tag{2.55a}$$
$$\text{Re}(g_L) \in [-0.14, 0.11]\,, \tag{2.55b}$$
$$\text{Re}(g_R) \in [-0.08, 0.04]\,, \tag{2.55c}$$

assuming only one of them non-zero at a time. The comparison to the respective numbers from B decays given in Fig. 2.3 reveals a neat complementarity between the two assessments, namely that the flavor observables are particularly sensitive to V_R and g_L (by a rough order of magnitude above V_L and g_R) while the top decay is most sensitive to g_R, cf. [78, 94].

Finally, note that due to the large top mass the angular distributions of the decay products also carry information on the polarization of the top. Quite similar to the previous definition of θ_ℓ^*, in the top rest frame one can define additional 3-momentum angles θ_X of the top decay products ($X = \ell, \nu, b$) against an arbitrary quantization axis z. The normalized differential decay width with respect to these angles is [94, 96]

$$\frac{1}{\Gamma}\frac{\mathrm{d}\Gamma}{\mathrm{d}\cos\theta_X} = \frac{1}{2}\left(1 + \rho_z \alpha_X \cos\theta_X\right) \tag{2.56}$$

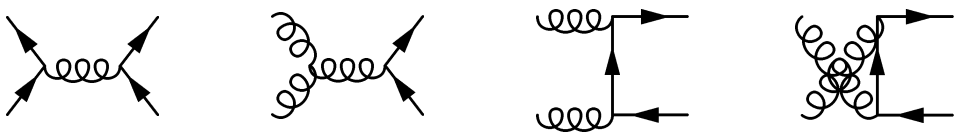

Figure 2.4.: Leading order $t\bar{t}$ production diagrams for hadronic initial states.

with the top polarization $\rho_z \in [-1, 1]$ along the quantization axis z, and the so-called "spin analyzing power" α_X of the decay product X. In the SM, they take the values

$$\alpha_\ell = 1\,(0.998)\,, \qquad \alpha_\nu = -0.32\,(-0.33)\,, \qquad \alpha_b = -0.41\,(-0.39) \tag{2.57}$$

at LO [97] (NLO [98–100]) in α_s, but of course, in general they depend on NP contributions. However, as another consequence of the argument above that the contact interactions play no role at the decay vertex, the α_X can be expressed model independently as a function of the anomalous trilinear tbW couplings only, $\alpha_X \equiv \alpha_X(V_L, V_R, g_L, g_R)$ (LO analytical expressions given in [101]). With the θ_X, one can further define asymmetries

$$A_X = \frac{N(\cos\theta_X > 0) - N(\cos\theta_X < 0)}{N(\cos\theta_X > 0) + N(\cos\theta_X < 0)} = \frac{1}{2}\rho_z\alpha_X\,, \tag{2.58}$$

where N denotes measured event numbers with the respective property. Obviously, the A_X are sensitive to the product $\rho_z\alpha_X$, but as explained before the α_X can in principle be fixed independently by W helicity fractions (up to a normalization), so that particularly A_ℓ becomes a powerful observable to measure the top spin polarization ρ_z, where the optimal polarization axis z depends on the given production mechanism.

2.5.3. Top Pair Production

Finally turning to direct top production above the threshold, let us first address top pair production at hadron colliders such as Tevatron and LHC. With hadronic initial states, top pairs are predominantly produced via QCD processes (cf. Fig. 2.4 for respective tree level diagrams), whereas quark annihilation dominates at the Tevatron while gluon fusion is the largest contribution at the LHC, due to the different pdfs. Because of its high relevance for both colliders (the Tevatron was designed to discover the top, while the LHC produces them abundantly due to the increased c.m.s. energies), much theoretical effort over the past two decades has gone into the precise calculation of total as well as differential $t\bar{t}$ production cross sections, from the first NLO computation in 1988 [102] until the full NNLO (QCD) result published only this year [103], cf. [104] for a dedicated review. Also NLO corrections connecting production and decay of the top quarks were taken into account [105]. Experimentally, the $t\bar{t}$ final states are classified into fully hadronic, fully leptonic and semileptonic, according to the combination of possible top decay modes. An overview over all available measurements, divided into final states and CMS energies

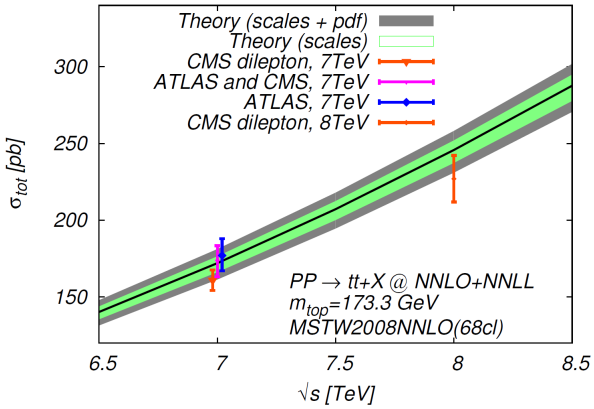

Figure 2.5.: Comparison of theoretical NNLO (QCD) result and LHC measurements of the total $t\bar{t}$ production cross section (taken from [103]).

from various colliders and experiments, can be found in [106], cf. Fig. 2.5 for a comparison of theoretical and LHC results.

In the literature, anomalous couplings or, more generally, effective $d = 6$ operators have been considered with respect to several different aspects of $t\bar{t}$ production. In the most straightforward approach [107–109], the total on-shell production cross section can be expressed in terms of anomalous top–gluon couplings as parametrized in Eq. (2.38). The analysis is facilitated by the fact that in the minimal operator basis the QCD sector is completely separated from the electroweak sector, so that including the anomalous QCD dipole moments $d^g_{V,A}$ of Eq. (2.38) does not affect the top decay. Hence, the insertion into LO on-shell amplitudes already produces a solid estimate of NP contributions. Diagrammatically, one has to insert the anomalous trilinear ttg vertex wherever possible in the diagrams given in Fig. 2.4. In the gluon fusion amplitude, an associated $ttgg$ contact diagram must also be inserted as required by gauge invariance to fix the Ward identities of the gluons, cf. Eq. (2.22). In [108, 109], expected sensitivities from combined Tevatron and LHC results are reported around $|d^g_V| \lesssim 0.1$ resp. $|d^g_A| \lesssim 0.15$, in the normalization of Eq. (2.38), with no actual measurements from the collider experiments available so far.

Another interesting observable in the $t\bar{t}$ sector is the forward-backward asymmetry A_{FB} at the Tevatron, which is defined identical to A_X in Eq. (2.58): just replace θ_X by the polar angle θ_t of the top against the beam axis in the lab frame. In the SM, the largest contribution to A_{FB} is induced only at NLO by an interference between QCD amplitudes, and amounts to $\sim 5\,\%$ at leading $\mathcal{O}(\alpha_s^3)$ [110] (electroweak contributions $\ll 1\,\%$). However, the Tevatron experiments CDF and DØ have reported an intriguing 2σ deviation from this value [111–113], where the absolute size of A_{FB} and particularly the growing discrepancy with the invariant mass $M_{t\bar{t}}$ have prompted various NP explanations in the literature (cf. [114] for an overview). From the EFT perspective with MFV, there are specific linear combinations of color-octet operators contained within the NC contact interactions, Eq. (2.45), which could induce such an effect by a tree level SM–NP interference [115]. Dropping non-MFV contact

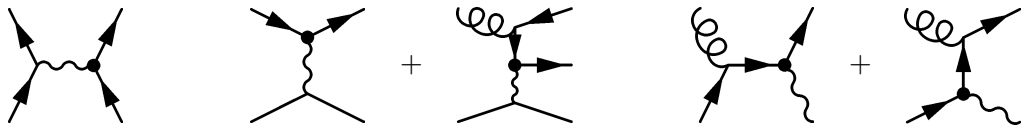

Figure 2.6.: Diagrams contributing to on-shell single top production at tree level (possible anomalous tbW insertions from Eq. (2.24) marked by a dot): s channel tb production (left), t channel $tj + tbj$ production (center) and associated tW production (right).

operators after the rewriting in [49] (cf. appendix B.2), the asymmetry direction in terms of the minimal basis introduced in 2.1.2 reads

$$A_{\mathrm{FB}} \sim C_{ud}^{(8,33kk)} - C_{qd}^{(8,33kk)} - C_{qu}^{(8,33kk)} - C_{qu}^{(8,kk33)} \,. \tag{2.59}$$

However, as argued in [114] an interpretation in terms of a UV completion containing axigluons is problematic, because in order to produce the correct sign of A_{FB} they would either have to be rather light ($< 1\,\mathrm{TeV}$) and hence broad to evade existing bounds (ignoring the fact that the EFT approach is not applicable any more with such light new degrees of freedom), or they would have to couple flavor non-universally to the quarks (i. e. flipping sign between light and heavy flavors). Quite apart from such considerations, the LHC experiments ATLAS and CMS have looked for similar patterns in the LHC version of A_{FB}, defined as the charge asymmetry

$$A_{\mathrm{C}} = \frac{N(\Delta|\eta| > 0) - N(\Delta|\eta| < 0)}{N(\Delta|\eta| > 0) + N(\Delta|\eta| < 0)} \,, \tag{2.60}$$

using pseudorapidity differences $\Delta|\eta| \equiv |\eta_t| - |\eta_{\bar{t}}|$ because of the symmetric pp initial state. No significant deviations from SM predictions have been found [116, 117].

Finally, note that $t\bar{t}$ studies also form the basis for other anomalous coupling searches such as $tt\gamma$ [118], ttZ and tth [119, 120], where the final state comprises a boson resp. its decay products, in addition to the $t\bar{t}$ system. Although the cross section generally is very small for these processes, these couplings are otherwise very difficult to assess experimentally, and the associated production with a top pair might turn out to be the most promising approach, at least at the LHC. As an alternative, precise measurements of the Higgs production and decay modes have recently been discussed as a probe of anomalous ttg [121] and $tt\gamma$ [122] couplings.

2.5.4. Single Top Production

In contrast to top pair production, the main feature of single top production is that it takes place exclusively via electroweak CC interactions. These two modes are thus complementary in their sensitivity to top NP patterns. Single tops are produced at the LHC (and Tevatron) in three different channels, namely s channel tb production, t channel tj production (where j denotes a light hadronic jet), and associated tW production, cf. Fig. 2.6. Hence, apart from the decay mode of

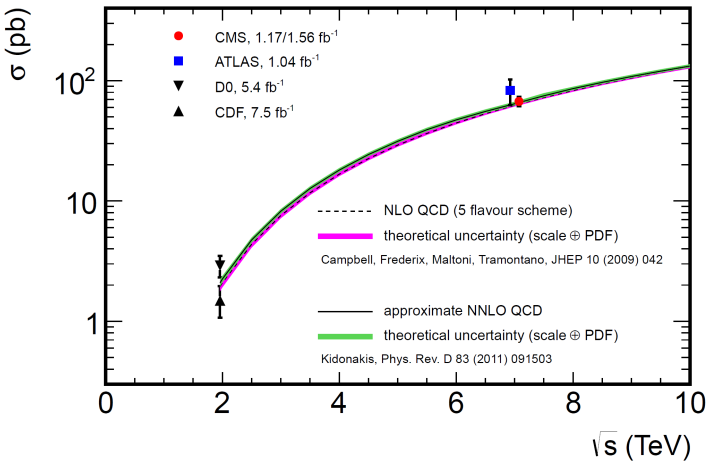

Figure 2.7.: Comparison of theoretical NLO and NNLL (QCD) results with Tevatron and LHC measurements of the total single top t channel production cross section (taken from [27]).

the top, the single top final states at the detector level are classified according to these production channels. While tW production stands a little apart because of its additional heavy resonance, the tb and tj channels are much more interweaved because of their rather similar final state patterns, where the discrimination power largely depends on the b tagging performance of the detector, cf. Sec. 4.2.2. An additional complication of the tj and tW channels is that they require an initial b quark at leading order, cf. Fig. 2.6, which in the proton pdfs comes from a gluon splitting $g \to b\bar{b}$. However, this leads to some double counting of phase space regions once the radiation correction diagrams (e. g. the $t\bar{b}j$ final state in Fig. 2.6) are included in the hard parton level matrix element. While various well-defined procedures exist in the literature to resolve this problem in the t channel (refer to Sec. 4.1.2 for details), the tW channel is problematic because the radiative correction diagram tWb contains $t\bar{t}$ contributions—roughly an order of magnitude larger than the actual single top signal—whose consistent removal still is a topic of vivid discussion (cf. e. g. [106]). Nevertheless, approximate NNLO (QCD) calculations exist for total on-shell production cross sections in all three channels [123–125]. Values for $\sqrt{s} = 14\,\text{TeV}$ and $m_t = 173\,\text{GeV}$ are listed in Tab. 2.1 for reference, because we will later rely on them for the SM normalization. In addition, a full NLO calculation of the t channel including off-shell and non-resonant effects has recently been published [126]. Experimentally, the LHC experiments have claimed observations of the tW channel [23, 24] and the t channel [25–27] signal with significances above 3σ resp. 5σ, whereas the s channel is not significant yet [127]. However, very recently the Tevatron experiment DØ was the first to claim a 3σ evidence of the s channel signal [28]. A comparison of the calculation and experimental results for the t channel is displayed in Fig. 2.7.

Turning to anomalous CC interactions, it is clear from Fig. 2.6 that in the limit of on-shell production only one insertion of the anomalous tbW vertex, Eq. (2.24), is

$\mathcal{O}(\alpha_s)$	s channel		t channel		tW channel
	σ_t	$\sigma_{\bar{t}}$	σ_t	$\sigma_{\bar{t}}$	$\sigma_t = \sigma_{\bar{t}}$
WHIZARD LO	4.81	2.94	134.8	79.1	26.5
NLO [128–130]	6.56 ± 0.38	4.09 ± 0.24	$155.9^{+5.8}_{-6.3}$	$90.7^{+3.4}_{-3.7}$	37
NNLL [123–125]	$7.93^{+0.34}_{-0.31}$	$3.99^{+0.15}_{-0.22}$	151^{+5}_{-3}	92 ± 3	$41.8^{+1.8}_{-2.6}$

Table 2.1.: Single top LHC cross sections for $\sqrt{s} = 14\,\text{TeV}$ and $m_t = 173\,\text{GeV}$, at different orders in α_s (in [pb], including pdf and scale uncertainties beyond LO while employing the WHIZARD default setup at LO, cf. appendix C).

possible. Hence the respective on-shell cross sections can depend only quadratically on the corresponding coupling factors $\vec{g}$. However, as explained in Sec. 2.5.2 the top decay is also dominated by the tbW vertex, thus allowing for up to two anomalous insertions into the full amplitude including decay. Therefore, the on-shell quadratic approximation is valid only if the narrow width approximation (NWA) holds, where the decay insertions in the numerator cancel against the width dependence $\Gamma_t(\vec{g})$ in the denominator. In general, this works well as long as the kinematic variables are integrated over the full phase space in the numerator, thus recovering Γ_t after the propagator has been replaced by a delta function. However, since this is not the case for final state momenta which have to to be detected inside the collider experiments, the validity of this approximation as well as possible consequences on the bounds derived on $\vec{g}$ from single top cross section measurements will be addressed in detail in Sec. 5.1.

Apart from anomalous trilinear tbW couplings, single top production is also sensitive to CC four-fermion contact interactions as parametrized in Eq. (2.43). However, as argued in Sec. 2.5.2 these insertions can be neglected in the decay already at the amplitude level, so that the quadratic approximation trivially holds for the corresponding cross sections, without having to bother about NWA as in the trilinear case. Furthermore, the contact amplitudes are expected to produce rather different kinematics than the SM amplitude, even in the on-shell case. In conclusion, from the kinematic point of view it is justified to perform dedicated studies addressing only trilinear couplings (Sec. 5.1), or only contact interactions (Sec. 5.2), and to reduce the underlying operator set accordingly. Still, it was argued in Sec. 2.2.2 that the contact interaction $\sim V_L^{\text{off}}$, cf. Eq. (2.24), plays a special role because it interferes with the SM amplitude, and potentially shares an operator coefficient with an anomalous δV_L, which is why it is included in both phenomenological studies of Ch. 5.

As a concluding remark to this section, remember the spin asymmetries A_X introduced in Sec. 2.5.2, particularly A_ℓ. They generally depend on the product $\rho_z \alpha_X$, where both factors are affected by anomalous CC contributions. Yet once the spin analyzers α_X are fixed from W helicity fractions with sufficient precision, A_ℓ probes the top spin polarization ρ_z, if a sensitive quantization axis z can be found. In the

single top t channel, ref. [101] proposes the 3-momentum direction of the light jet in the top frame for such an axis, because the SM predicts highly polarized tops, $\rho_z \in [0.9, 1]$ along this axis [131], which is of course correlated with the chiral structure of the production vertex (purely left-handed in the SM). This will be exploited in Sec. 5.2 to probe the chiral structure of the anomalous contact interactions.

3. Implementation and Validation

In general, high energy collider experiments are a rather complex issue, particularly if the initial state to be collided is hadronic as in the case of the Tevatron (proton–anti-proton) or the LHC (proton–proton). However, since a detailed knowledge about the physical processes mapping the initial collisions onto detector hits is paramount for the interpretation and conclusions to be drawn from actual experiments, a powerful phenomenological machinery has been developed along with the actual collider machines over the past decades to describe and numerically simulate these processes.

An obvious complication is posed by the fact that a good part of the final states, and in our case also the initial state, is dominated by hadrons, i. e. complicated bound states of QCD, which becomes strongly coupled and cannot be handled perturbatively at low energies. However, the counterpart of this "confinement" is asymptotic freedom, i. e. the decoupling of QCD at increasing energies, which together with the factorization theorems of QCD [132] provides the possibility to factorize the entire process into subprocesses governed by different energy scales. At collision energies far above the proton mass, the initial (anti-)protons can thus be approximated simply as bunches of decoupled colored constituents, or partons, consisting of the light quark flavors and gluons. The distribution of the total proton momentum among these partons can be described heuristically by parton distribution functions (pdfs) to be determined from experiment. As a first result, a proton–proton collision decomposes into a hard scattering of two high-energetic partons, whose initial momenta are accounted for by a convolution with the pdfs. The hard $2 \to n$ process itself can be computed perturbatively by quantum field theory methods, leading to a hard final state with leptons and again partons. Although these partons will eventually have to hadronize again to from an uncolored final state, at sufficiently high energies the individual partons can be identified with individual hadronic responses or jets in the detector; the simplified process up to this stage is commonly referred to as parton level.

This is the special field of the Monte Carlo event generator package WHIZARD [56], which was particularly designed to handle the hard scattering at the core of the process to leading perturbative order including BSM physics, and which is used throughout this thesis. Therefore, the rest of this chapter is devoted to the package, with a general introduction in the next section, followed by the implementation of anomalous top couplings, in Sec. 3.2, and its validation in Sec. 3.3. The whole rest of the machinery, i. e. the steps from parton level differential cross sections to fully simulated detector level events will be addressed in Ch. 4.

3.1. WHIZARD—A Monte Carlo Event Generator

The WHIZARD package basically consists of two components, namely O'MEGA [133] for the generation of the hard parton level matrix elements (Sec. 3.1.1), and the WHIZARD core program which performs the phase space integration over the matrix element (Sec. 3.1.2) and delivers all the necessary infrastructure, from pdf handling to output formatting and interfaces. To that end, WHIZARD comes with a dedicated scripting language called SINDARIN to facilitate the user control of the entire package functionality in one script file, from the process definition in a given model to event analysis and histogram production.

3.1.1. Matrix Element Generation with O'MEGA

Originally, O'MEGA was a standalone tool intended to generate efficient code for the numerical handling of tree level matrix elements based on model specific Feynman rules to be given as input. The necessity to optimize this step immediately becomes obvious upon counting the number of Feynman diagrams $F(n)$ contributing to a process with n external legs in the brute-force diagrammatic approach. For instance, consider the simplest interacting field theory imaginable, namely unflavored scalar ϕ^3 theory, containing just one trilinear vertex and one propagator[1]. $F(n)$ can simply be obtained recursively, by asking for all possibilities to build an $(n+1)$-point function out of the n-point one via attaching another external line. Diagrammatically, this corresponds to [133]

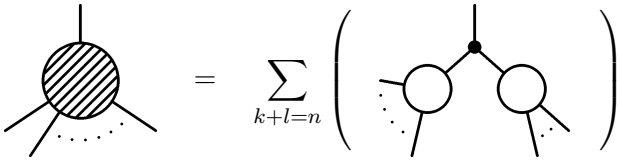

(3.1)

where the sum runs over all possibilities to split the external momenta into two connected subsets A and B. In the simplest nontrivial case, one starts with the 3-point function with just one diagram and finds the three well-known $2 \to 2$ diagrams with kinematic configurations s, t and u. Obviously, in general one can thus recursively construct any possible kinematic topology contributing to a given number of external momenta, where in each step the number of lines in a diagram is increased by two, and the number of new diagrams found depends on the number of the ones already constructed, times the number of lines contained in each of them before the insertion. By induction, it is easy to see that this leads to a factorial growth of the number of diagrams [133],

$$F(n) = (2n-5)!! = (2n-5)(2n-7)\cdots 5 \cdot 3 \cdot 1 \,. \tag{3.2}$$

[1] The generalization to more complex theories such as QED (postponing the issue of quartic couplings for the moment) is straightforward: just "dress" the scalar with additional quantum numbers (such as Lorentz representations, flavors, etc.), which does not affect the momentum combinatorics.

While this is still controllable for small numbers of external legs $n \lesssim 6$ (the working basis for the first automated matrix element tools such as CALCHEP [134]), the complexity runs very fast out of border when n is further increased (e. g., $F(8) = 10395$).

However, a naive diagrammatic computation is extremely redundant, as can be seen by a slight physical reinterpretation of Eq. (3.1): Regard the objects A and B on the right-hand side not as mere sums of diagram pieces, but rather as *one-particle off-shell wave functions* (1POW), i. e. "almost physical" amplitudes [133] where all but the $(n+1)$-th external line are already amputated via the LSZ reduction procedure. From this point of view, Eq. (3.1) represents a recursive instruction to find all of these 1POWs, but it also highlights the inherent redundancy, because in every iteration step two 1POWs of lower order are fused into a new off-shell line by a trilinear vertex. Exploiting this redundancy boils down to computing each individual 1POW exactly once, and reusing the result every time it reappears in the recursion. The computational effort is thus reduced from computing $F(n)$ diagrams to computing $P(n)$ different 1POWs, where the total number $P(n)$ is simply given by all possibilities to select a subset of k external momenta out of the n available ones,

$$P(n) = \sum_{k=1}^{n-1} \binom{n}{k} = 2^n - 2 \,, \tag{3.3}$$

which grows only exponentially with n [133].

The remaining task for O'MEGA is to express the desired matrix element as a sum over products of 1POWs, instead of a sum over all diagrams. Diagrammatically, this would correspond to promoting in each diagram one vertex to a so-called *keystone* [135], and representing the whole diagram as one term contained in a product of 1POWs fused together at this keystone. The particular choice of a set of keystones thus defines the representation of the entire amplitude in terms of a *directed acyclical graph* (DAG), which essentially is just a prescription how to combine common subexpressions (namely the 1POWs) in order to obtain the full sum in a maximally factorized way. Yet this choice of keystones is not unique, and optimizing it would imply again operations on the full set of diagrams. However, Eq. (3.1) already defines all possible 1POWs recursively, and it was shown [135] that a corresponding DAG can be constructed directly in a consistent way without double counting, by selecting sets of keystones according to additional ordering principles (i. e. taking the maximally symmetric [135], or in special cases maximally asymmetric ones [136]). The output of O'MEGA is a FORTRAN program implementing the DAG in a human-readable way, to numerically compute the matrix element as a function of n on-shell momenta. This program is linked to the WHIZARD core program, which takes care of the phase space mapping and integration.

3.1.2. Monte Carlo Integration

As a result of the previous section, we have a numerical representation of the squared matrix element as a function $f(p)$, where p labels all valid phase space points. The

remaining task is to integrate $f(p)$ over the entire kinematically accessible phase space Ω. For an n-particle scattering process, Ω is a complicated hypersurface inside the $4n$-dimensional configuration space of the external momenta, constrained by on-shell conditions and momentum conservation. Subtracting all constraints (n mass shells, 4 conserved momentum components, and one angle in our case due to the rotation invariance of the scattering experiment around the beam axis), we still have $d(\Omega) = 3n - 5$. The preferred approach to such high dimensional integration problems are Monte Carlo (MC) methods. In the simplest realization, one draws a (pseudo-)random ensemble of N allowed momentum configurations $\mathfrak{p}_k = \{p_1, \ldots, p_n\}_k$, i. e. accessible phase space points, which are uniformly distributed over Ω. Then the integral value is approximated by the mean value of f over the ensemble [137],

$$I[f] = \int_\Omega \mathrm{d}p\, f(p) \approx V\langle f\rangle = \frac{V}{N}\sum_{k=1}^{N} f(\mathfrak{p}_k)\ , \tag{3.4}$$

where V is the volume of Ω. In addition, if $f(p)$ can be properly normalized and interpreted as a probability density (as should be the case for any well behaved matrix element function, cf. Sec. 4.1 for problems arising from infrared singularities at tree level), each event $\mathfrak{p}_k$ is assigned a statistical weight $f(\mathfrak{p}_k)$: we have a set of *weighted events*

$$\mathcal{W} = \big\{\big(\mathfrak{p}_1, f(\mathfrak{p}_1)\big), \ldots, \big(\mathfrak{p}_N, f(\mathfrak{p}_N)\big)\big\}\ . \tag{3.5}$$

Unweighting the set can be done by a simple procedure; just draw N numbers $z_k \in [0, \max_\Omega f]$ and keep only the events satisfying $z_k \leq f(\mathfrak{p}_k)$. This gives a set of *unweighted events*

$$\mathcal{U} = \{\mathfrak{p}_k | z_k \leq f(\mathfrak{p}_k)\} = \{\mathfrak{p}_{k_1}, \ldots, \mathfrak{p}_{k_n}\} \tag{3.6}$$

containing n phase space points which have survived the procedure. For phenomenological collider studies, $\mathcal{U}$ is usually favored over $\mathcal{W}$, because it represents an event sample whose distribution over Ω follows the actual matrix element, thus mimicking the phase space population as expected from a real experiment.

Now that the nomenclature is set, let us come to the limitations of this simple procedure introduced so far: pragmatically, the aim of any MC integration is to obtain a precise estimate for $I[f]$, and to efficiently generate unweighted events. However, both the uncertainty of the integration estimate, Eq. (3.4), estimated by the square root of the variance

$$\Delta[f] = \frac{1}{N-1}\left(\langle f^2\rangle - \langle f\rangle^2\right) \tag{3.7}$$

as well as the the efficiency of the unweighting procedure, i. e. the ratio of event numbers n/N inside the sets $\mathcal{U}$ resp. $\mathcal{W}$, heavily relies on the question whether $f(p)$ is well behaved in Ω. In general, this is obviously not the case, because matrix elements usually have a complicated resonance structure from the propagators, dominated by

large contributions in very small corners of Ω, whereas huge parts of the remaining phase space are almost negligible, while additional (user defined) phase space cuts multiply further Θ functions to the integrand. Clearly, this calls for an optimization of the procedure, where from the variance and unweighting efficiency the road map is evident: find a function $g(p)$ over Ω such that the MC integrand $f \to f/g$ becomes well behaved, with an error estimate now given by $\Delta[f/g]$. However, as

$$I[f] = \int_\Omega \mathrm{d}p\, g(p)\, \frac{f}{g}(p)\ , \tag{3.8}$$

the drawing of random phase space points $\mathfrak{p}_k$, now distributed according to $g(p)\mathrm{d}p$, must also remain economic. Optimization of $\Delta[f/g]$ vs. fast generation of $\mathfrak{p}_k$ pose conflicting goals to g, so again pragmatic solutions have to be applied.

The standard tool for the numerical adaption of integral measures for MC integration over the past decades has been VEGAS [138], which uses a factorized ansatz for g. However, the factorization property obviously depends on the coordinates, and matrix elements in collider applications often comprise sums of distinct resonance structures which generally factorize in *different* coordinates [139], so that the overall function does not factorize any more in just a single map of Ω. WHIZARD employs the multi channel sampling tool VAMP [139], which builds on VEGAS but separates the full amplitude into several integration channels with individually optimized phase space maps ϕ_k. This requires some heuristics, because accounting for all propagator structures in f would reintroduce the whole diagram multiplicity at the integration level [56]: some restricted knowledge about the physics going into f is used by WHIZARD to guess the most important kinematic channels such as hard s channels ("signal-like" diagrams) or massless branchings, and identify equivalences from crossing. Thus the full multi-dimensional phase space mapping function g is parametrized as

$$g(x) = \sum_{k=1}^{m} \alpha_k \left(g_k \circ \phi_k\right)(x) \tag{3.9}$$

with m integration channels of different weights α_k, and corresponding grid functions g_k obeying a factorized ansatz within their respective map ϕ_k. In the adaption phase, these g_k are adapted individually by VEGAS in each channel, while the α_k are adapted by VAMP to reduce the overall variance $\Delta[f/g]$.

In summary, an ordinary WHIZARD run usually consists of three steps: an adaption step to find an optimal g for a given f as described above, followed by the actual integration step, where the phase space is sampled according to g with high statistics in order to further reduce the error of $I[f]$ ($\sim 1/\sqrt{N}$). Finally, in the event generation step $I[f]$ (i. e. the total cross section, multiplied by cut efficiencies) and g are used to generate unweighted event samples corresponding to a given integrated luminosity. This is the basis for Ch. 4, which is concerned with technical issues of event generation as well as the whole subsequent simulation chain, from parton level events to detector level samples. The remainder of this chapter addresses the actual WHIZARD implementation of new physics in the form of anomalous top couplings as described in Ch. 2.

3.2. Implementation of Anomalous Top Couplings

As described in the previous section, all the physics up to the finished matrix element is handled by O'Mega. Basically, O'Mega is an O'Caml program which takes the particular physics model in the form of Feynman rules as input, then performs the algorithms described in Sec. 3.1.1 to find all 1POWs and construct a DAG representing the amplitude of the requested process, and finally translates it to a self-contained Fortran program. Hence, the implementation of new coupling structures into the Whizard package mainly requires to edit O'Mega. In principle, one has to

- provide a user interface which takes values for the model parameters as external input and initializes them as Fortran variables/functions;
- convey an O'Caml model file containing the new Feynman rules;
- extend the Fortran library whenever necessary to provide Fortran vertex functions for any Lorentz structures contained in the Feynman rules.

As this sounds a little tedious, one should shortly mention the meantime progress in simplifying the implementation of new models into the Whizard package. Indeed, there exists a tested interface [140] to FeynRules [141], which only needs to know the model Lagrangian for input to automatically generate the required O'Mega code. However, to date the bottleneck still is the Fortran library, where all Lorentz structures must be available as hardcoded functions, so that the interface only works with already implemented "standard" structures. Although from version 2.2 onwards general Lorentz structures will be supported, as this is still ongoing development the present implementation must follow the classic way. Omitting several minor changes to the infrastructure, the points stated above are realized as follows: for the anomalous top couplings, we provide a new model called `SM_top_anom` and steered by the user input file `SM_top_anom.mdl`. However, mainly to simplify maintenance, the Feynman rules themselves are not defined in a separate model but as an extension to the SM, inside the corresponding O'Caml file `modellib_SM.ml` (to be switched on/off by a model flag). Finally, new vertex functions were added to the code library `omegalib.nw` to account for the Lorentz tensor structure $\sigma^{\mu\nu}$. The various kinds of anomalous interactions are now addressed in more detail, sorted according to the structural differences of their implementation, while a complete list of their names inside the model can be found in appendix D.1.

3.2.1. Trilinear Interactions

Scalar and Vector Couplings

The simplest structures to implement are the anomalous trilinear (pseudo-)scalar tth couplings $Y_t^{V,A}$, Eq. (2.40), and vector couplings $\propto \gamma^\mu$, namely the CC tbW couplings $V_{L,R}$, Eq. (2.24a), and the NC ttZ couplings $X_{tt}^{L,R}$, Eq. (2.29a), because the Lorentz structures are no different from those appearing in the SM Lagrangian. It only

remains to state the Feynman rule of the vertex and fudge it with a corresponding numerical factor. In `modellib_SM.ml`, the tbW vertex simply looks like

```
((M (D (-3)), G Wm, M (U 3)), FBF (1, Psibar, VLR, Psi), G_VLR_btW);
((M (U (-3)), G Wp, M (D 3)), FBF (1, Psibar, VLR, Psi), G_VLR_tbW)
```

which should be read as

$$\Big(\big(\text{flavors: } \bar{b}W^- t\big)\,, \big(\text{Lorentz: } \overline{\Psi}\gamma^\mu (V_L P_L + V_R P_R)\Psi\big)\,, \text{couplings: } (V_L, V_R)\Big) + \text{h.c.}$$

The keyword `VLR` (`SP` for (pseudo-)scalar in the tth case) in the code tells O'Mega to take the correct set of $2 \to 1$ wave function fusions from the Fortran library, where the actual fusion direction depends on the architecture of the DAG (cf. the next paragraph and appendix D.2). The bookkeeping of the number of vertices and propagators with corresponding factors of i in the amplitude is handled internally by O'Mega, so that most of the time the Feynman rule can be read off directly from the respective Lagrangian term (up to multiplicities from identical particles), with any explicit i factors in the Lagrangian to be explicitly carried over to the Feynman rule.

Form Factors

In fact, although the Lagrangian terms themselves do not require it, the vector-like vertices were actually extended to make the momentum transfer q^2 of the fermion line available to the coupling module (by replacing the keywords `VLR` $\to$ `VLRM` resp. `SP` $\to$ `SPM`). This is because the model supports the option to replace simple numerical coupling values g by form factors, i. e. promote them to functions $g(q^2)$, employing heuristic functional dependences, among others a dipole-like dependence $g(q^2) \sim (1+ q^2/\Lambda^2)^{-2}$. Note that the actual fusion functions to be called are not affected, we just make the code generator insert the value of q^2 as an argument of the couplings, which are themselves arguments of the fusion functions. Of course, this functionality is also available for the tensor couplings in the next section, where the fusion functions need the full momentum transfer vector anyway.

Tensor Couplings

In addition to the scalar and vector structures, there are the anomalous trilinear tensor couplings $\propto \sigma^{\mu\nu} q_\nu$, namely the CC ones $g_{L,R}$, Eq. (2.24b), the NC ones $d^Z_{V,A}$, Eq. (2.29b), and $d^\gamma_{V,A}$, Eq. (2.35), as well as the ttg couplings $d^g_{V,A}$. In principle, the implementation proceeds as before, but this time the required vertex fusions have to be provided by hand in the Fortran library. Typically, a set of vertex fusions consists of three separate functions corresponding to the three different possibilities to take two wave functions at the vertex as arguments and fuse them into a third one given as result ("fusion directions"). All of them are necessary because the actual fusion direction depends on the way the DAG was constructed by O'Mega.

The fusions themselves are implemented as Fortran functions by simply hard-coding the spinor matrix multiplications of the incoming wave functions, and returning an outgoing one in the correct representation. To be more general, this was done

for a generic antisymmetric Lorentz tensor $T^{\mu\nu}$, providing the three fusion directions

$$\overline{\Psi}\Gamma^{\mu\nu}(\vec{g})\Psi \to T^{\mu\nu} \,, \tag{3.10a}$$
$$T^{\mu\nu}\Gamma_{\mu\nu}(\vec{g})\Psi \to \Psi \,, \tag{3.10b}$$
$$\overline{\Psi}T^{\mu\nu}\Gamma_{\mu\nu}(\vec{g}) \to \overline{\Psi} \,, \tag{3.10c}$$

where $\Gamma^{\mu\nu}(\vec{g})$ is $\sigma^{\mu\nu}$ times a superposition of $\mathbf{1}$ and γ_5 in spinor space, controlled by the coupling values $\vec{g}$. In the case of our trilinear top–gauge boson couplings, the result of fusion (3.10a) is contracted with the momentum transfer $\mathrm{i}(p-p')_\nu$ afterwards to give the outgoing vector boson wave function A^μ, while in the directions (3.10b)–(3.10c) T is constructed from an incoming vector wave function with momentum q as $T = \frac{\mathrm{i}}{2} A \wedge q$, cf. appendix D.2 for more details including actual code chunks implementing Eq. (3.10). Finally, the new vertex structure is made available at the Feynman rule level, depending on the choice of the parametrization of Γ, by the keywords `TVAM` (vector–axial), `TLRM` ((left–right-handed) and `TRLM` (required because the vertex mixes chiralities, just like a mass term).

3.2.2. Quartic Interactions

As argued in Ch. 2, there are many reasons why quartic interactions must be included in a gauge-invariant effective operator approach to anomalous trilinear top couplings: for one, there are quartic top–gauge interactions required to fix the ward identities of the amplitude, but there are also four-fermion interactions which cannot reasonably be separated from the trilinear ones at the amplitude level. Now turning to their actual implementation, note that despite the simplified version of the algorithm that was presented in Sec. 3.1.1 and only considered trilinear vertices, O'Mega is in principle able to handle quartic vertices. However, once the lines get dressed with quantum numbers and specific representation indices, it is generally not clear any more which of the lines should be combined at a quartic vertex. Therefore, since the resulting DAG only contains topological information on all possible momentum flows in the amplitude, as a means of bookkeeping it is convenient to represent the quartic interactions by 1POWs which are built from two trilinear fusions, i. e. introduce an auxiliary non-propagating field Π to make the replacement

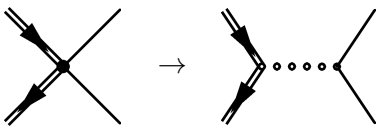

(3.11)

where any of the external lines may be off-shell. The double fermion line indicates the heavy flavor, while the plain line may be any pair of fields that couple to the heavy fermion pair, in our case either two gauge bosons or two other fermions. Evidently, this whole procedure leaves the momentum combinatorics in the amplitude unaffected. The Π just has to come in the right representation of the Lorentz and gauge groups to mediate the correct structure of the original quartic interaction.

Since O'Mega inserts an i for each vertex and each propagator, the couplings are simply related as

$$g_4 = \mathrm{i}^2 g_3 D g_3' = -g_3 g_3' \,, \tag{3.12}$$

noting that the constant inserted for the propagator is just $D = 1$.

One could now try to write down a field theory in terms of a Lagrangian containing the Π field to derive the correct Feynman rules generating diagrams like Eq. (3.11). Conversely, we can just guess them to see what is the problem:

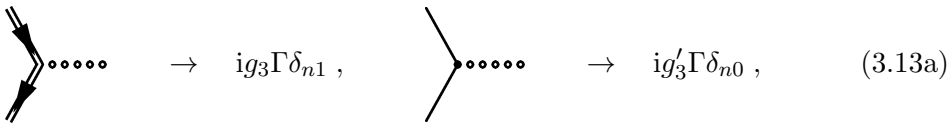

(3.13a)

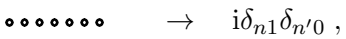

(3.13b)

where Γ encodes the group structure of the vertex, i. e. it carries Lorentz, spinor or gauge indices in any given representation imposed by the original contact term. On the other hand, n is a new quantum number adopting two different values, so we have just made it a boolean, $n = 1, 0$. The necessity to introduce n is clear from the asymmetric nature of the contact terms: we must couple the heavy fermion line to its counterpart, while forbidding any symmetric diagram coupling the heavy line (or the counterpart) to itself. In terms of the Π field, this is a non-local property requiring a propagator which is non-diagonal in n, as written down in Eq. (3.13b). Suppressing all indices except for n, this would correspond to a Lagrangian

$$\mathcal{L}_\Pi = \sum_n g_n J_n \Pi_n + \Pi_1^\dagger \Pi_0 + \text{h.c.} \tag{3.14}$$

with $J_1 = \bar{q}_3 \Gamma q_3$ and $g_n = g_3^{(\prime)}$, where Γ and the field bilinear J_0 depend on the specific contact interaction to be generated. The standard (and O'Mega) procedure is to diagonalize the Lagrangian in the bilinear terms to find the propagating eigenstates. This can be done here as well, leading to

$$\mathcal{L}_\Pi = \frac{g_1}{\sqrt{2}} J_1 (\Pi_+ + \Pi_-) + \frac{g_0}{\sqrt{2}} J_0 (\Pi_+ - \Pi_-) + \Pi_+^\dagger \Pi_+ - \Pi_-^\dagger \Pi_- + \text{h.c.} \tag{3.15}$$

with $\Pi_\pm = \frac{1}{\sqrt{2}}(\Pi_1 \pm \Pi_0)$. Eq. (3.15) produces Feynman rules generating $J_1 J_1$ and $J_0 J_0$ interactions, respectively, but of course by construction the corresponding diagrams cancel,

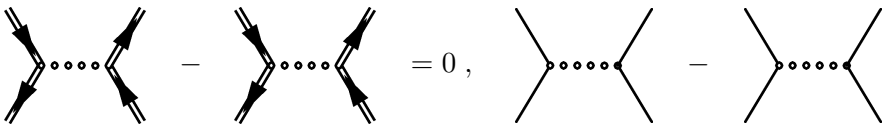

(3.16)

while the desired contact interaction

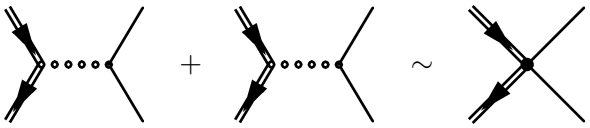

(3.17)

is correctly produced. Yet such an implementation would entail a heap of nontrivial zeros added to amplitudes which actually have nothing to do with anomalous top couplings at all, apart from doubling the number of Feynman rules to be implemented in the physical basis of $J_{0,1}$.

However, there is a neat trick to implement the original approach of Eq. (3.13) with just three Feynman rules and one non-diagonal propagator for each contact interaction: note that the Π only occurs internally in a diagram, never as an external leg, so O'Mega needs to know its hermitian conjugate only to construct the internal propagator. Hence, a conjugation rule $(\Pi_n)^\dagger = (\Pi^\dagger)_{!n}$ forces the propagator $D \sim \langle \Pi_n (\Pi_n)^\dagger \rangle$ off-diagonal, and together with the two vertices (3.13a) exactly produces the desired contact interactions; this is the procedure pursued in our model. In terms of O'Mega code, one has to define the new field Π, called `Aux_top` in `modellib_SM.ml`, and assign to it a set of quantum numbers:

```
type other = ... | Aux_top of int*int*int*bool*f_aux_top
                          (*i lorentz*color*charge*top-side*flavor *)
```

where *lorentz* labels the possible Lorentz representations. For our purposes, we require at least an antisymmetric tensor for the top–gauge interactions, plus a vector and a scalar for the various four-fermion interactions of Eqs. (2.43) and (2.45). Of the other quantum numbers of `Aux_top`, *color* switches between a singlet and an adjoint representation of $\mathbf{SU}(3)_{\mathrm{QCD}}$, *charge* is the ordinary electromagnetic charge, and *top-side* is the new quantum number n. Finally, *flavor* just labels the various contact interactions in a legible way, cf. appendix D.3 for more implementation details, including example vertex statements for the *tbWA* interaction and the fixing of top–gauge coefficients according to gauge invariance. Concerning the quartic fermion terms, at the moment only the CC interactions introduced in Sec. 2.3.1 and studied in Sec. 5.2 are available at the user level, in order to keep the number of parameters in `SM_top_anom.mdl` small, cf. Eq. (D.2) for naming conventions. (There are many different NC structures, cf. 2.3.2, so any study would first have to restrict them according to some phenomenological reasoning anyway, but in principle all of them are implemented and could be provided at the user interface.)

3.3. Validation

The last section of this chapter is devoted to the validation of the Whizard implementation. It should cover various critical aspects, including

- a test of the algebraic structure of the new tensor vertex fusions,
- overall coupling signs and normalizations,

- relative coupling signs and consistency between trilinear and quartic top–gauge interactions,
- correct cross sections and differential distributions.

In the following, we present a series of validation checks that have been performed, and comment on which of the above points could be verified by the various methods.

Gordon Identity

The spinor structure of the tensor vertex $\propto \sigma^{\mu\nu}$ obeys an algebraic identity known as the *Gordon identity*, which reads

$$\overline{\psi}(p')\gamma^\mu\psi(p) = \overline{\psi}\left(\frac{(p'+p)^\mu}{2m} + \frac{\mathrm{i}\sigma^{\mu\nu}(p'-p)_\nu}{2m}\right)\psi(p) \tag{3.18}$$

with a Dirac spinor ψ of mass m. Since the spinor product has been hardcoded in the respective FORTRAN fusion functions, cf. appendix D.2, one can perform numerical tests to verify the correct implementation of the various fusion directions. To that end, contract Eq. (3.18) with the spinor momentum p, use the Dirac equation and optionally insert a γ_5 matrix to obtain two scalar identities,

$$p_\mu\left(\overline{\psi}(p')\mathrm{i}\sigma^{\mu\nu}q_\nu\psi(p)\right) - \left(p\cdot q - m^2\right)\overline{\psi}(p')\psi(p) = 0 \tag{3.19a}$$

$$p_\mu\left(\overline{\psi}(p')\mathrm{i}\sigma^{\mu\nu}q_\nu\gamma_5\psi(p)\right) - \left(p\cdot q + m^2\right)\overline{\psi}(p')\gamma_5\psi(p) = 0 \tag{3.19b}$$

with $q = p' - p$, which can easily be tested at the FORTRAN function level: just generate on-shell momenta p and p' of given m, compute corresponding Dirac spinors u, v of any fixed helicity, and see if the left-hand side of Eqs. (3.19) vanishes up to numerical stability, for each of the fusion directions (3.10).

Ward Identities

It is an inherent property of gauge theories that the gauge bosons couple to conserved Noether currents which come with the respective gauge symmetry. The momentum space version of this statement, well-known as *Ward identity*, is that an external gauge boson state decomposes into physical polarizations perpendicular to its momentum, while any contribution parallel to the momentum must vanish by current conservation. In O'MEGA, Ward identities of amplitudes containing external gauge bosons can be neatly tested on the basis of the 1POWs on which the amplitude is built up. As explained in Sec. 3.1.1, the 1POWs already represent "almost physical" objects with all but one external leg removed. If the remaining off-shell leg corresponds to a gauge boson, the dot product with the respective momentum must evaluate to zero, or to the gauge boson mass in spontaneously broken gauge theories [133].

In the context of anomalous top interactions, such Ward identities represent powerful checks of the implementation, as well as relative signs of various trilinear and quartic couplings in the non-Abelian case. For simplicity, consider the gluon pair

production amplitude $t\bar{t} \to gg$, because the $\mathbf{SU}(3)_{\text{QCD}}$ gauge symmetry is unbroken. In the SM case it is straightforward to verify the Ward identity (following e. g. [63], Ch. 16.2): there are three contributing diagrams (namely those of Fig. 2.4, read from right to left),

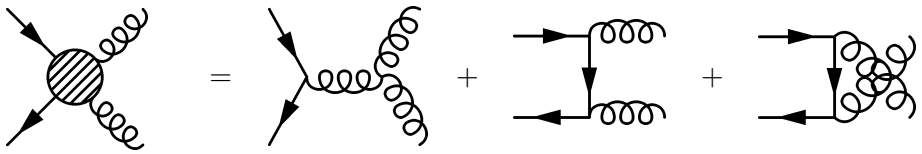

(3.20)

The t plus u channels contracted with $k_{2\nu}$ and a physical polarization $\varepsilon_\mu(k_1) \equiv \varepsilon_{1\mu}$ obeying $\varepsilon_1 \cdot k_1 = 0$ give

$$\begin{aligned} \mathrm{i}(\mathcal{M}_t + \mathcal{M}_u)^{\mu\nu}\varepsilon_{1\mu}k_{2\nu} = \bar{v}(p_+)\Big\{ &\left(\mathrm{i}g_s \not{\varepsilon}_1 t^a\right)\frac{\mathrm{i}}{\not{p} - \not{k}_2 - m_t}\left(\mathrm{i}g_s \not{k}_2 t^b\right) \\ &+ \left(\mathrm{i}g_s \not{k}_2 t^b\right)\frac{\mathrm{i}}{\not{k}_2 - \not{p}_+ - m_t}\left(\mathrm{i}g_s \not{\varepsilon}_1 t^a\right)\Big\} u(p) \\ = -g_s^2\, \bar{v}(p_+)\left\{-\mathrm{i}\not{\varepsilon}_1 [t^a, t^b]\right\} u(p) \end{aligned} \tag{3.21}$$

with normalized Gell-Man matrices $t^a \equiv \lambda^a/2$, where the on-shell Dirac equations have been employed to add a zero and cancel the propagators in the first line. In the Abelian case the commutator vanishes, and there is no s channel diagram, but in the non-Abelian case the s channel reads

$$\begin{aligned} \mathrm{i}\mathcal{M}_s^{\mu\nu}\varepsilon_{1\mu}k_{2\nu} &= \mathrm{i}g_s \bar{v}(p_+)\gamma_\rho t^c u(p)\frac{-\mathrm{i}}{q^2} \times g_s f^{abc}\left(g^{\rho\mu}q^2 - q^\rho q^\mu\right)\varepsilon_{1\mu} \\ &= g_s^2 f^{abc}\, \bar{v}(p_+)\not{\varepsilon}_1 t^c u(p)\,, \end{aligned} \tag{3.22}$$

where $\bar{v}\,\not{q}\,u = 0$. By virtue of the generator algebra of the gauge group, Eq. (A.5), the contributions (3.21) and (3.22) exactly cancel in the non-Abelian case.

Now turning to anomalous QCD interactions, recall the effective interaction Lagrangian including the $d = 6$ operator $O_{uG\phi}$ (2.4d) to derive the Feynman rules from scratch[2]:

$$\begin{aligned} \mathcal{L}_{\text{QCD}} =& g_s \bar{t}\gamma^\mu \frac{\lambda^a}{2} t\, G_\mu^a + g_s \bar{t}\frac{\lambda^a}{2}\sigma^{\mu\nu}\tilde{C}\, t\left(\partial_\nu G_\mu^a - \frac{1}{2}g_s f^{abc} G_\mu^b G_\nu^c\right) \\ &\text{with } \tilde{C} \equiv -\frac{2\sqrt{2}v}{g_s \Lambda^2}\left(\mathrm{Re}\, C_{uG\phi} + \mathrm{i}\gamma_5 \mathrm{Im}\, C_{uG\phi}\right). \end{aligned} \tag{3.23}$$

From Eq. (3.23) we find the Feynman rules

$$\to \quad \mathrm{i}g_s(\gamma^\mu + \Gamma^\mu(k))t^a \qquad \text{with } \Gamma^\mu(k) \equiv \mathrm{i}\sigma^{\mu\nu}k_\nu\tilde{C}\ , \tag{3.24a}$$

$$\to \quad -\mathrm{i}g_s^2 f^{abc}t^c\,\sigma^{\mu\nu}\tilde{C}\ , \tag{3.24b}$$

where the derivative was replaced by the momentum transfer away from the fermion line, $\partial_\mu \to \mathrm{i}k_\mu$, in accord with the O'Mega implementation, while in the contact interaction the factor $1/2$ was cancelled by the gauge boson multiplicity. We now have to add the contact diagram to the SM diagrams (3.20) and replace the trilinear vertex by (3.24a) wherever possible, but generally $\Gamma(k)\cdot k = 0$ due to the asymmetry. All in all, the new diagrams surviving the contraction with $k_{2\nu}$ are

$\delta\mathcal{M} =$ 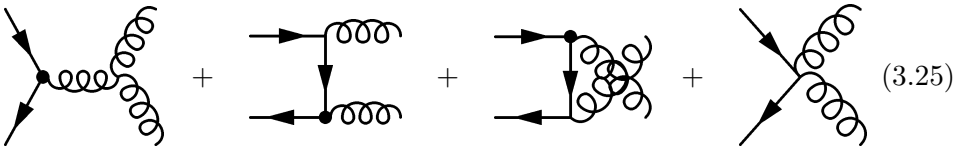 (3.25)

with replacements $\gamma^\mu \to \Gamma^\mu$ indicated by a dot. The computation of the first three diagrams containing a Γ^μ proceeds exactly as in Eqs. (3.21) and (3.22), but this time their sum does not entirely cancel because of the dependence on the gauge boson momentum. The leftover is

$$\begin{aligned}\mathrm{i}\delta(\mathcal{M}_s+\mathcal{M}_t+\mathcal{M}_u)^{\mu\nu}\epsilon_{1\mu}k_{2\nu} &= g_s^2 f^{abc}\,\bar{v}(p_+)\big(-\Gamma(k_1)+\Gamma(-q)\big)^\mu t^c u(p)\epsilon_{1\mu}\\ &= g_s^2 f^{abc}\,\bar{v}(p_+)\big(\Gamma(k_2)\cdot\varepsilon_1\big)t^c u(p)\ ,\end{aligned} \tag{3.26}$$

but there still is the contact diagram. Using the Feynman rule (3.24b), one finds

$$\mathrm{i}\mathcal{M}_\times^{\mu\nu}\epsilon_{1\mu}k_{2\nu} = -\mathrm{i}g_s^2 f^{abc}\,\bar{v}(p_+)\sigma^{\mu\nu}\tilde{C}t^c u(p)\varepsilon_{1\mu}k_{2\nu}\ , \tag{3.27}$$

which cancels the term (3.26).

Concerning the actual implementation, conventions were already adapted to the O'Mega ones in this paragraph, but there are some remaining remarks. First note that the contact interaction is internally invoked by a constant auxiliary field exchanged between two trilinear vertices with couplings g_1 and g_0, which produces an extra i^2 (cf. Sec. 3.2.2). Note further that O'Mega handles color in the color flow representation [56, 142, 143], which eliminates adjoint indices in favor of fundamental $3\otimes\overline{3}$ indices, cf. appendix D.3, so internally $f^{abc}G^bG^c \to -\frac{\mathrm{i}}{2}G\wedge G$. While the factor $1/2$ is generic to the color flow basis and hence already absorbed into g_s^2, a $(-\mathrm{i})$ must

[2] Note that the signs are consistent with the sign convention used in appendix A and in O'Mega, while section 2 follows the other convention with a flipped sign of the gauge coupling in the definition of the covariant derivative and the field strength, consistent with existing literature on anomalous top couplings. However, as will be argued below, this section is concerned only with *relative* coupling signs, while absolute signs entering the normalization are fixed in O'Mega by comparison to the SM couplings.

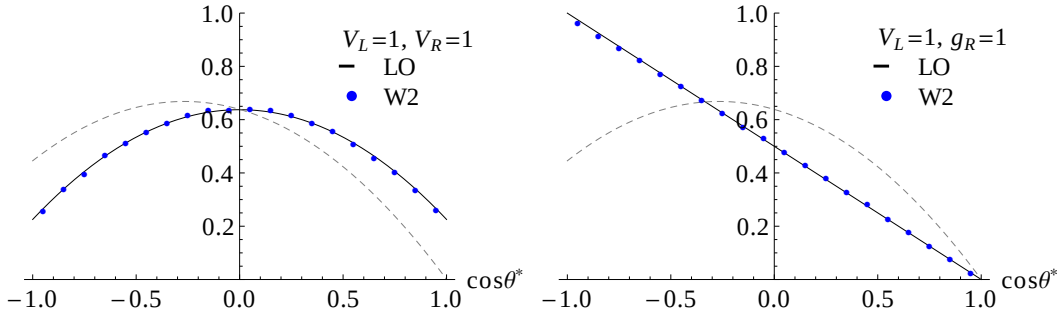

Figure 3.1.: Comparison of the normalized differential decay width, Eq. (2.53), from WHIZARD (version 2, "W2") and an analytical LO calculation, for different coupling combinations (SM indicated in dashed grey for reference).

be reintroduced by hand in our particular contact vertex. In summary, the vertex prefactor is partitioned onto the internal trilinear couplings as

$$g_1 = -g_s\tilde{C}\ , \qquad g_0 = \mathrm{i}g_s\ , \tag{3.28}$$

where $\tilde{C}$ also controls the trilinear anomalous couplings, cf. Eq. (3.24a). Thus, the Ward identity tests the correct fixing of the quartic coupling relative to the trilinear one, irrespective of the overall normalization convention. The procedure can be extended in an obvious way to the anomalous electroweak sector. For instance, the photon polarization in the amplitude $t\bar{b} \to W^+A$ fulfills an exact Ward identity due to unbroken QED, which fixes the quartic $tbWA$ prefactor, cf. Eq. (D.4). Once this is known, the prefactors for the other terms $tbWZ$, $ttWW$ and $bbWW$ are trivially obtained by the rotation prescription of the gauge field components into the physical basis, cf. Eqs. (1.22) and e. g. (2.21).

Top Decay

As described in Sec. 2.5.2, in the MFV scheme the fact that the top decay is dominated by the CC channel $t \to bW$ remains unaffected by BSM physics. In this channel, the total decay width decomposes into partial widths which correspond to the various possible polarizations of the W boson, cf. Eq. (2.53), which are sensitive to anomalous contributions to the tbW vertex (2.24). Hence the differential decay width with respect to the angle θ^* defined in Sec. 2.5.2 represents a good handle to validate the top decay width in our model as a function of the anomalous couplings. The normalized differential width, Eq. (2.53) as a function of $\vec{g} = \{V_L, V_R, g_L, g_R\}$, can straightforwardly be plotted with the WHIZARD package and compared to the analytical LO results given in [94]. Fig. 3.1 illustrates some representative histograms for specific parameter points, underlining the excellent agreement of the generated event distributions with the LO expectation. The same agreement is obtained in collision processes $pp \to t\bar{t} \to b\bar{b}\ell\bar{\ell}\nu\bar{\nu}$, integrating over full resonant amplitudes without

sample				A_ℓ		A_b		A_ν	
V_L	V_R	g_L	g_R	LO	W2	LO	W2	LO	W2
1	0	0	0	0.500	0.500	-0.198	-0.199	-0.167	-0.164
1	1	0	0	0.329	0.326	0.000	0.000	-0.329	-0.327
1	0	1	0	0.502	0.500	-0.324	-0.322	-0.195	-0.194
1	0	0	1	-0.242	-0.232	0.166	0.161	0.055	0.056
0	1	1	0	-0.055	-0.057	-0.166	-0.159	0.242	0.230
0	1	0	1	0.195	0.195	0.324	0.322	-0.502	-0.501
0	0	1	1	0.353	0.355	0.000	0.000	-0.353	-0.354

Table 3.1.: Comparison of W2 with analytical LO results for spin symmetries A_X ($X = \ell, \nu, b$), at different coupling values $\vec{g}$ (W2 statistical uncertainties $\lesssim 0.004$).

cuts. This is a nontrivial result, because depending on the process O'Mega invokes different fusion functions of the new vertices in different amplitudes, so the internal consistency of fusions and sign conventions is tested that way.

Further angular observables θ_X ($X = \ell, \nu, b$) were introduced for the top decay products in Sec. 2.5.2, cf. Eq. (2.56), where the respective asymmetries A_X (2.58) are sensitive to the production of top polarization times "analyzing power" $\alpha_X(\vec{g})$ of the decay product. While it was argued that with the knowledge of $\vec{g}$ one can measure the top polarization, the A_X conversely represent another validation of the implementation of $\vec{g}$ once tops are produced on-shell in a given polarization direction. Again, obtaining numerical values with Whizard and comparing them to analytical LO results [101] is straightforward, and results in very good overall agreement as summarized in Tab. 3.1.[3]

Single Top $2 \to 2$ Cross Sections

Apart from the top decay, single top production at hadron colliders is also dominated by electroweak CC interactions. As already mentioned in Sec. 2.5.4 and explained in more detail later on in Sec. 5.1.1, in the approximation of on-shell top production the cross section is a quadratic function of the CC couplings $\vec{g}$. Although the phenomenological validity of this approximation is one of the main subjects of Chapter 5, the approximation itself is well-suited to perform further validation tests of the implementation. The numerical coefficients of the squared terms $\sim g_i^2$ obtained with Whizard are sensitive to the absolute normalization of the couplings; once these are fixed with respect to the SM strength $\sim V_L^2$, the interference terms $\sim g_i g_j$ test the relative signs of the couplings, where the SM–NP interferences $\sim V_L g_i$ are particularly important to check the sign convention of the anomalous couplings against the SM implementation.

[3] One could see a slight deviation in the numbers for $V_L g_R$ resp. $V_R g_L$, but ref. [101] states that $\mathcal{O}(1\,\%)$ and smaller terms were omitted in the analytical expressions, and these coupling combinations indeed show the largest interference terms of all, cf. Fig. 3.2 and Sec. 5.1.2.

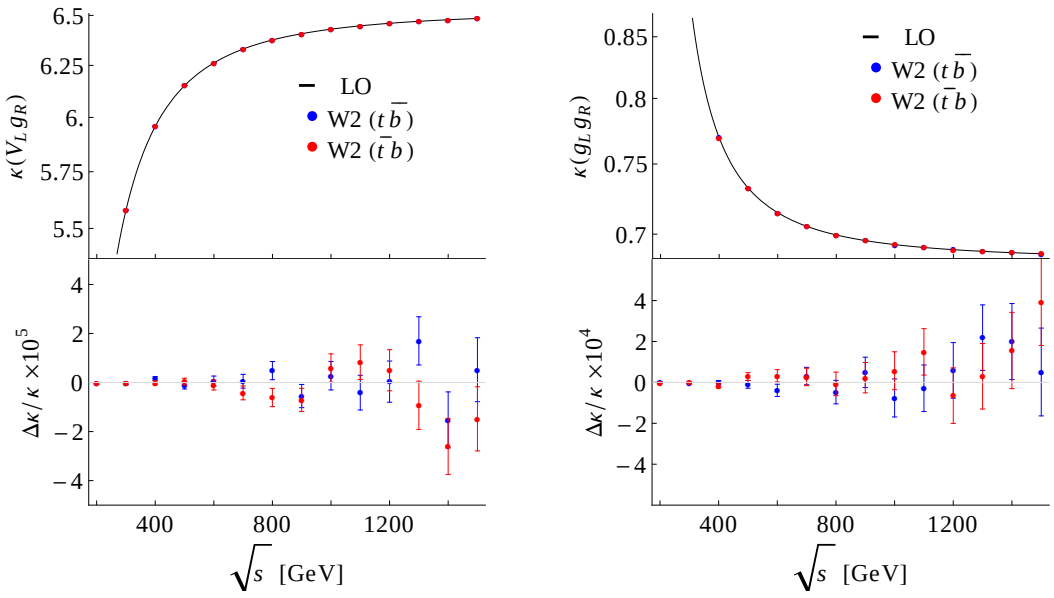

Figure 3.2.: Comparison of interference κ coefficients $\sim V_L g_R$ (left) and $\sim g_L g_R$ (right) for on-shell s channel production, cf. Sec. 5.1.1, as a function of $\sqrt{\hat{s}}$ obtained from W2 and an analytical LO calculation: absolute values (top) and relative differences (bottom) including MC errors.

Switching off the initial state proton pdfs for the moment, the cross section for the process $u\bar{d} \to t\bar{b}$ can be easily computed analytically at LO, as a function of the partonic $\sqrt{\hat{s}}$ and the scattering angle $\cos\theta$. As illustrated in Fig. 3.2 for two examples, the WHIZARD and analytical results for the κ coefficients (essentially the numerical coefficients of the quadratic approach normalized to the SM strength, see Sec. 5.1.1 for a detailed introduction) agree in absolute size and relative sign, for all possible coupling combinations. In addition, numerical values for all κ coefficients in all production channels are available in the literature in an LHC setup with pdfs at $\sqrt{s} = 14\,\text{TeV}$ [79]. It was verified that WHIZARD produces the same values up to the MC uncertainty once an identical parameter and pdf setup as in [79] is employed.

4. Single Top Event Generation and Simulation

While Ch. 3 was concerned with the description of the basic working principles of the leading order Monte Carlo event generator WHIZARD as well as the implementation of the anomalous top couplings introduced in Ch. 2, this chapter will be devoted to the actual procedure of event generation and simulation of LHC processes, mostly focusing on single top processes because they stand in the center of Ch. 5. Sec. 4.1 describes the employment of WHIZARD to integrate SM and BSM processes, and generate parton level event samples, whereas details on the further simulation chain including shower, fragmentation and detector simulation can be found in Sec. 4.2.

4.1. Parton Level

4.1.1. Process Definitions

As described in Sec. 2.5.4, there are in principle three ways to produce a single top on-shell at a hadron collider, namely s channel, t channel and associated tW production (cf. Fig. 2.6), all of which are mediated by a single CC interaction (tbW or $tbff'$ in the general BSM case). Generally, the narrow width approximation (NWA) is employed in such cases to factorize heavy intermediate states into on-shell production and subsequent decay, traditionally estimating an error of $\mathcal{O}(\Gamma_t/m_t)$, where Γ_t is the top width. However, in the case of anomalous CC couplings $\vec{g}$, production as well as decay of the top are affected by NP contributions. Of course, even if $\Gamma_t \equiv \Gamma_t(\vec{g})$ the propagator should still cancel against the width in the numerator according to NWA, irrespective of $\vec{g}$, but this reasoning relies on the assumption that the entire decay phase space is integrated over. This is obviously not the case at the LHC, where the decay products must be reconstructed by a detector of finite angular extent. Including finite detector acceptance A, the NWA argument only holds if A factorizes from the $\vec{g}$-dependent part, i. e. the influence of $\vec{g}$ on the distributions is negligible, so that a factor $A \cdot \Gamma_t(\vec{g})$ is recovered in the numerator to cancel the denominator. This is certainly a questionable simplification, so there are good reasons to go beyond on-shell production for single tops with anomalous CC couplings. In order to compare results and quantify the effects of including the full $\Gamma_t(\vec{g})$ dependence into the matrix element response in Sec. 5.1, single top final states will be modelled in three different schemes at parton level, namely

- plain on-shell top production;
- resonant matrix elements with the full top propagator;

- full matrix elements including signal and irreducible background diagrams.

Yet before giving the WHIZARD details, let us first address some general issues.

Preliminaries

Concerning the initial states, except for the s channel and CKM-suppressed transitions, all production modes need a b quark in the initial state, which is dominantly produced by a gluon splitting $g \to b\bar{b}$ at the LHC. Inside the detector, the b flavor can be tagged and separated from light jets mainly due to its long lifetime leading to displaced decay vertices, so in an inclusive experimental assessment the spectator b from the splitting is part of the signal signature, and should be modelled correctly by the MC. In a MC generator, the b flavor can be obtained either from the initial state pdf (diagram (a) in Fig. 4.1) or by including the splitting itself into the hard matrix element (diagram (b)), where in the first case the spectator b is added to the event beyond parton level by an initial state radiation (ISR) shower. The problem is that there are different kinematic regions where either of the approaches becomes problematic, so a correct description of the full p_T spectrum of the second b necessitates a consistent combination of both (the actual procedure called *matching* is described in Sec. 4.1.2 below).

Apart from the problem of matching, the inclusion of the splitting into the hard matrix element (ME) leads to another problem in the tW channel, because the process $gg \to tWb$ contains the $t\bar{t}$ resonance, which is an order of magnitude larger than the single top signal itself. Quite apart from this huge background contamination in the detector, it is highly nontrivial on the MC side to consistently disentangle the signal from this irreducible background in order to cleanly assess BSM contributions. Indeed, this is still a topic of vivid discussion in the literature (cf. e. g. [106] for a review), where some of the approaches are a veto cut on the second top resonance, or excluding $t\bar{t}$ diagrams from the amplitude, or subtracting the squared $t\bar{t}$ diagrams from the cross section, where only the veto cut procedure is gauge invariant (cf. [79] for a comparison). However, in this thesis it is one of the reasons to drop this production channel entirely from the analysis. The other one is that the detector signature is quite different from the s and t channel ones, because it contains an additional heavy resonance, which also leads to considerably more light jet activity. In conclusion, it essentially is a technical issue which complicates the study without affecting the statements of Ch. 5.

Yet even after dropping the tW channel, there remains a problem in the t channel radiation correction process $gq \to t\bar{b}q'$, because it contains not only the t channel diagrams (b, c) in Fig. 4.1 but also s channel correction diagrams (d, e). Although in principle these should be small ($\sigma_s/\sigma_t \lesssim 5\,\%$ at 14 TeV from Tab. 2.1), diagram (d) contains a massless propagator in the kinematic t channel. Labeling the initial (final) state momentum in the lab frame $p_{i(f)}$, the propagator reads

$$\frac{1}{(p_f - p_i)^2} = -\frac{1}{2p_f \cdot p_i} = -\frac{1}{2E_f E_i(1 - \cos\theta_f)}\,, \tag{4.1}$$

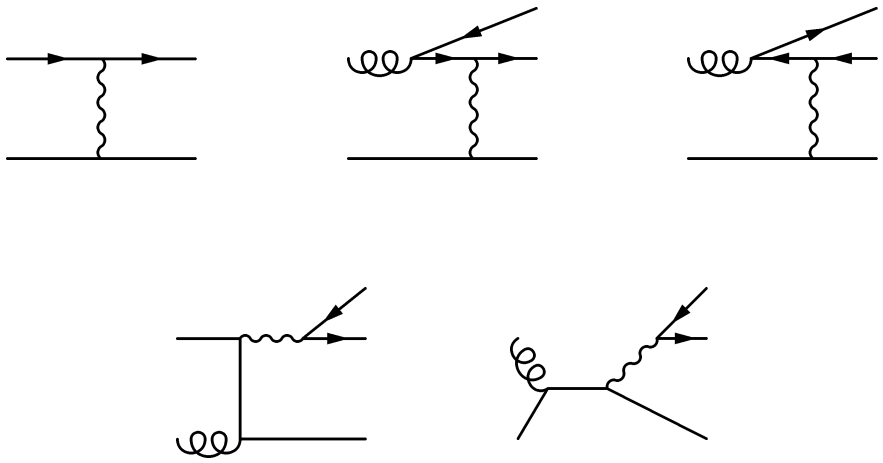

Figure 4.1.: Diagrams contributing to the tj and tbj final states (on-shell): t channel signal diagrams (a–c) and radiative correction diagrams to the s channel (d, e). The plain line may be an up–down or an anti down–up charged current among the two light quark generations.

leading to the well-known soft and collinear Coulomb singularities, namely when the energy $E_f \to 0$ or the polar angle against the beam axis $\theta_f \to 0$. In a LO program like WHIZARD they must be handled by hand, either by excluding diagram (d), which potentially violates gauge invariance, or by cutting on p_f. However, it is argued in [79] that diagrams (b) and (c) alone form a gauge invariant subset, so in the on-shell approach we will exclude diagrams (d, e) to comply with existing literature, while in the full ME approach there are detector acceptance cuts applied on the final state particles anyway, where the cut on a minimal transverse momentum p_T and maximal pseudorapidity $|\eta|$ of the light jet, cf. Eq. (4.2), automatically regularizes the divergent propagator (4.1).

WHIZARD Processes

We can now move on and define the single top processes at parton level in the three different schemes stated at the beginning of the section, starting with the on-shell scheme. In a SINDARIN file the s channel simply reads

```
process tb1 = qu, Qd => t, B
process tb2 = Qd, qu => t, B
```

with an obvious generalization to the charge-conjugated processes. `qu`, `qd`, `Qu` and `Qd` label the light (anti) quark flavors u, d, s, c (all assumed massless). The definition of two processes `tb1` and `tb2` accounts for the asymmetric initial state definition while the experiment obviously is symmetric, so results should be combined by adding cross sections and merging events into one sample[1]. The t channel is modelled

[1] WHIZARD could weed out the allowed processes itself in a symmetric initial state definition, but this would blow up the internal flavor matrix of the process with lots of zeros. The CPU cost

on-shell by merging the partonic processes $bq \to tq'$ and $gq \to t\bar{b}q'$,

```
process tj1  = b, qu:Qd => t, qd:Qu
process tbj1 = g, qu:Qd => t, qd:Qu, B   { $restrictions = "2+4~" }
```

with swapped initial states for `tj2` and `tbj2`, and conjugated processes as before in the s channel. The `$restrictions` statement enforces the light quarks to be fused into a common vertex, thus implementing the exclusion of diagrams (d, e) of Fig. 4.1. Note that a naive merging of the processes `tj` and `tbj` is only valid if the implemented ME matching[2] (explained below in Sec. 4.1.2) is enabled by the beam switch `?lhapdf_hoppet_b_matching`. This works with any LHAPDF set of choice, the default being CTEQ6L [144] in this thesis (cf. appendix C for an overview of the entire default setup employed with WHIZARD).

Moving on to the resonant and full ME schemes is straightforward from the on-shell process definitions above: just replace the `t` by its decay products,

```
process ... = ... => L, n, b, ...
```

with lepton (anti) flavors of the first two generations stacked into the labels `L` and `n` (resp. `l` and `N` for the conjugated processes), where we exclusively consider the leptonic decay channel to have a clean final state signature in the detector. Once the top decays inside the hard ME, the process definitions are only consistent when Γ_t is properly computed as a function of the anomalous couplings at each parameter point $\vec{g}$. This is done by adding an additional `process` for the top decay into all allowed products (but setting $V_{\text{CKM}} \equiv \mathbf{1}$), integrating it and assigning the result to the respective model parameter `wtop`, thus overriding (C.1h) by hand. In order to obtain the full ME scheme, also remove the restriction to the `tbj` processes. As explained above, at LO this only makes sense in combination with some acceptance cuts. To roughly home in on the signal region while leaving the detailed final state reconstruction including the disambiguation of the s and t channel to the detector level (cf. Sec. 4.2.2), we define basic acceptance cuts for the partonic phase space integration, which globally apply to both channels:

$$\Phi^{\text{part}}: \quad p_T(\ell,\nu) > 25\,\text{GeV} \quad \text{and} \quad |\eta(\ell)| < 3\,, \tag{4.2a}$$

$$p_T(j,b) > 30\,\text{GeV} \quad \text{and} \quad |\eta(j,b)| < 5\,, \tag{4.2b}$$

$$150\,\text{GeV} < m_{b\ell\nu} < 225\,\text{GeV}\,, \tag{4.2c}$$

where Eq. (4.2b) is required for only one of the two bs in the off-shell tbj processes to be inclusive[3]. On the other hand, for the resonant scheme enforce the subprocess $t \to \ell\nu b$ by adding a restriction `"3+4+5~t"` in all processes, and keep the one already present in `tbj`. Clearly, this is in conflict with gauge invariance, but this scheme is only used for some cross-checks later on in Ch. 5.

becomes significant especially in the more involved $2 \to 4$ and $2 \to 5$ processes later on.

[2] Part of the official WHIZARD release from version 2.2.0 onwards.

[3] Clearly, for full inclusiveness one would have to entirely drop the distinction of light and b flavors at partonic level, but the actual chance of mistagging the light forward jet is negligible once the full event topology (cf. tj selection in Sec. 4.2.2) is taken into account.

Finally, concerning all on-shell and off-shell process definitions in general, of course once the top is decayed there are more processes with the same final state signature at detector level (e. g. W + jets), because one cannot measure jet charge and also b tagging is impure, but these are reducible and hence independent of anomalous couplings. They can simply be added afterwards to any histogram or observable, and just enter the background normalization. Before moving on in Sec. 4.2 to the further simulation chain with which the partonic WHIZARD samples are processed to arrive at the detector level, let us shortly come back to the aforementioned issue of ME matching, and its WHIZARD implementation.

4.1.2. Matrix Element Matching

As argued in the previous section, whenever one has b flavor in the initial state there is a phenomenological need to correctly describe the kinematics of the second b from the gluon splitting $g \to b\bar{b}$, since it may be recovered in the final state. The splitting can be either fully included in the hard LO matrix element, or accounted for by a pdf with b flavor in combination with an ISR shower to produce the second b. The two approaches are not equivalent but rather complement each other: The hard LO ME poses a good approximation of the b jet at relatively high p_T but fails to describe the low p_T region due to large logarithms enhancing higher order QCD corrections,

$$\left(\frac{\alpha_s(Q^2)}{2\pi}\log\frac{Q^2}{Q_0^2}\right)^n \sim 1 \tag{4.3}$$

whenever the hard scale Q and the splitting scale Q_0 (e. g., p_T of the spectator b in our case) are well separated. On the other hand, the pdf/ISR shower approach goes to higher orders and hence contains a resummation of these logarithms, but it lives in the soft/collinear regime where $Q \gg Q_0$, and the splittings factorize well from the remaining ME. It therefore fails for large momentum transfers (large p_T of the b). Hence both approaches should be combined to cover the entire p_T spectrum, but this entails an obvious danger of double counting, because the LO term of the splitting function times the hard LO $2 \to 2$ ME is an approximation of the hard $2 \to 3$ ME in the soft/collinear phase space region.[4]

There exist different approaches in the literature to remove this double counting (i. e. *match* the MEs consistently, cf. [145, 146] or e. g. [106] for an overview), for instance by introducing an ad-hoc p_T cut to separate the hard ME from the ISR shower, where the actual cut value must be fixed "by eye" with regard to the different spectra (e. g. 10 GeV, as proposed by [79]). A theoretically more controlled approach, which will be pursued here, is to simply subtract the LO term from the $g \to b\bar{b}$ splitting function which is employed in a given pdf to convey a b quark distribution function. However, before moving on to the implementation, let us first have a brief look at the underlying theoretical machinery, cf. e. g. [147].

[4] Note that this is also another argument to exclude diagram (d) of Fig. 4.1 in the on-shell scheme without cuts, because the diagram emerges from kinking one of the light initial quarks of the LO s channel diagram (cf. Fig. 2.6) into the final state by a gluon splitting, exactly as diagram (b) results from (a) in the t channel, so there would also be some double counting there.

As already mentioned, protons or hadrons in general form a rather complicated initial state, because their substructure is governed by QCD in a strongly coupled regime which cannot be assessed perturbatively. However, it can be measured in restricted momentum/energy ranges Q, e. g. by deep inelastic scattering experiments such as the electron–proton collisions performed at HERA. The results are parton density functions $f_i(x, Q^2)$, which represent the probability density to find a parton of flavor i carrying a fraction x of the total hadron momentum when its substructure is resolved at a scale Q. On the other hand, there are the parton splitting functions $P_{ij}(z, Q^2)$ describing the splitting of a parton of flavor j into one of flavor i carrying a momentum fraction z of j, in the weakly coupled regime of QCD. Hence they are well-defined perturbatively as a series in $\alpha_s(Q^2)$,

$$P\big(z, \alpha_s(Q^2)\big) = P^{(0)}(z) + \frac{\alpha_s(Q^2)}{2\pi} P^{(1)}(z) + \left(\frac{\alpha_s(Q^2)}{2\pi}\right)^2 P^{(2)}(z) + \dots \,, \tag{4.4}$$

which is to date known up to NNLO [148, 149]. Already in the 1970s, several authors presented a formalism to use the RGE scale running of the perturbative P_{ij} for an evolution equation for the f_i, namely the famous Dokshitzer-Gribov-Lipatov-Altarelli-Parisi (DGLAP) equation [150–152]

$$\frac{\partial f_i(x, Q^2)}{\partial \log Q^2} = \frac{\alpha_s(Q^2)}{2\pi} \int_x^1 \frac{\mathrm{d}z}{z} P_{ij}\big(z, \alpha_s(Q^2)\big)\, f_j\left(\frac{x}{z}, Q^2\right) \,, \tag{4.5}$$

where experimental information on the f_j in a restricted range of Q, and for a subset of flavors j, is fed in and extrapolated to any Q of interest. The numerical solutions of Eq. (4.5) are the working basis for the entire pdf industry which makes statements about the proton structure at the Tevatron and LHC essentially from HERA results. Particularly, the matrix structure of Eq. (4.5) allows to generate heavy flavors, which are not contained in the initial f_j, from the gluon sea (e. g., there is no b flavor in the structure functions measured at the HERA scale). The b part of the LHC pdfs is thus in principle given by

$$f_b = P_{bg} \,\tilde{\otimes}\, f_g \,, \tag{4.6}$$

where $\tilde{\otimes}$ is a short-hand for the solution of Eq. (4.5) evaluated at a specific $Q = \mu_F$, the factorization scale set by the hard partonic process (in WHIZARD, $\mu_F = \sqrt{\hat{s}}$ by default). LHC cross sections are then obtained by summing over all contributing initial state flavors and convoluting the partonic ME with the respective $f_i(x, \mu_F^2)$. Hence, writing out only the b part of the initial state, a correctly matched partonic differential cross section for our t channel single top process can be termed as

$$\mathrm{d}\sigma = \underbrace{\left(f_b - P_{bg}^{(0)} \,\tilde{\otimes}\, f_g\right)}_{\equiv \tilde{f}_b} \otimes \left|\mathcal{M}_{bq\to tq'}\right|^2 + f_g \otimes \left|\mathcal{M}_{gq\to t\bar{b}q'}\right|^2 \,, \tag{4.7}$$

where the double counting is removed by subtracting exactly the LO term of Eq. (4.4) which is already contained in the (LO) $\mathcal{M}_{gq\to t\bar{b}q'}$.

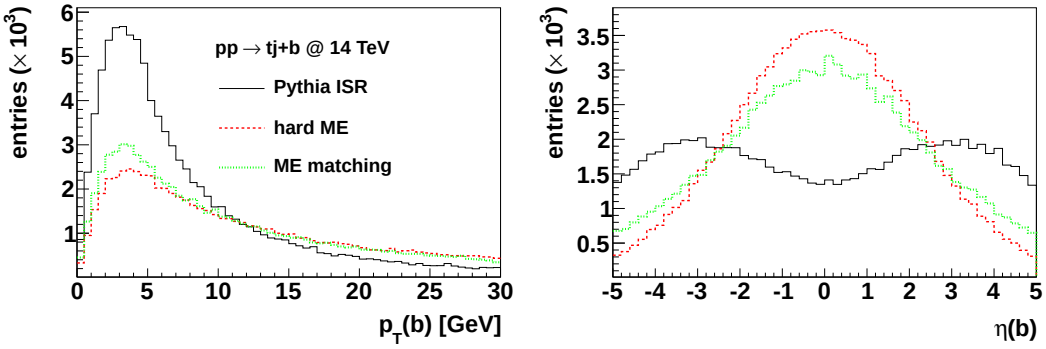

Figure 4.2.: Comparison of the differential distributions of the spectator b in t channel single top production (p_T left, η right), from PYTHIA ISR (black line), hard LO matrix element (red dashes), and a matched sample (green dots) at $\sqrt{s} = 14\,\text{TeV}$.

From release verion 2.2.0 onwards, WHIZARD provides the functionality to perform the matching of Eq. (4.7) on the fly, so that e. g. the processes tj and tbj (cf. Sec. 4.1.1) can be naively added up in a WHIZARD run. Internally, the b quark pdf is replaced by the new one $\tilde{f}_b$ introduced in Eq. (4.7), which is constructed as

$$\tilde{f}_b(x,Q^2) = f_b(x,Q^2) - \frac{\alpha_s(Q^2)}{2\pi}\log\frac{Q^2}{m_b^2}\int_x^1 \frac{\mathrm{d}z}{z}\,P_{bg}^{(0)}\big(z,\alpha_s(Q^2)\big)\,f_g\left(\frac{x}{z},Q^2\right) \qquad (4.8)$$
$$\text{with } P_{bg}^{(0)}(z) = \frac{z^2+(1-z)^2}{2}\,,$$

where f_b and f_g are taken from the original pdf set invoked in the beam definition. The actual operation (4.8) is performed by the program HOPPET [147], a tool to numerically solve the DGLAP equation at a fixed order in α_s. Once the program is linked to WHIZARD[5], the replacement $f_b \to \tilde{f}_b$ is invoked by setting the beam switch `?lhapdf_hoppet_b_matching` (as the name indicates, so far this only works with LHAPDF). Adding up the integrated cross sections of the partonic tj and tbj processes then gives the correct LO estimate, while processing the resulting partonic event samples with an appropriate shower algorithm will add the second b to those events originating from the partonic $\mathcal{M}_{bq\to tq'}$. Fig. 4.2 displays a comparison of p_T and η distributions of the spectator b obtained by the different mechanisms, illustrating that the hard $2 \to 3$ process dominates overall, however with significant corrections in the small p_T region.

4.2. Simulation Chain

The rest of the chapter is a short overview of the remaining two steps towards a full detector simulation, including the step of turning the hard parton level events

[5] You have to build HOPPET externally and configure WHIZARD with `HOPPET=<path>` and `--enable-hoppet` before compilation.

into fully hadronized truth level events containing only stable and meta-stable (decay lengths $\sim$ track resolution) color-neutral particles (Sec. 4.2.1), followed by the simulation of their impact inside the detector, eventually leading to measurable quantities and corresponding process signatures (Sec. 4.2.2, with a focus on single top final state selection).

4.2.1. Shower and Fragmentation

A parton level event as produced e. g. by WHIZARD comprises a set of usually $\lesssim 8$ hard particle momenta (of $\mathcal{O}(100\,\text{GeV})$ at the LHC with $\sqrt{s} = 14\,\text{TeV}$), among them leptons, photons and and colored partons (quarks and gluons). Although such particles will certainly show further interactions, due to large logarithms, cf. Eq. (4.3), these are governed by processes where the hard line radiates off another particle into the soft and collinear phase space regions around the original hard momentum. According to the factorization theorems [132], this can in good approximation be factorized from the hard scattering itself, and described by successive QED or QCD $1 \to 2$ splittings, the so-called final state radiation (FSR) or shower, where of course QCD is more important for the partons due to the larger coupling. In any case, having already introduced the splitting functions $P_{ij}(z, Q^2)$ in Sec. 4.1.2 (the principle applies to QED as well), the rest of this paragraph can be held quite concise: just use the RGE running of the P_{ij} together with the hard partonic momenta as input to generate cascades of particle splittings (populating mainly the soft/collinear regions), thus evolving the hard scale Q down to ever smaller values. The same reasoning basically applies to the *backwards* evolution of the initial state, thus leading to initial state radiation (ISR), which adds soft/collinear initial state partners to the event by reconstructing the $1 \to 2$ splittings contained in the DGLAP evolution, cf. Sec. 4.1.2.[6]

In QCD, this procedure is conceptually limited from below by the confinement scale $Q \sim \Lambda_{\text{QCD}} \sim \mathcal{O}(1\,\text{GeV})$ where QCD becomes strongly coupled, $\mathcal{O}(\alpha_s) \sim 1$, and the perturbation series of the P_{ij} breaks down, cf. Eq. (4.4). This is the scale where the open color lines must recombine to form color-neutral particles (i. e. mesons and baryons) in the final state, a process called hadronization or fragmentation. However, since it cannot be described by perturbative field theory any more, other means of description must be employed. Apart from numerical approaches using lattice QCD, there are heuristic models based on the qualitative knowledge of what should come out in the end, namely mainly stable and meta-stable mesons (and a few baryons) of the three light flavors u, d, s. These models can then be tuned quantitatively to the particle fractions observed in actual experiments. Among the many available fragmentation models, the two most widely used ones in current MC programs are HERWIG's cluster fragmentation [153] and the Lund string model included in PYTHIA [57]. On an even more sophisticated level, one can try to also include an underlying event description, which addresses the occurrence of further

[6] In principle, in both ISR as well as FSR there can be double counting with the hard scattering whenever splitting processes are already included in the partonic ME, so also FSR should be matched to the hard process as described in Sec. 4.1.2 for ISR.

QCD interactions connecting initial and final state along with the hard scattering.

Turning to WHIZARD, it is worth mentioning that the package already comprises its own built-in ISR/FSR shower algorithm, which also features an internal matching to the hard partonic ME. Yet since this was still subject to ongoing development at the time of writing this thesis, we have employed PYTHIA 6 [57] for ISR, FSR and fragmentation, thus benefiting from the fact that the tool is widely used in the community and hence heavily tested and tuned to the LHC experiments. Technically, WHIZARD was used to produce parton level event samples in the Les Houches Accord (LHA) format, which were then further processed externally with PYTHIA in the "Perugia 2011" tune [154] (based on the CTEQ6L1 pdf set chosen also in WHIZARD, cf. appendix C) to obtain truth level samples.

4.2.2. Detector Level

On top of the truth level samples, the remaining step is to simulate the impact of the various particle types onto the different components of a high energy particle detector. To that end, let us first briefly address the conceptual structure and typical dimensions of a current state-of-the-art high energy collider experiment such as CMS [155] and ATLAS [156] at the LHC.

A Generic LHC Multi-Purpose Experiment

Geometrically, a high energy particle collision experiment generally has a predefined symmetry axis z, namely the colliding particle beams, with a rotation symmetry in the azimuth angle φ. The rest depends on the initial beam setup, i. e. whether one has a fixed target experiment, as e. g. in LHCb, or a symmetric beam setup, as in the pp collision experiments ATLAS and CMS. In the latter case, another mirror symmetry with respect to the polar angle θ is given by the plane containing the interaction point and perpendicular to the beam, cf. Fig. 4.3 for illustration. In the special case of hadronic initial states, the business is complicated by the fact that the partonic c.m.s. frame is typically boosted along z against the lab frame to an unknown extent governed by the proton pdfs, hence it is more convenient to measure the polar direction in terms of the pseudorapidity η defined as

$$\eta \equiv -\ln\tan\frac{\theta}{2} \qquad \simeq \qquad y \equiv \frac{1}{2}\ln\frac{E+p_z}{E-p_z} \qquad \text{for } \frac{m}{E} \ll 1\,, \tag{4.9}$$

where y is the particle's rapidity, with the feature that any Δy and thus approximately $\Delta\eta$ is invariant under z-boosts. Other sensible quantities then are the invariant angular distance $\Delta R \equiv \sqrt{\Delta\eta^2 + \Delta\varphi^2}$ as well as the transverse momentum p_T, defined as the spatial momentum component in the $(z, \eta) = (0, 0)$ plane. Nonetheless, in such a setup there is one scalar information missing per visible particle to reconstruct the full 4-momentum, so in addition to the measured direction (η, φ) and one dimensionful quantity (p_T for the muons, E for the rest), one usually employs mass-shell conditions to reconstruct the full final state. However, at least the transverse momenta should sum up to zero in every event, so any measured imbalance, termed missing transverse energy $\not{E}_T$ though comprising two scalars, conveys

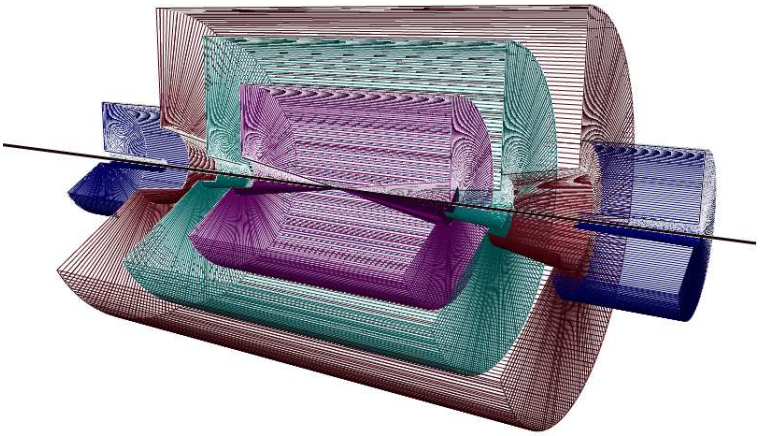

Figure 4.3.: Generic detector layout for high energy collider experiments used in DELPHES [58, 59]. From the interaction point to the outer shell, there is a central tracking system (pink), a central calorimeter volume (green) with both electromagnetic and hadronic sections, and a muon system (red). Two end-cap calorimeters (blue) extend the η coverage of the central system (picture and color code from [58]).

information on particles which have escaped detection, such as invisible particles like neutrinos or extremely forward particles.

Concerning the actual composition of such a detector, as a multi-purpose experiment it should be sensitive to as many particles types and energy/momentum ranges as possible, while also maximizing the solid angular acceptance. To that end, it usually consists of several layers arranged around the beam with the collision point in the center, dedicated to various tasks and particle species. As illustrated in Fig. 4.3, the components comprise an inner tracking system measuring particle tracks in a given magnetic field. Apart from determining charged track momenta, they are the key ingredients to the reconstruction of displaced decay vertices, which form the basis of the b tagging algorithm. The tracker is surrounded by a calorimeter system, consisting of an inner electromagnetic part (ECAL) to measure energies of photons and electrons, and an outer section (HCAL) measuring hadronic energy deposition. It was argued in Sec. 4.2.1 that hard partons undergo shower and fragmentation, thus forming a complex hadronic final state entering the detector. However, it was also shown that much of the activity is either soft or aligned with the original hard momentum, so one can define composite hadronic objects called jets at detector level by subsuming energy depositions clustered in a restricted area in the (η, φ) plane. Ideally, every jet corresponds to one hard parton, but obviously the jet definition depends on the particular algorithm employed to sort the calorimeter hits. Going on to muons, since they hardly interact with the previous layers (except for the tracker), a detector typically comprises a dedicated muon spectrometer as outer shell, where the momentum is measured by its deflection in a defined magnetic field (geometry

varying between ATLAS and CMS). Finally, every component mentioned so far has a counterpart in the end cap regions to further extend the sensitivity in $\pm\eta$.

Detector Simulation

The detector response to truth level momenta can be simulated in a greatly varying level of detail: for instance, the experimental collaborations themselves use very accurate software descriptions of their detectors including exact geometric dimensioning and matter filling to simulate all matter interactions of every single truth level particle in their full detector simulations, thus producing exactly the same data pattern as an actual event. From these digital hits, final state objects such as photons, jets and so on are reconstructed by successive algorithmic steps. However, once the overall detector performance is determined by such full simulations and experimental input, the detector response can simply be *parametrized* using the respective angle-resolved performance indicators like resolutions and efficiencies.

One of the available programs performing such a fast detector simulation, which has been used throughout this thesis, is DELPHES [58, 59]. Its general detector layout has already been introduced in the previous paragraph, cf. Fig. 4.3. Within DELPHES, a particular detector is specified by giving the angular extensions and cell spacings of the various components in the (η, φ) plane, along with the magnetic field configuration. Any input track is reconstructed to a given percentage, without (η, φ) smearing but accounting for magnetic field effects, whereas the energy loss inside the ECAL and HCAL is smeared according to Gaussian resolution values as functions of the target cell and particle type[7], with additional p_T smearing inside the spectrometer in the case of muons. Specific experiments are initialized within DELPHES by providing the program with a corresponding detector chart where all these parameters have been tuned to resemble the actual values as much as possible. For this thesis, the default ATLAS chart shipped with the package has been employed (merely resetting the b tagging efficiency to 0.6 globally).

Final State Reconstruction

Irrespective of the simulation method (full or fast), a detector level event usually consists of a list of object *candidates* classified according to some basic selection criteria such as energy thresholds, track matching and so on, where we choose the anti-k_T algorithm [157] as implemented in DELPHES to define ECAL/HCAL candidates. However, such candidates generally still show a considerable overlapping which requires further high-level reconstruction to obtain some definite final state signature (like "x leptons + y jets + $\not{E}_T$"), with notorious classics being e. g. photon/-pion or jet/electron disambiguation. While the former is of minor importance to the single top analysis performed in Ch. 5, the latter one is accounted for in DELPHES

[7] Note that usually the detected amount of energy is reduced due to particles escaping overall detection, which is accounted for in real experiments by energy-dependent rescaling functions, but this was not implemented yet in the latest DELPHES version relevant for this thesis (3.0.9). The result is that the reconstructed jets tend to lose energy (and hence also p_T) when going from truth level to detector level, but the effect on the top signal was checked to be small.

as follows: whereas fake electrons are entirely neglected, generator electrons produce an electron candidate whenever they are within tracking acceptance, but may additionally fake a jet candidate. These fake jets are removed by a matching to the electron candidates: whenever a jet candidate has an electron candidate within an angular cone $\Delta R < 0.1$ and carries a minimum energy $E_j/E_\ell > 0.7$ of that electron, it is discarded from the list. On the other hand, the electron (and muon) purity is improved by an isolation cut defined as a veto on additional tracks with $p_T/p_T(\ell) > 0.1$ inside a fixed cone $\Delta R < 0.5$ around the lepton.

One thus arrives at final states with definite signatures (of course still depending on some quality cuts, but this is beyond the scope of this work), on top of which further kinematic selection cuts can be applied, e. g. to suppress background and improve the signal purity. Turning now to the particular case of single top selection in the s or t channel, the selection criteria should obviously include the decay products of the decaying top, namely a hard charged lepton (that is, e or μ) and a hard b jet plus missing transverse energy from the neutrino. In addition, the channel-specific selections require one additional hard b jet in the s channel resp. one very hard light jet in the extreme forward directions in the t channel, while any kinds of reducible backgrounds, most prominently $t\bar{t}$ and W + jets production, are suppressed by a veto on additional jet activity in the event. For later comparison reasons, we adopt the detailed setup of final state selection cuts stated in [79]: apart from requiring an isolated lepton with $p_T > 25\,\mathrm{GeV}$ and missing transverse energy $\not{E}_T > 25\,\mathrm{GeV}$, the selection criteria for the two final state signatures are, respectively

1. for s channel or "tb" selection: exactly two b tagged jets with $p_T > 30\,\mathrm{GeV}$, and neither central nor forward light jets with $p_T > 15\,\mathrm{GeV}$. In addition, the top momentum p_t is reconstructed from one of the bs together with the charged lepton and $\not{E}_T$ (to be identified with the neutrino p_T), by applying the on-shell constraint $(p_\ell + p_\nu)^2 = m_W^2$ and picking the smaller of the two solutions for the longitudinal component of p_ν. Finally, the resulting top mass must lie between 150 and 225 GeV.

2. for t channel or "tj" selection: at least one b jet with $p_T > 30\,\mathrm{GeV}$ (one of them reconstructing p_t together with the leptons as explained above), one light forward jet with $p_T > 50\,\mathrm{GeV}$ and $2.5 < |\eta| < 5$ and no more than one additional light central jet, which may have $p_T < 30\,\mathrm{GeV}$ only.

Note that the universal partonic acceptance cuts applied on the full MEs, Eq. (4.2), have been deliberately designed such that they contain the entire phase space regions of the final state selections stated here for *any* of the two channels. The detector simulation procedure thus allows not only to determine the reconstruction efficiencies but also their mutual contamination, i. e. the off-diagonal elements of the detector response matrix mapping partonic input processes onto final state selections.

5. Single Top Cross Sections at the LHC

There are many different classes of observables which are potentially sensitive to an anomalous top charged-current sector, some of which were already introduced in more detail in Sec. 2.5. While it is clear that only a combination of all available observables will deliver the best bounds on anomalous contributions, it is crucial to understand each analysis separately before the combination step. In this chapter, the focus will be on direct observables accessible at the current LHC experiments, concentrating particularly on single top production, but also citing and using results from top decay studies to derive estimates for the most stringent bounds on the full anomalous parameter space at the end of the chapter.

To that end, in Sec. 5.1 (following [55]) we will first restrict the set of anomalous CC couplings to the trilinear ones and examine the sensitivity of total single top cross sections, extending existing studies by a detailed discussion of the interplay among production and decay in full matrix elements, and also of the influence of the coupling V_L^{off}, cf. Eq. (2.24), which was previously dropped from the trilinear list. In Sec. 5.2, it will be argued how decay observables serve to independently assess the trilinear couplings, while the single top cross sections remain the only window to anomalous CC contact interactions at the LHC. Finally, experimental sensitivities to the most general set of these couplings in the MFV scheme will be presented.

5.1. Total Cross Sections and Trilinear Couplings

Since the stage for single top LHC studies has already been set in the previous chapters, we can directly proceed to the phenomenological impact of anomalous CC top couplings

$$\vec{g} = \left\{ V_L, V_R, g_L, g_R, V_L^{\text{off}} \right\} \ , \tag{5.1}$$

cf. Eq. (2.24), on total cross section measurements. The theoretical question is how the measured cross sections σ_i^{det} (for final states $i = tb, tj$) are represented as functions on the anomalous parameter space, i. e. how the measurement can be converted into bounds on the parameters. In this respect, a first step may be to separate the detector response from the hard production cross section:

$$\sigma_i^{\text{det}}(\vec{g}) = \sum_j \varepsilon_{ij} \cdot \sigma_j^{\text{part}}(\vec{g}) \ , \tag{5.2}$$

summing over partonic production processes j as functions of the parameter point $\vec{g}$. ε_{ij} denotes the detector efficiency matrix mapping the process j onto the final state selection i, which was already mentioned at the end of Sec. 4.2.2. Once the functions

$\sigma_i^{\text{part}}(\vec{g})$ are known, experimentally measured confidence intervals for σ_i^{det} can be mapped onto confidence intervals for $\vec{g}$ by formal inversion of Eq. (5.2).

However, the remaining question to be addressed in this approach is: Where did we put the detector acceptance Φ, into ε or into σ_i^{part}? The significance of this question is obvious, since anomalous couplings might very well affect the differential distributions, thus making Φ a function of $\vec{g}$. Therefore, the answer to that question influences the strategy as well as the efforts necessary to compute the function $\sigma_i^{\text{part}}(\vec{g})$, and potentially also the bounds derived from it, as we will show in the following section.

5.1.1. Technical Setup

On-shell Approach

The simplest approach is to neglect the $\vec{g}$-dependence entirely and pull the acceptance into ε, implying that the $\sigma_i^{\text{part}}(\vec{g})$ in Eq. (5.2) represent the set of total partonic cross sections integrated over the full phase space. Further neglecting finite width and interference effects with irreducible backgrounds enables one to decompose $\sigma_i^{\text{part}}(\vec{g})$ as

$$\sigma_i^{\text{part}}(\vec{g}) = \sigma_i^{\text{prod}}(\vec{g}) \times \prod \mathcal{BR} \ , \tag{5.3}$$

where $\sigma_i^{\text{prod}}(\vec{g})$ denotes the full on-shell single top production cross sections, and the product of branching ratios accounts for the decays of the heavy particles, namely t and one or two Ws, depending on the production channel. Since all the on-shell production diagrams can contain only one anomalous tbW vertex insertion, it is argued in [79] that $\sigma_i^{\text{prod}}(\vec{g})$ may be written as a polynomial up to second order in $\vec{g}$:

$$\sigma_i^{\text{prod}}(\vec{g}) = \sigma_i^{\text{SM}} \sum_{k,l} \kappa_{kl}^i \, g_k \, g_l \ , \tag{5.4}$$

where the σ_i^{SM} are the total SM cross sections, and the κ_{kl}^i denote the integrated products of diagrams with one insertion of g_k and g_l each, normalized to the SM point in each production channel i. Plugging (5.3) and (5.4) into (5.2), one arrives at the ansatz employed in [79]:

$$\begin{aligned} \sigma_i^{\text{det}}(\vec{g}) &= \sum_{j,k,l} \left[\varepsilon \times \prod \mathcal{BR} \right]_{ij} \cdot \sigma_j^{\text{SM}} \cdot \kappa_{kl}^j \, g_k \, g_l \\ &\equiv \sum_{j,k,l} \varepsilon_{ij} \cdot \sigma_j^{\text{SM}} \cdot \kappa_{kl}^j \, g_k \, g_l \ . \end{aligned} \tag{5.5}$$

For brevity, this will be referred to as *on-shell approach* from here on (corresponding of course to the definition of on-shell production processes in WHIZARD as given in Sec. 4.1). The advantage of the formula is obvious: once ε and the constant κs are known, the conversion of measured results into bounds on $\vec{g}$ becomes very simple and efficient. However, the validity of the assumptions leading to this result shall be addressed now.

Full Matrix Element Approach

Eq. (5.5) tells us that one should be able to vary the coupling point $\vec{g}$ within the ranges relevant for the study, with only minor effects on the detector response ε in the phase space window which corresponds to a given final state selection. However, Eq. (5.5) implies even more, namely that retrieving the matrix element response as a function of $\vec{g}$ and applying acceptance cuts on the phase space should approximately commute, or equivalently, Eq. (5.5) should give the same results as e. g.

$$\sigma_i^{\text{det}}(\vec{g}) = \sum_j \varepsilon'_{ij} \cdot \left[\Phi^{\text{part}} \times \sigma^{\text{part}}\right]_j (\vec{g}) \,, \tag{5.6}$$

where the basic detector acceptance cuts such as p_T and η cuts on the partons and leptons, represented by Φ^{part}, are applied directly to the phase space integration and hence formally included in the $\vec{g}$-dependent part of the formula, while the matrix ε', assumed to be constant in $\vec{g}$, denotes the efficiency of mapping the partonic final states *at the acceptance level* Φ^{part} onto the final state selections at detector level.

To be more explicit, the idea is to accommodate as much of the acceptance cuts as possible within the $\vec{g}$-dependent part without becoming exclusive to any of the different final state selections, which are still contained in the $\vec{g}$-independent ε'. This obviously implies that the phase space window covered by ε' must be fully contained within the acceptance window Φ^{part}, leading to the notion that partonic acceptance and final state selection cuts should be adapted to each other as closely as possible. Assuming leptonic t decay, this leads exactly to the definition of the universal partonic acceptance cuts Φ^{part} already given in Eq. (4.2), which are in direct correspondence to the detector level selection criteria stated in Sec. 4.2.2 for the tb and tj channel. Associated tW production has been entirely omitted, with arguments stated in Sec. 4.1. However, now there is yet another argument, because modelling this process within its detector acceptance window while at the same time remaining inclusive with respect to the other processes is highly nontrivial, and only marginally affects our following statements[1]. Clearly, this approach is still not the fully correct answer at detector level, but it should be closer to the truth than entirely neglecting the $\vec{g}$-dependence of ε, and the consistency of the two approaches can be checked.

Although it is clear that the object $\left[\Phi^{\text{part}} \times \sigma^{\text{part}}\right]_i (\vec{g})$ to be computed is much harder to handle than the constant κs (even more so if the full matrix element response including all off-shell and interference effects is to be taken into account), it is basically just a technical issue which can be tackled with appropriate Monte Carlo machinery and respective CPU time. For brevity, we will refer to this approach as *full matrix element (ME) approach* from now on (with respective WHIZARD process definitions for full partonic MEs to be found in Sec. 4.1). In the following section, we compare the results of Eq. (5.5) and Eq. (5.6), and see if the effort is justified.

[1] The main effect is the neglected contamination of the other final states at the detector level, which amounts to $\lesssim$10 % in the tb channel and practically vanishes in the dominant tj channel. Still, it is clear that in the end also this channel should be addressed and included in a complete study.

5.1.2. Comparison of the On-shell Limit With the Full Result

For the measurement of the total cross section of a given final state at the detector level, the experimental sensitivity is given in terms of a measure for $\Delta\sigma/\sigma$, where estimations for total uncertainties are adopted from [79] for benchmarking, amounting to 20.8 % (tb sel.) and 13.5 % (tj sel.) for $10\,\mathrm{fb}^{-1}$ of LHC data at $\sqrt{s} = 14\,\mathrm{TeV}$. Therefore, we separate the overall normalization, which is basically given by higher-order SM results for the total production cross sections, from the modelling of the normalized LO matrix element response as a function of the anomalous coupling set $\vec{g}$, i. e. the κ_{on} coefficients in the on-shell approach or, more generally, a function $\Delta\sigma/\sigma(\vec{g}) \equiv \kappa(\vec{g})$ for each partonic input process i, where

$$\text{on-shell:} \qquad \kappa^i_{\mathrm{on}}(\vec{g}) = \sum_{k,l} \kappa^i_{kl}\, g_k\, g_l\,, \tag{5.7a}$$

$$\text{full ME:} \qquad \kappa^i_{\mathrm{full}}(\vec{g}) = \frac{\left[\Phi^{\mathrm{part}} \times \sigma^{\mathrm{part}}\right]_i(\vec{g})}{\left[\Phi^{\mathrm{part}} \times \sigma^{\mathrm{part}}\right]_i|_{\mathrm{SM}}}\,, \tag{5.7b}$$

cf. Eqs. (5.5) and (5.6). Since the aim is to accommodate *all* coupling dependence therein, it is fruitful to first set $\varepsilon \equiv 1$ and compare this function for the different approaches at the partonic level.

Partonic Level

To benchmark our approach, we essentially redo the analysis procedure presented in [79] for the on-shell approach, employing WHIZARD as described in Sec. 4.1 to compute the coefficients of κ_{on} as well as produce parton level samples, which are then further processed according to Sec. 4.2 to obtain detector level events and eventually retrieve ε. The quadratic coefficients (i. e. $\sim g_i^2$) are obtained in each production channel by separately setting each $g_i = 1$, integrating the total cross section for on-shell single top production and finally normalizing to the SM point ($V_L = 1$, $V_R = g_{L,R} = 0$). The interference terms are computed similarly, setting always two couplings to 1 and subtracting the quadratic parts from the result before normalizing to the SM. The WHIZARD input setup employed for this analysis is summarized in appendix C.

In the full ME approach, the matrix element response is modelled according to Eq. (5.7b) by applying the acceptance cuts Φ^{part}, Eq. (4.2), to the full partonic off-shell MEs as described in Sec. 4.1. In this approach, taking all finite width and interference effects into account, it is a priori not clear that the function $\kappa_{\mathrm{full}}(\vec{g})$ obeys a simple polynomial expansion in $\vec{g}$, so rather than assuming a specific functional form, we use the WHIZARD machinery to scan the entire 4-dimensional parameter space $\vec{g} = (V_L, V_R, g_L, g_R)$ (effects of V_L^{off} will be addressed separately in Sec. 5.1.3) within the relevant numerical ranges $0 < V_L < 1.2$, $-1.2 < V_R < 1.2$ and $-0.6 < g_{L,R} < 0.6$ (cf. [79]), also including the full dependence of the top width on the couplings $\Gamma_t(\vec{g})$. Since Γ_t has already been measured, the most recent bound from DØ being $\Gamma_t = 2.00^{+0.47}_{-0.43}\,\mathrm{GeV}$ [95], it is included in our analysis as an additional

observable[2]. The numerical results can then be used to test the validity of the polynomial parametrization, Eq. (5.7a), in the following way: The normalized matrix element response κ may always be expanded as

$$\kappa\left(\vec{g}\right) = \sum_i \kappa_1\left(g_i\right) + \sum_{i,j} \kappa_2\left(g_i, g_j\right) + \sum_{i,j,k} \kappa_3\left(g_i, g_j, g_k\right) + \ldots , \tag{5.8}$$

where the κ_i are polynomials in their respective arguments. Offsets κ_0 from squared irreducible background diagrams could be considered, but are obviously independent of $\vec{g}$ and merely add to the background normalization, so we just subtract them from the scans, while keeping all interference effects (appearing as terms linear in the g_i in κ_1) for completeness. Usually this series terminates after κ_2, which becomes obvious when applying the narrow width approximation, where additional coupling effects cancel in the interplay of the decay vertex insertion, width dependence and phase space integration. This basically leads to the quadratic form in the on-shell approach. However, in the special case of single tops, production and decay are interrelated via the same set of CC couplings, thus affecting production as well as decay distributions, which in combination with the detector acceptance cuts might lead to deviations from the on-shell result in some regions of the parameter space[3].

In order to estimate the size of the moments κ_3, in our cross section scans we consider 2-dimensional subplanes (g_i, g_j) among the anomalous couplings (V_R, g_L, g_R) for different fixed values of V_L. After subtracting all the lowest moments,

$$\Delta\kappa(\vec{g}) = \kappa(\vec{g}) - \sum_{k=i,j,V_L} \kappa_1(g_k) - \sum_{k=i,j} \kappa_2(g_k, V_L)\,, \tag{5.9}$$

within the on-shell picture the remaining contribution $\Delta\kappa(\vec{g}) \sim \kappa_2(g_i, g_j)$ should then be independent of the value of V_L, otherwise it would by definition contain some $\kappa_3(g_i, g_j, V_L)$. For illustration, we choose the coupling subspace $(g_i, g_j) = (V_R, g_L)$, because it is one of the dominant interference contributions to all production processes, and evaluate $\Delta\kappa|_{V_L=1.2} - \Delta\kappa|_{V_L=0.2}$. The resulting picture is mixed: while in the s channel the result is practically 0 all over the V_R–g_L plane, in the t channel processes $\bar{t}(b)j$[4], which play a central role because of the comparably large cross section, this difference amounts to ~ -0.2 at $V_R \simeq \pm 1$ and $g_L \simeq \pm 0.5$ along the

[2] Clearly the experimental analysis performed in [95] to extract Γ_t from data will itself also be affected by $\vec{g}$ dependent acceptances as discussed here. However, since we do not aim at a reassessment of their analysis in this respect, yet also want to exclude regions in parameter space which are completely unphysical with respect to Γ_t, we still include the observable, inferring the $\Gamma_t(\vec{g})$ dependence over the full phase space. This approach is conservative, because our results indicate that including the full acceptance dependence generally tends to improve the sensitivities, cf. e. g. Fig. 5.3. A posteriori, we find that, due to the still large error bars, the current measurement of Γ_t constrains $\vec{g}$ much less than the cross sections. The limits on $\vec{g}$ would therefore not be affected substantially by such a reassessment.

[3] Note that this is a qualitative difference to QCD (LHC) or NC (ILC) $t\bar{t}$ production, where production and decay are affected by different sets of anomalous couplings.

[4] At this level, we keep the partonic processes tj and tbj distinct, in order to examine their individual response to anomalous couplings. They will be merged according to Sec. 1.2.2 at detector level.

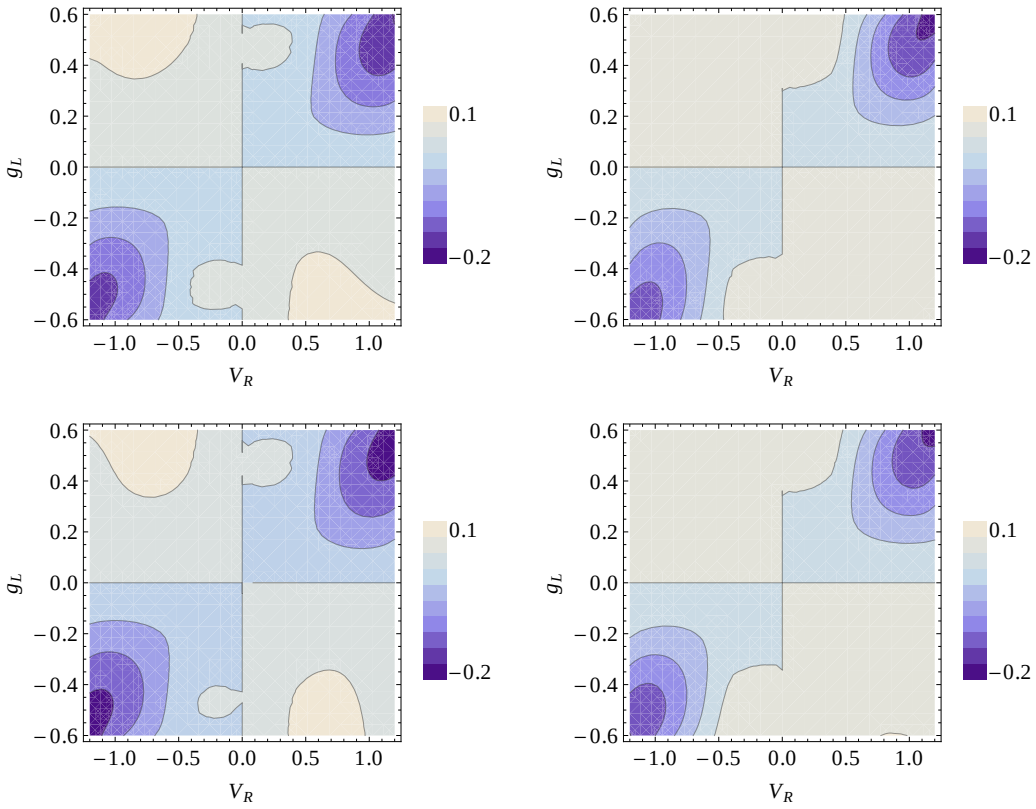

Figure 5.1.: $\Delta\kappa|_{V_L=1.2} - \Delta\kappa|_{V_L=0.2}$ in the $\bar{t}j$ process (left) and $\bar{t}bj$ process (right), based on full matrix elements (top) and resonant diagrams (bottom).

interference direction $V_R \sim 2g_L$ (cf. Fig. 5.1), which is of the same size as the respective on-shell contribution $\sim -0.5 \times V_R \times g_L$, (the same is true for the $V_L g_R$ interference in the tj channel). For comparison, we repeat the whole procedure employing the resonant ME approach described in Sec. 4.1 for the scan (including the full top width dependence on $\vec{g}$), finding that background interference only plays a minor role.

Furthermore, note that there are other interference directions also showing substantial effects, e. g. in the g_L–g_R plane of the s channel, but the $V_R g_L$ interference is the most interesting one because it is large in all channels, and respective bounds are expected to remain rather weak also from other experiments along the considered direction $V_R \sim 2g_L$ [79]. All in all, these numbers indicate strongly that the interference and off-shell effects contained in the full matrix elements might become important at the level of the coupling limits to be expected experimentally, at least in a stand-alone single top cross section study at the LHC, and should be checked in any case.

In order to further quantify this effect and exclude potential artefacts from unphysical regions in the parameter space, we now systematically scan the $V_R g_L$ inter-

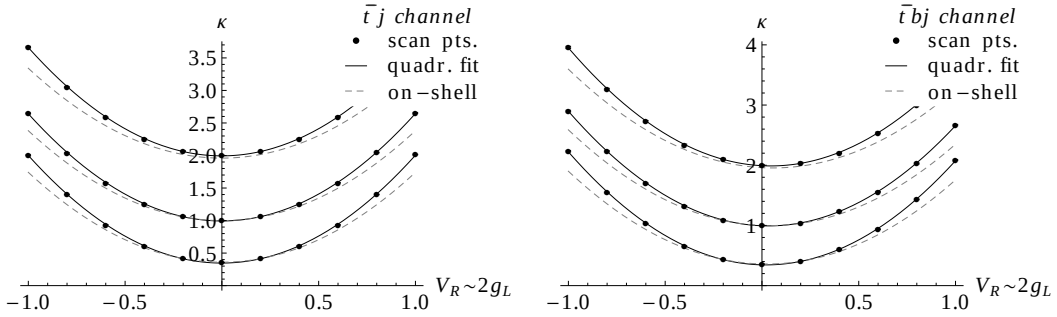

Figure 5.2.: κ scan results and quadratic fits of resonant matrix elements inside the acceptance region along the coupling direction $V_R \sim 2g_L$, for $V_L = 0.6$, 1.0 and 1.4 (bottom to top) in the $\bar{t}j$ channel (left) and the $\bar{t}bj$ channel (right). Grey dashed lines indicate the on-shell κ function.

ference along the direction $V_R \sim 2g_L$ as a function of V_L, including resonant off-shell diagrams for anomalous single top production and decay. We observe that the scans do show a quadratic dependence on V_R and g_L to a very good approximation at any value of V_L (cf. Fig. 5.2), so the respective coefficients $\kappa_{V_R} \sim V_R^2$, $\kappa_{g_L} \sim g_L^2$ and $\kappa_{V_R g_L} \sim V_R\, g_L$ can be extracted from quadratic fits along the axes V_R, g_L and $V_R = 2g_L$, for each fixed value of V_L and $g_R = 0$. This is done for the full phase space integration as well as for the acceptance region defined in Eq. (4.2). As illustrated in Fig. 5.3 for the t channel processes, when integrating over the full phase space the deviations from the on-shell result are very small as expected from the narrow width approximation, whereas application of the acceptance cuts leads to substantially different fit coefficients which also depend on the value of V_L.

Particularly this dependence of the magnitude of the $V_R g_L$ interference on V_L is an example for the breakdown of the quadratic on-shell approach. However, this dependence is rather small in κ_{V_R} and κ_{g_L} which come with squares of the respective couplings and therefore dominate the sensitivity of a given process to these couplings, so it might still be a good approach to expand the full κ_{full} as a quadratic form in *small* anomalous deviations from the SM point $V_L = 1$, namely by choosing $V_L = 1$ as an origin. As explained before, the numerical values are extracted from quadratic fits to 1-dimensional coupling scans (including acceptance cuts) in all directions of $\vec{g}$, and all interference directions $g_i g_j$. A major difference to the original on-shell quadratic form is the appearance of large linear terms in the couplings, which now encode the interference with the SM. In Figs. 5.4 and 5.5, we compare the different quadratic parametrizations, namely κ_{on} from the on-shell approach and κ_{fit} inferred from the fits, to the full ME response κ_{full}, illustrating two statements: Firstly, κ_{on} significantly deviates from κ_{full} in various parts of the parameter space relevant to the analysis, particularly in the g_L–g_R and V_R–g_L planes. Secondly, although still neglecting the higher coupling dependences, κ_{fit} inferred from quadratic fits to the full scan does show a significantly improved agreement with the full scan while still being fast and efficient. This is further illustrated in Fig. 5.6 and 5.7 showing $\pm 1\sigma$

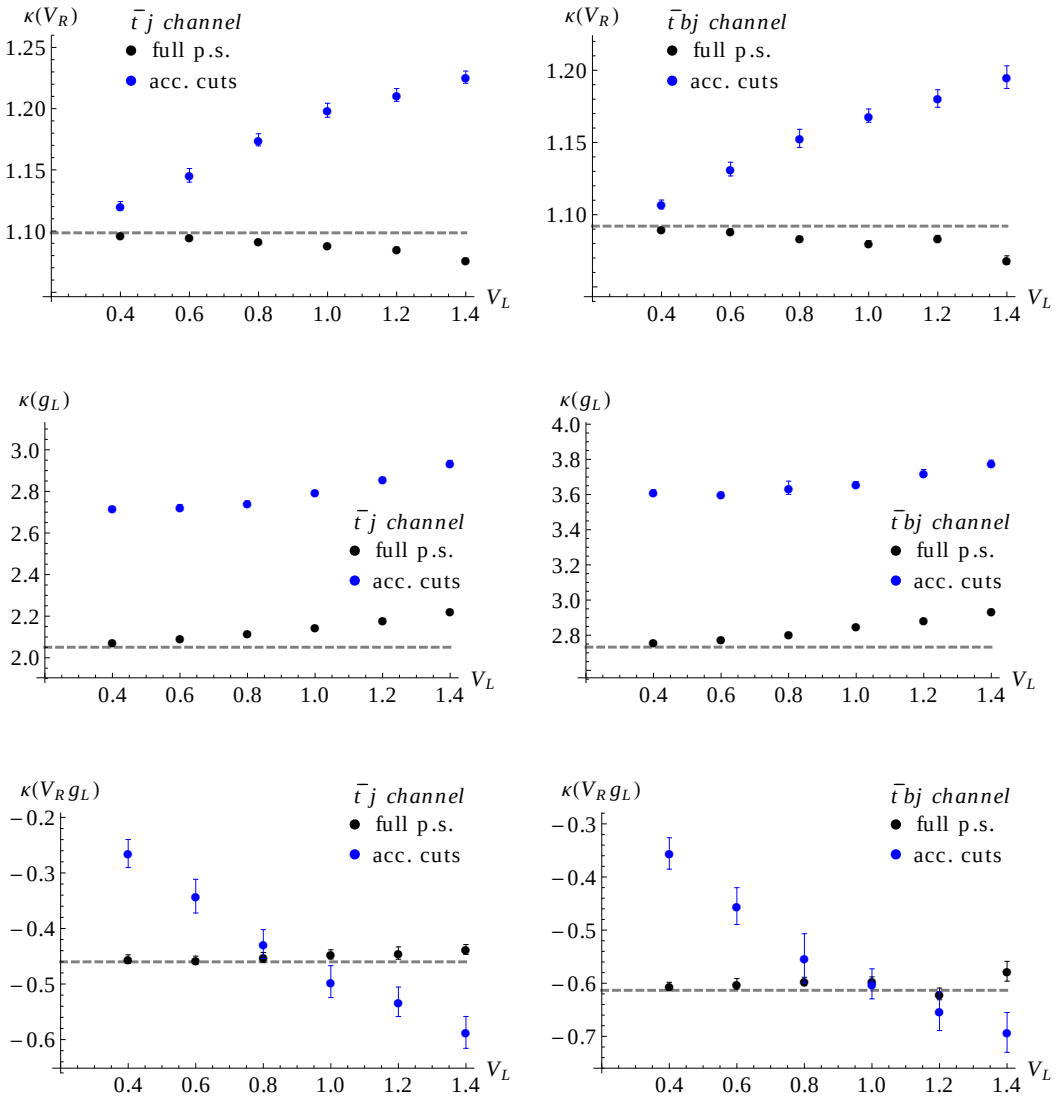

Figure 5.3.: Numerical results for various κs in the processes $\bar{t}j$ (left) and $\bar{t}bj$ (right), as extracted from quadratic fits to the normalized cross sections. The dashed line indicates the value of the on-shell κ in each case.

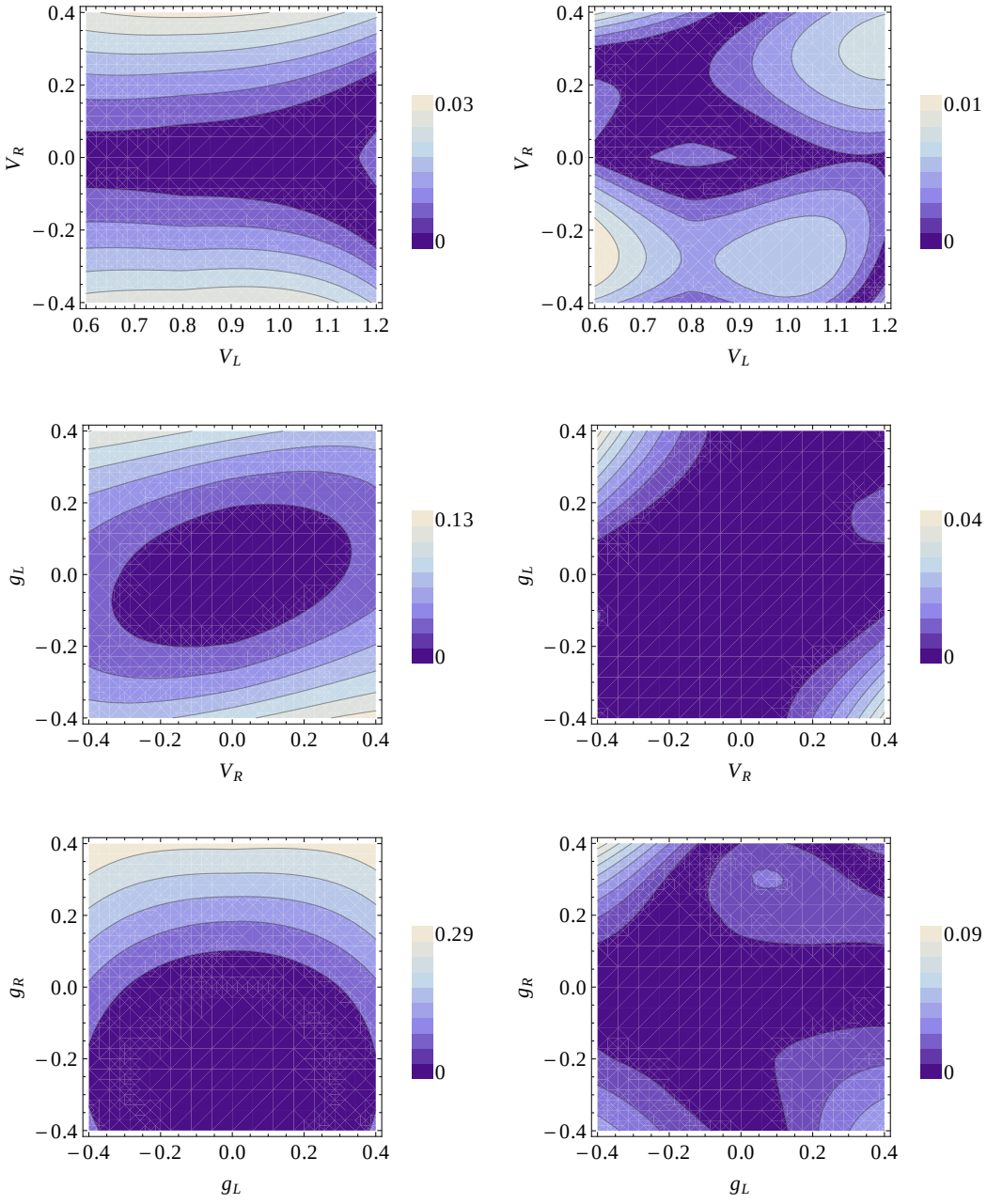

Figure 5.4.: The differences $|\kappa_{\text{full}} - \kappa_{\text{on}}|$ (left) and $|\kappa_{\text{full}} - \kappa_{\text{fit}}|$ (right) in various coupling planes of the $\bar{t}j$ process. Note that the heat scales on the left are of the size of the expected experimental sensitivity to the t channel ($\sim 13\,\%$), and significantly decrease on the right.

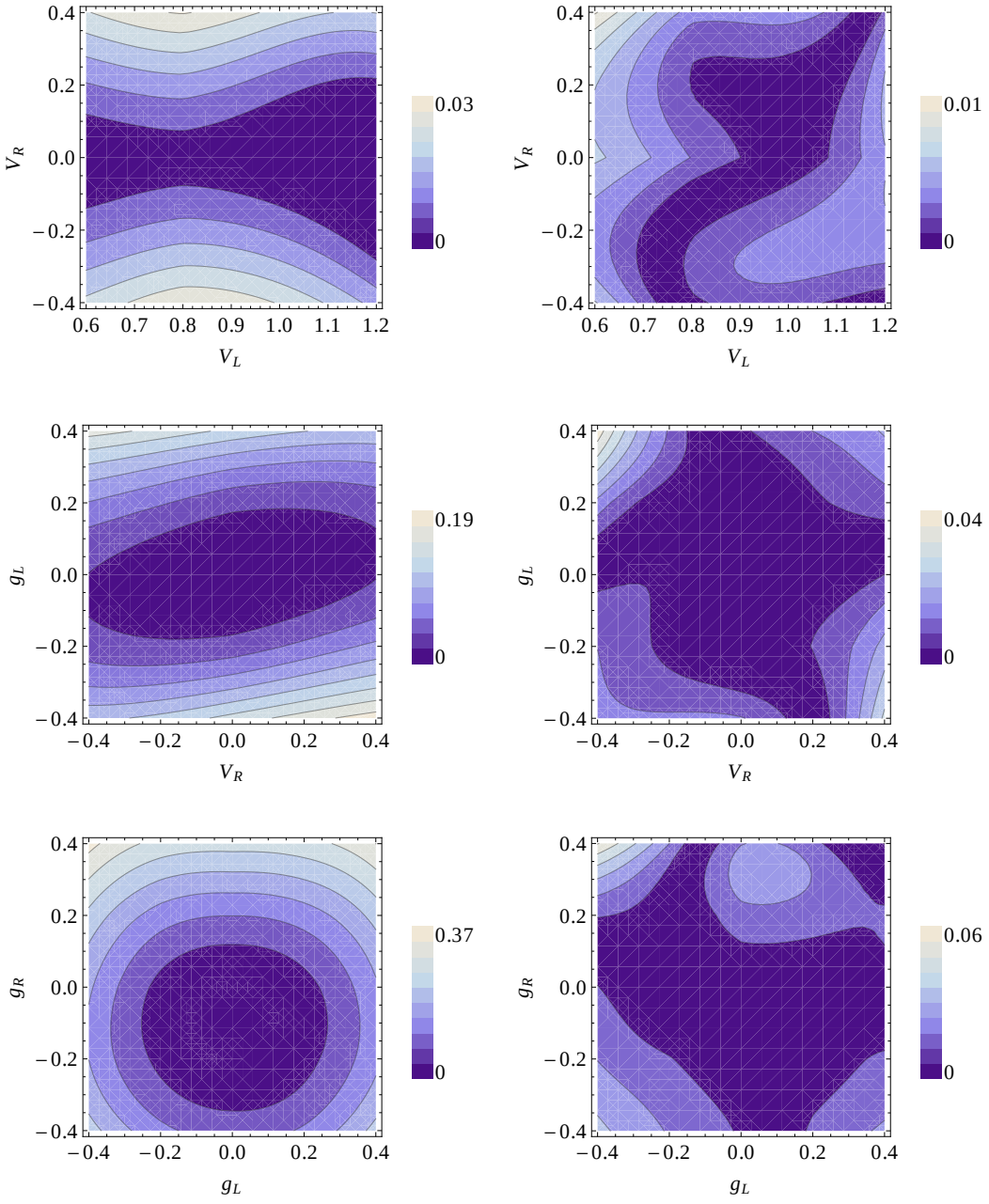

Figure 5.5.: The differences $|\kappa_{\text{full}} - \kappa_{\text{on}}|$ (left) and $|\kappa_{\text{full}} - \kappa_{\text{fit}}|$ (right) in various coupling planes of the $\bar{t}bj$ process (note the heat scales, cf. discussion in Fig. 5.4).

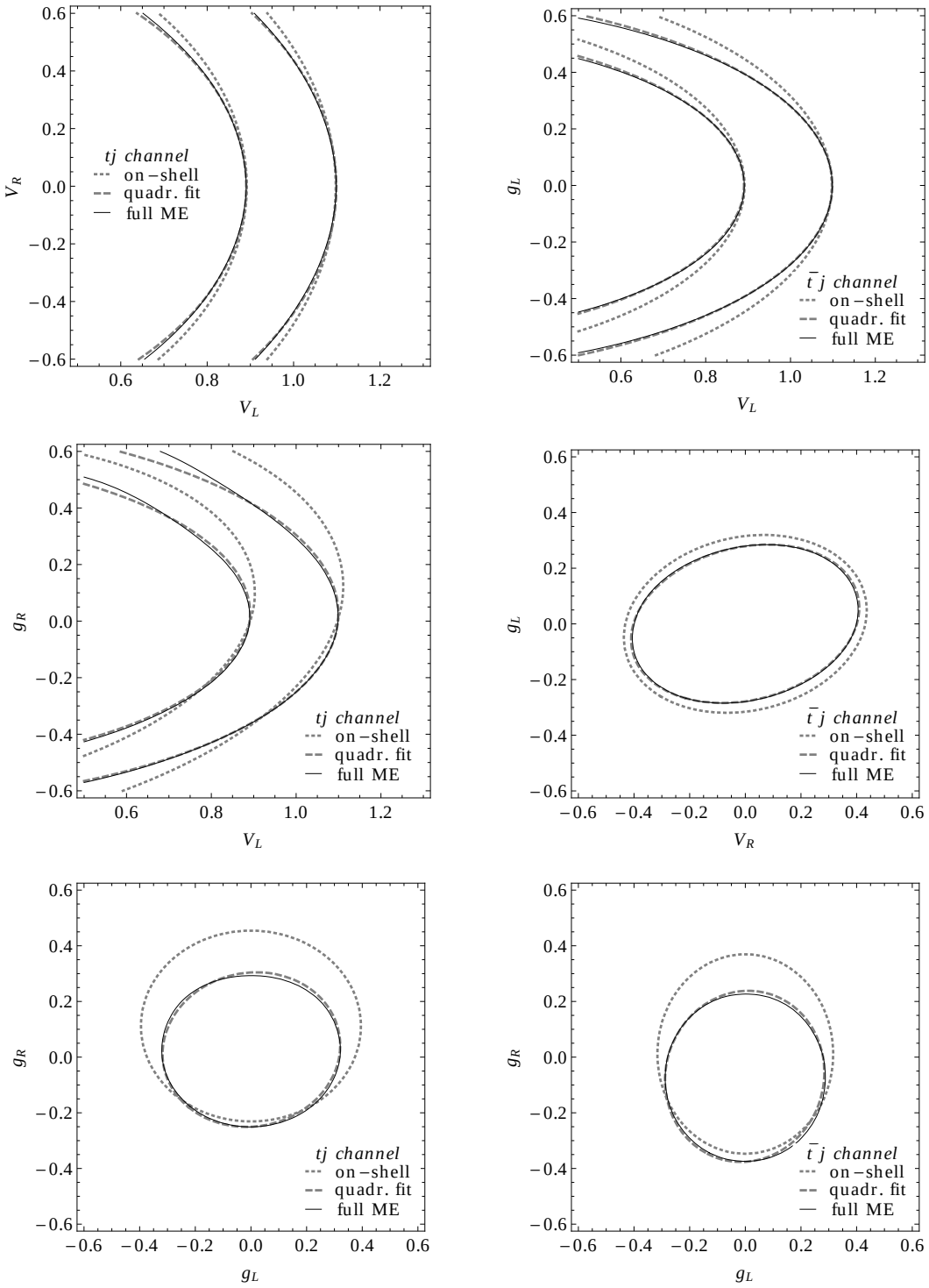

Figure 5.6.: Comparison of the 1σ contours for the various matrix element response functions κ_{on}, κ_{fit} and κ_{full} at parton level, for tj and $\bar{t}j$ production processes in different coupling planes (setting all others to the SM).

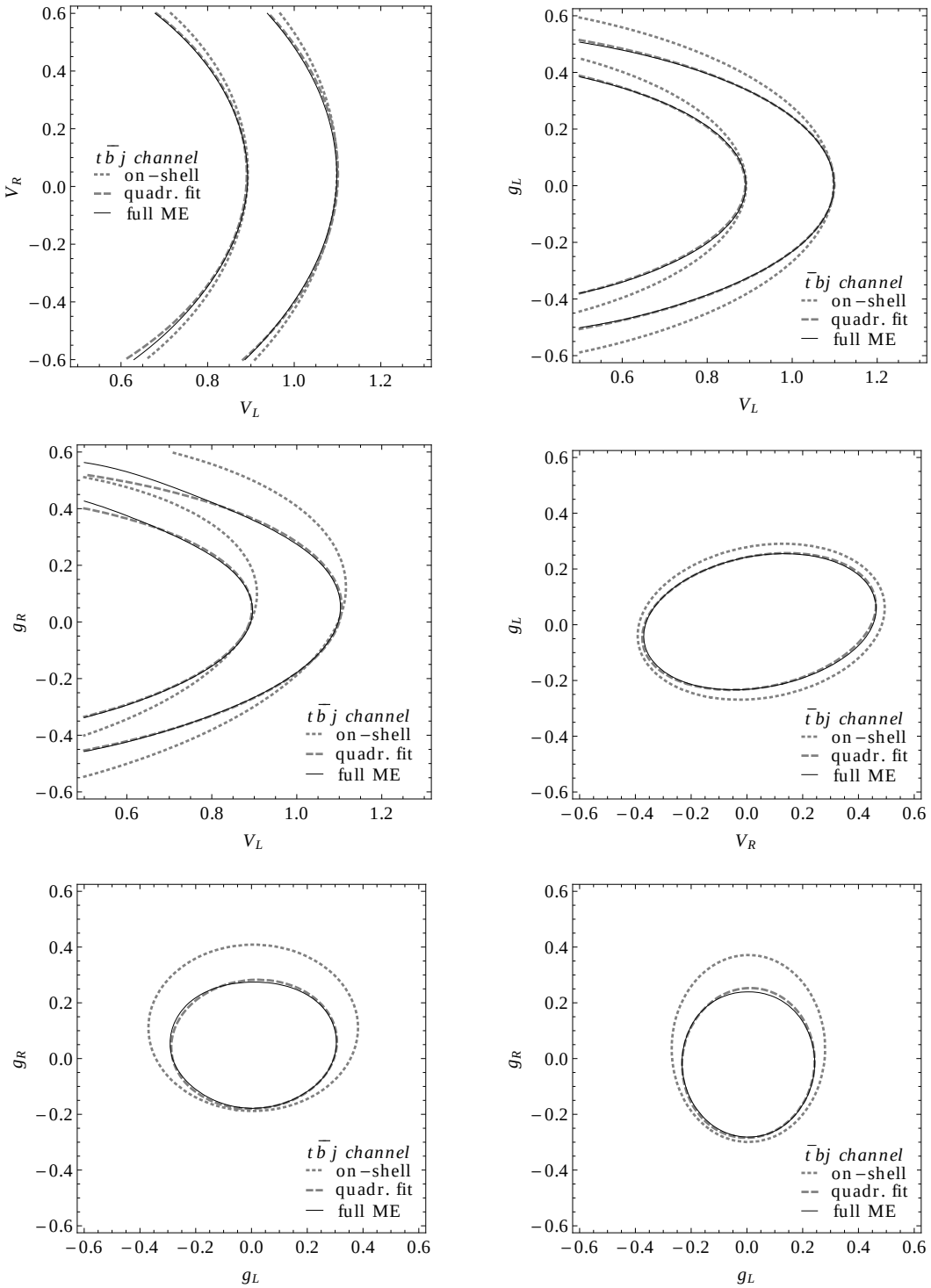

Figure 5.7.: Comparison of the 1σ contours for the various matrix element response functions κ_{on}, κ_{fit} and κ_{off} at parton level, for $t\bar{b}j$ and $\bar{t}bj$ processes in different coupling planes (setting the others to their SM values).

sensitivity contours around the SM strength $\kappa = 1$ for various anomalous coupling combinations and production processes: Especially when the momentum-dependent couplings $g_{L,R}$ are involved, there are remarkable shifts of the contours when going from the on-shell to the full ME approach, but generally these effects are modelled very well by the adapted quadratic parametrization $\kappa_{\text{fit}}(\vec{g})$, while the machine cost reduces from a 4D scan over $\vec{g}$ to a set of 1D scans along all axes g_i and interference directions $g_i g_j$ for each input process. We now go on to the detector level to quantify the impact of these different approaches on exclusion bounds on anomalous couplings from combined cross section measurements.

Detector Level

In order to obtain a detector efficiency matrix in the various approaches, samples of 500 k events are produced in each partonic production process, now explicitly merging the partonic processes tj and tbj into one process labeled "tj", cf. Sec. 4.1 for process definitions. This is done once in the full ME approach integrating over the acceptance region, Eq. (4.2), and once in the resonant ME approach integrating over the full phase space, letting the tops decay off-shell into a b quark, a charged lepton and a neutrino, analogously to [79]. All parton level samples are processed according to Sec. 4.2 to obtain events at detector level. This is done for the SM point as well as the coupling configurations

$$\begin{array}{lllll} \text{A:} & V_L = 1\,, & V_R = 0.3\,, & g_L = 0.15\,, \\ \text{B:} & V_L = 1\,, & g_R = 0.024\,, & \end{array} \tag{5.10}$$

taken from [79] to facilitate comparison. Note that in each case a consistent top width $\Gamma_t(\vec{g})$ is calculated beforehand and the result checked to comply with experimental constraints [95]. Again for comparison reasons, in Sec. 4.2.2 we have also adopted the final state selection cuts stated in [79] which define the various components of ε. By applying every final state selection to each of the 500 k event samples corresponding to the partonic input processes and averaging over lepton flavors and charge states, we find for the samples from resonant diagrams integrated over the full phase space an efficiency matrix ε (in %) at the SM point:

	tb	tj
tb sel.	0.658(6)	0.048(2)
tj sel.	0.165(3)	0.558(4) .

(5.11)

For the full ME approach, we run the selection criteria described above on the detector level samples from full matrix elements integrated over the acceptance region, inferring ε' (in %)

	tb	tj
tb sel.	1.28(1)	0.033(1)
tj sel.	0.282(4)	1.123(6)

(5.12)

at the SM point.

Before moving on to detector level coupling limits, the detector efficiency matrices can be compared between the various coupling points, Eq. (5.10), to test the

assumption of a constant detector response. While the small admixture of g_R in point B only has a negligible effect on the efficiencies, we observe that there are sizeable changes in the efficiencies when going from the SM point to point A, amounting to some 15 % (8 %) of the original values for tb (tj) selection in the samples with full phase space integration at parton level. However, when going close to the detector acceptance region already with the partonic input, this dependence is reduced to $\sim 6\,\%$ (4 %), thus improving on another source of systematic uncertainty.

Taking the approximate NNLO on-shell s and t channel production cross sections from Tab. 2.1 (multiplied by a partonic acceptance efficiency corresponding to the cuts in Eq. (4.2) in the full ME approach) to normalize the SM reference point for each input process, we now have all ingredients at hand to derive limits on $\vec{g}$ from a set of cross section measurements, and compare the results. To that end, we define a χ^2 function

$$\chi^2(\vec{g}) = \sum_i \left(\frac{\sigma_i^{\text{exp}} - \sigma_i^{\text{th}}(\vec{g})}{\Delta\sigma_i} \right)^2 , \tag{5.13}$$

where the sum runs over all final state selections and charge states, and the $\sigma_i^{\text{th}}(\vec{g})$ are modelled by Eqs. (5.5) resp. (5.6) while $\sigma_i^{\text{exp}} \equiv \sigma_i^{\text{th}}(\vec{g})|_{\text{SM}}$ (i. e. assuming experimental confirmation of the SM). The uncertainties $\Delta\sigma_i$ are the ones quoted at the beginning of Sec. 5.1.2, so that confidence regions in $\vec{g}$ are inferred by sampling the parameter space and accepting all points satisfying

$$\chi^2(\vec{g}) \leq \chi^2_{\text{min}} + \Delta\chi^2 , \tag{5.14}$$

where $\chi^2_{\text{min}} = 1$ assuming experimental confirmation of the SM, and $\Delta\chi^2$ depends on the number of couplings varied independently as well as the requested confidence level (cf. e. g. [92, Ch. 33]). It was shown [145, 146, 158, 159] that NLO corrections affect the differential distributions in s and t channel single top production only marginally[5], at the few % level, and can thus be readily accounted for by channel specific overall K factors, as in our analysis. A more comprehensive analysis including coupling dependent K factors, similar to the case of anomalous flavor changing gluon couplings [160] and extending an existing study on anomalous top decays at NLO [161], will moderately influence the numerical values of the exclusion bounds. However, our results concerning the need to include the full matrix elements and the relative importance of the quartic couplings (cf. below) remain valid.

Now turning to the resulting bounds at the detector level, as already anticipated from the 1σ contours in Fig. 5.6 and 5.7 the effects on $V_{L,R}$ remain small in general, while the largest differences are found when the momentum dependent couplings $g_{L,R}$ are involved, particularly in the g_L–g_R plane illustrated in Fig. 5.8. In this case, when single channels and charge states are considered separately, the different approaches tend to produce very different exclusion bounds. Fig. 5.8 might also suggest that after combining all channels and considering the ratio $R(\bar{t}/t)$ of cross sections for t

[5] In the t channel, this is particularly true for the tbj MEs [145, 146], which however dominate the matched process tj, as shown in Sec. 1.2.2.

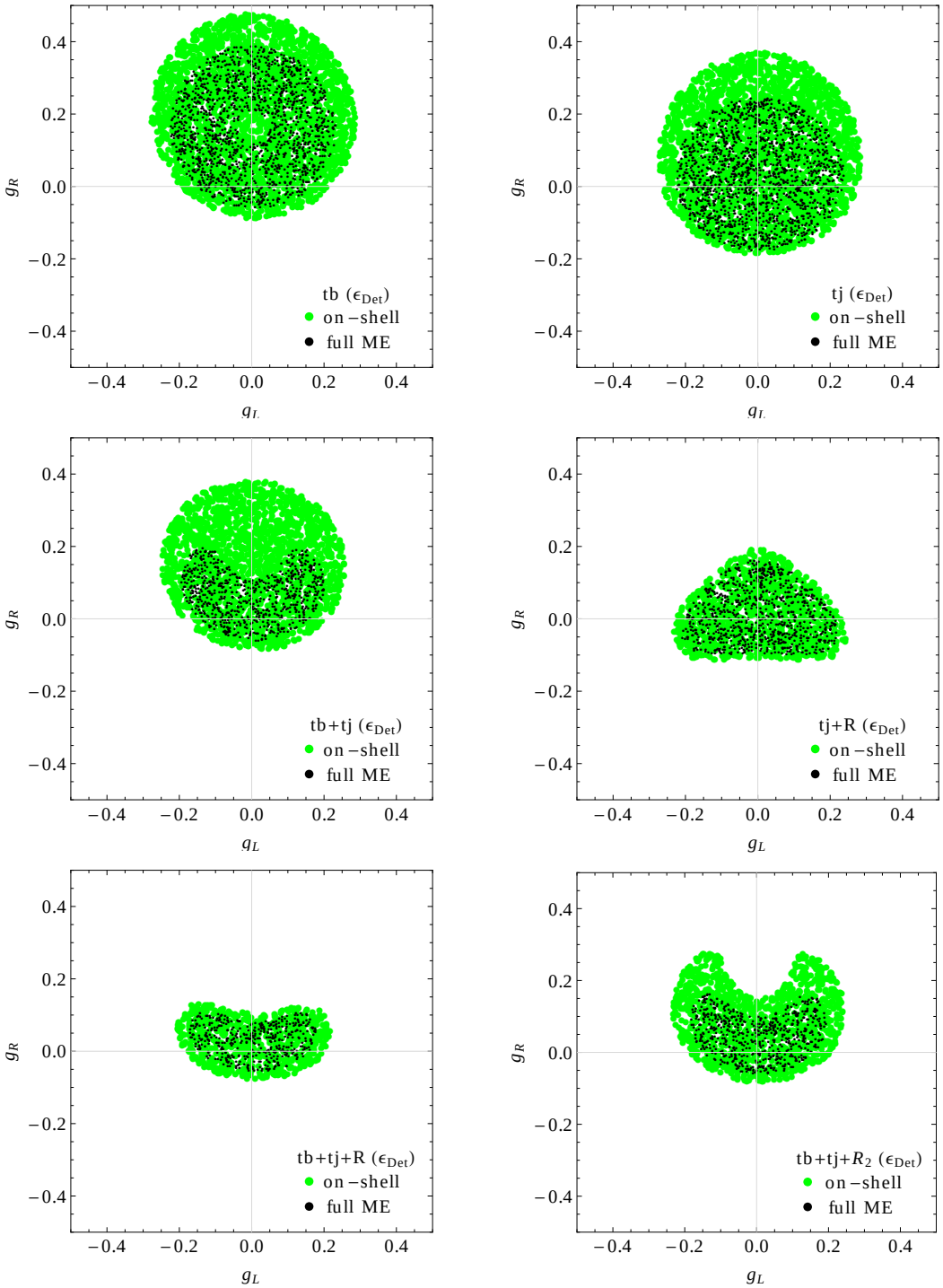

Figure 5.8.: Combined 1σ limits on g_L and g_R ($V_L = 1$, $V_R = 0$) from single final states (top), combined final states (center left), and including the observable $R(\bar{t}/t)$ (center right and bottom). "R_2" denotes a factor 2 on the experimental resolution of R.

and $\bar{t}$ production in the t channel as an additional observable (tentatively assuming 2 % statistical and 3 % systematic uncertainty as estimated for $10\,\mathrm{fb}^{-1}$ at $\sqrt{s} = 14\,\mathrm{TeV}$ in [79], in the absence of a more detailed experimental assessment), one might end up with the same exclusion limits again, but indeed this depends heavily on the total uncertainty of R in the actual experiment (cf. "R_2" in Fig. 5.8). In any case, when the aim is to properly understand and quantify the sensitivities to anomalous couplings of the various final states separately, going from the on-shell approach to full matrix element responses inside the selection acceptance region produces considerable effects that should not be neglected. In that respect, the adapted quadratic parametrization introduced above, employing quadratic fits to off-shell scans inside the acceptance region, represents a very good approximation to the full off-shell parameter scan (cf. Fig. 5.4–5.7).

5.1.3. Influence of the Off-shell Coupling

After discussing the technical issue of modelling the LO matrix element response to anomalous top couplings at an experimentally relevant acceptance level, and validating an adapted quadratic parametrization which simultaneously meets the demands of machine efficiency and good agreement with the full off-shell coupling scan in the previous section, the closing section of this study is devoted to the application of the new approach to a physical issue, namely a possible admixture of the additional anomalous coupling V_L^{off} introduced in Sec. 2.2.2, to the single top cross sections (the total top width is also included as an observable, but its sensitivity to V_L^{off} is negligible compared to the other anomalous couplings, because kinematically it is a contact interaction, cf. Sec. 2.5.2 and [48]).

Considering the experimental sensitivities to the anomalous couplings of the total cross sections stated above for the LHC (which are already dominated by systematics), it is clear that a stand-alone study of single top cross sections alone will never provide the most stringent bounds on the complete parameter space of anomalous CC couplings, including V_L^{off} or not. Therefore, rather than just adding another direction to $\vec{g}$, the focus shall be directed here to those regions of the parameter space where single top cross sections actually become the crucial inputs to the combined limits (this will be further stressed in Sec. 5.2).

More explicitly, as shown in Sec. 2.5.2 the top decay observables are very sensitive to anomalous W helicity fractions generated by V_R, g_L and g_R (cf. [78, 79, 81, 94]). For example, the limit $|g_R| \lesssim 0.024$ stated in [79] for our LHC reference point ($10\,\mathrm{fb}^{-1}$ at $14\,\mathrm{TeV}$) is more than an order of magnitude below the sensitivity of the cross sections, so we may as well set $g_R \equiv 0$ for our purposes. On the other hand, the large interference among V_R and g_L leads to rather poor bounds $|V_R| \lesssim 0.3$ resp. $|g_L| \lesssim 0.15$ as long as they are fine-tuned to $V_R \sim 2g_L$. Finally, since decay observables basically measure helicity fractions, they are neither sensitive to the overall vertex normalization nor to the admixture of any four-fermion contact interaction (such as V_L^{off}). This is where the cross sections come into play, delivering the most stringent direct constraints as will be shown in detail in Sec. 5.2. However,

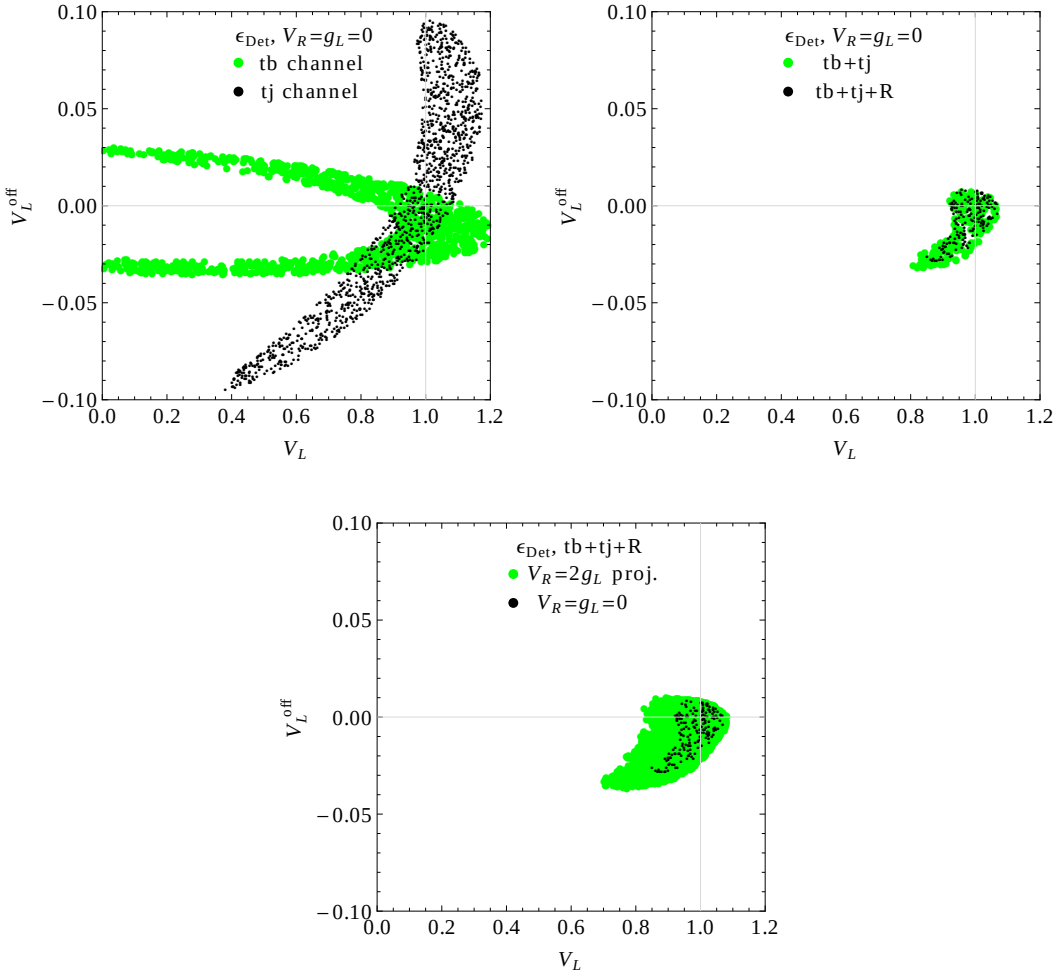

Figure 5.9.: Combined 1σ contours in the V_L–V_L^{off} plane, setting $V_R = g_L = 0$ (top) or projecting over the direction $V_R = 2g_L$ (bottom).

to conclude this study first, in Fig. 5.9[6] we therefore present combined limits from total single top cross sections on the interfering V_L and V_L^{off} (no other four-fermion interaction interferes with any of the remaining directions in $\vec{g}$, as argued in Sec. 5.2), both setting $V_R = g_L = 0$ as well as varying over $-0.3 \leq V_R = 2g_L \leq 0.3$. The very different sensitivities of the two final states greatly help in the combined limit: the s channel is very sensitive along V_L^{off} due to the kinematics, whereas the t channel basically cuts the substantial interference in the s channel along V_L. Still, the resulting limit on V_L deteriorates from $0.9 < V_L < 1.1$ ($V_L^{\text{off}} = 0$) to $0.82 < V_L < 1.1$ (V_L^{off} varied). Naturally, projecting over the remaining freedom in V_R and g_L instead of switching them off further relaxes the combined limits to $0.68 < V_L < 1.1$.

[6] Note the relative sign of V_L^{off} with respect to the plots in [55], correcting for the i^2 discussed explicitly in Sec. 3.2.2, cf. Eq. (3.12), which was originally missing in the implementation.

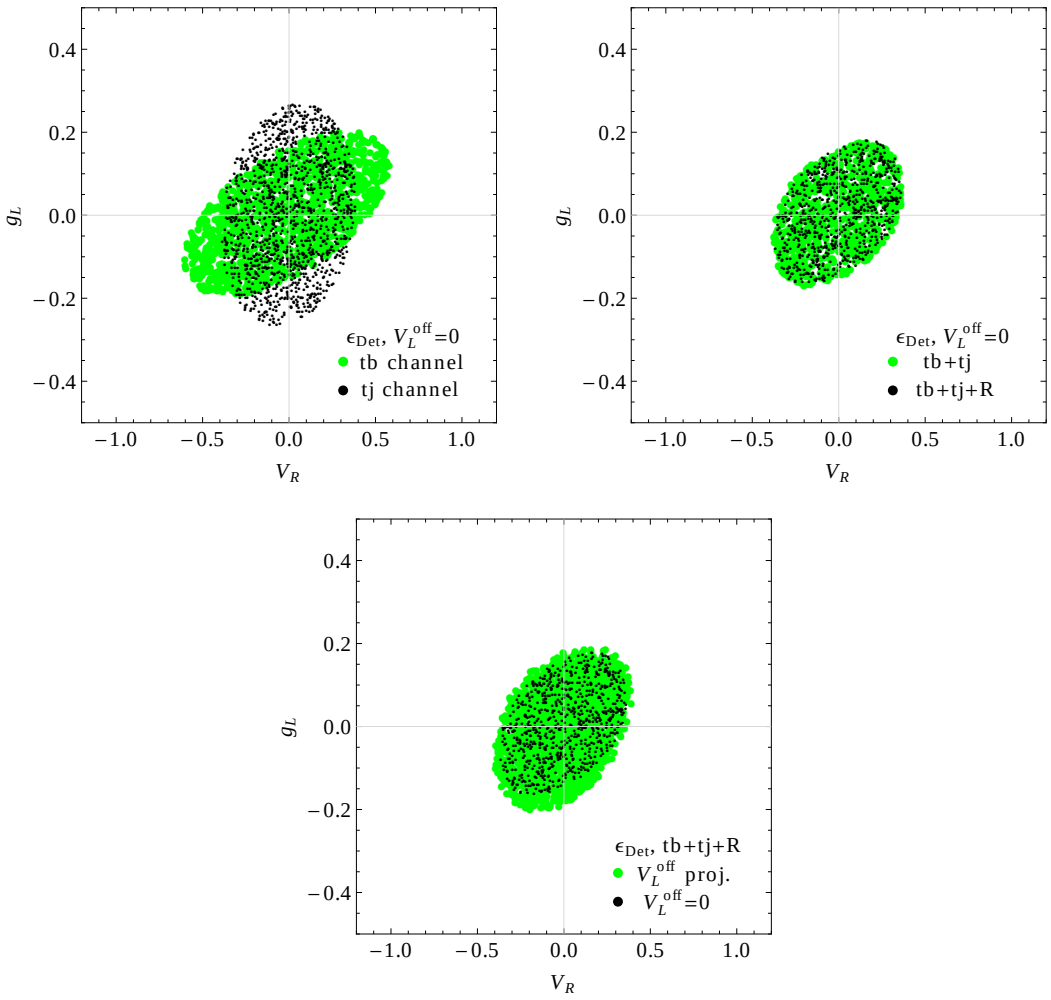

Figure 5.10.: Combined 1σ contours in the V_R–g_L plane, setting $V_L = 1$ and $V_L^{\mathrm{off}} = 0$ (top) or projecting (bottom).

Fig. 5.10 displays combined bounds in the V_R–g_L plane, switching off resp. varying over V_L^{off}.

In the long run, it is perfectly clear that this ambiguity among V_L and V_L^{off} remaining in the single top cross sections can be further resolved, namely by examining differential distributions, since V_L^{off} scales very differently with the partonic $\sqrt{s}$ than V_L due to the absent W propagator. A detailed assessment of this issue will form the main topic of the other study in this chapter presented in Sec. 5.2, also extending V_L^{off} to a more general set of contact interactions. In any case, one should remain careful when stating limits on V_L from measurements of the overall size of V_{tb} until its kinematic behaviour is further clarified experimentally.

5.2. Single Top Contact Interactions

In sections 2.5.2 and 5.1.3 it was argued that the W helicity fractions of the top decay convey a clean handle on the anomalous trilinear couplings V_R, g_L and g_R, because contact interactions are suppressed there [48]. On the other hand, single top cross sections do receive sizeable contributions from contact interactions stemming from the production insertion, cf. V_L^{off} discussed in Sec. 5.1.3 which kinematically is a contact coupling. So rather than considering single top cross sections as additional observables for the trilinear couplings, one could also employ top decay results to *fix* those beforehand[7] and then use the single top channels to cleanly constrain the four-fermion couplings: this is the idea of the study to be presented in this section. As a basis for the contact interactions we use the complete minimal set introduced in Sec. 2.3.1, so that the coupling parameter space is now spanned by

$$\vec{g} = \left\{ V_L, V_L^{\text{off}}, S_L^{(1)}, S_R^{(1)}, S_L^{(8)}, S_R^{(8)} \right\} , \tag{5.15}$$

where V_L^{off} is related to $V^{(3)}$ employed in Eq. (2.43) by (D.3). We explicitly keep the V_L^{off} normalization here rather than switching to $V^{(3)}$ in order to facilitate the comparison with the results of Sec. 5.1, whereas the scalar couplings are normalized by $\Lambda = 1\,\text{TeV}$, so any respective numerical values quoted later can be understood as being multiplied by $(\Lambda/\text{TeV})^2$. Furthermore, the SM vertex normalization V_L is kept as a direction in $\vec{g}$ because the helicity fractions are not sensitive to it, and it also interferes with V_L^{off}.

In order to assess the contact interactions, we make use of the kinematics which can be expected to be quite different from the SM because of the absence of the W propagator. Therefore, rather than considering just the total cross sections as observables, in Sec. 5.2.2 we perform a binned likelihood analysis over various distributions which are either sensitive the general admixture of contact interactions or disambiguate the various anomalous directions contained in Eq. (5.15). However, before moving on to the actual study, the next section addresses the general validity of the effective operator approach within the sensitivity reach of the contact interactions for the processes and LHC energies considered here.

5.2.1. Unitarity Considerations

As argued in some detail in Sec. 1.1.2, the tree level unitarity of the partial wave amplitudes conveys an upper limit for the typical process energies where the effective operator expansion is consistent. In principle this is true for all non-renormalizable couplings including also $g_{L,R}$, but of course the contact couplings are more critical because of the additional momentum power in the numerator. Hence it should be checked that the coupling limits derived from the study are well below the consistency bound from tree level unitarity. This is done here for the example of V_L^{off}, having verified that the scalar contact interactions are less critical in this respect. To

[7] Non-zero values would add to the reference offset of the single top cross sections and also change the spin analyzers introduced in Sec. 2.5.2, but in absence of any experimental hint towards NP in these couplings, we just use the SM values $V_R = g_{L,R} = 0$ as a reference point.

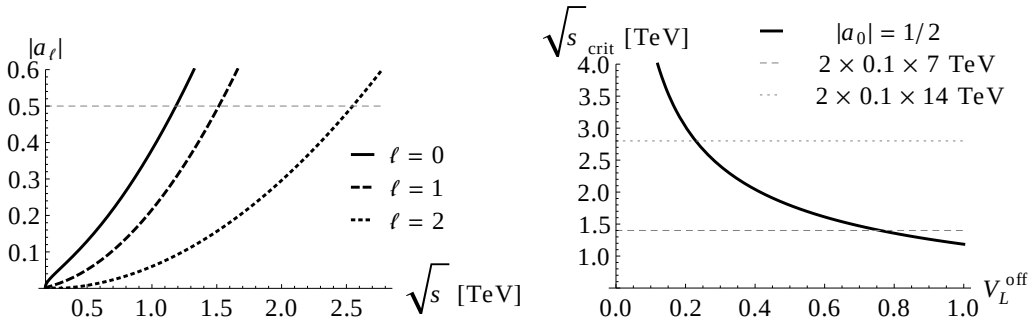

Figure 5.11.: Energy dependence of the lowest partial waves of the contact amplitude (left) and the critical c.m.s. energy corresponding to $|a_0| = 1/2$ as a function of the coupling value (right). The grey horizontal lines assume an approximate pdf cutoff corresponding to LHC collision energies $\sqrt{s} = 7\,\text{TeV}$ (dashed) and 14 TeV (dotted).

that end, the s channel contact amplitude given in Eq. (1.9) is evaluated analytically for flavors $u\bar{d} \to t\bar{b}$ as a function of the partonic c.m.s. energy $\sqrt{\hat{s}}$ and decomposed into partial wave amplitudes according to Eq. (1.11). Setting $V_L^{\text{off}} = 1$, the point where the most divergent s-wave runs into the unitarity limit (1.12), cf. left plot in Fig. 5.11, then defines a critical energy $\sqrt{s}_{\text{crit}}$ where the approach breaks down. Assuming a typical energy cutoff from the pdfs for various LHC collision energies, this can be turned into a critical coupling value which should well exceed the actual sensitivity of the experiment. As shown in the right plot of Fig. 5.11, this amounts to a consistency requirement of $|V_L^{\text{off}}| \lesssim 0.8$ (7 TeV) resp. $\lesssim 0.25$ (14 TeV), which particularly turns out to be well above the experimental reach ~ 0.05 which was found in Sec. 5.1.3 from total cross sections.[8] As the sensitivity can be generally assumed to further improve with differential observables, the effective expansion can be considered valid in all studies presented in this thesis.

5.2.2. Analysis and Results

As already mentioned, the qualitative difference of the couplings considered in Sec. 5.1 and the contact couplings is that the effect of the latter on the top decay is negligible already at the amplitude level (i. e. before phase space integration). This simplifies the parametric dependence, because the quadratic approach, Eq. (5.7a), now manifestly holds even with full matrix elements including acceptance cuts.[9] Moreover, as has also been discussed before, V_L^{off} stands out among the contact couplings as the only structure interfering with the SM piece of the amplitude, which was precisely the reason to include it also in the parameter space of Sec. 5.1. In addition, it turns out that there is no further interference direction among any of the remaining contact couplings, because generally the vectors (including the SM

[8] Conversely, the critical partonic energy corresponding to $|V_L^{\text{off}}| = 0.05$ is $\sqrt{s}_{\text{crit}} \simeq 6.4\,\text{TeV}$, well above the LHC reach for partonic collision energies even at 14 TeV.

[9] This can be easily verified by parameter scans similar to the ones performed in Sec. 5.1.2.

piece) do not interfere with any scalars, and likewise the scalar left–right interferences vanish because the chiral projectors are always inserted also in the massless fermion line in the contact diagrams, cf. Eq. (2.43). Finally, note that the scalar amplitudes $\propto S^{(1)}$ resp. $\propto S^{(8)}$ differ only in their color algebra, so the squared $2 \to 2$ production matrix elements are identical up to a global color factor. Analytically, averaging over initial and summing over final colors, this factor amounts to

$$\left(\frac{1}{3}\right)^2 \sum_{a,b} \mathrm{tr}[t_a t_b]\,\mathrm{tr}[t_a t_b] = \frac{1}{9} \cdot \frac{1}{4} \cdot \mathrm{tr}\,\mathbb{1}_{adj} = \frac{2}{9} \tag{5.16}$$

with normalized $\mathbf{SU}(3)_\mathrm{C}$ group generators t_a, cf. appendix A and e. g. [63, Sec. 17.4]. This is easily verified employing WHIZARD to calculate the ratio of respective on-shell production κ factors. It follows that the scalar directions $S^{(1)}$ and $S^{(8)}$ are kinematically degenerate because of identical differential matrix elements (up to negligible effects from the decay vertex), so in our approach based on binned distributions, one may just as well drop the color superscript and redefine Eq. (5.15) as

$$\vec{g} = \left\{V_L, V_L^\mathrm{off}, S_L, S_R\right\} \ , \tag{5.17}$$

working in the singlet-like normalization for the scalar couplings. Respective bounds can be interchanged to the octet normalization simply by multiplying the color factor, Eq. (5.16). In the end, this reduces the quadratic form to just five directions, namely four squared ones plus the V_L–V_L^off interference.

The analysis strategy is to produce parton level event samples corresponding to all these parameter directions, identify kinematic distributions which can discriminate either the contact couplings from the SM part, or several different contact couplings from each other, and perform a binned likelihood test to derive bounds on $\vec{g}$. This is done as a first step at parton level to discuss the observables and compare the sensitivities of the different production channels. In the second step, we will include detector effects accounting also for the relative admixture of the partonic processes in the final state selection. To that end, binned detector responses are inferred for s channel and t channel selection along each kinematic distribution considered in the likelihood function with $\vec{g}$ set to the SM, and multiplying all partonic histograms with it. Note that this entails leaving the spectator jet (a b quark in the s channel resp. a light quark in the t channel) untagged at parton level in order to remain inclusive for the finite b tagging performance of the detector (the point will be taken up in more detail in the detector level discussion).

Technical Setup

To meet the ends of the study to be performed here, one first has to adapt the partonic phase space cuts with respect to the ones quoted in Eq. (4.2) for the previous study. Specifically, the altered kinematics of the contact diagrams, which is expected to be more central compared to the SM especially in the t channel because of the absent propagator, is accounted for by tightening the η cut for all jets in (4.2b)

to $|\eta(j,b)| < 3$. In addition, to enhance the sensitivity to the high energy tail we introduce a cut on the total invariant mass of the final state

$$m_{tj} \equiv \sqrt{s} > 400\,\text{GeV}\ , \tag{5.18}$$

where m_{tj} is the invariant mass of the reconstructed top momentum and the hardest spectator jet. The final state selections stated at the end of Sec. 4.2.2 are adjusted correspondingly by globally adding a respective $\sqrt{s}$ requirement and additionally relaxing the forward cut on the tagging jet in the t channel to $0 \leq |\eta(j)| < 3$.[10] All these adjustments considerably reduce the SM cross section, which should however be considered as background to this study. With the stated acceptance cuts, WHIZARD is employed to produce samples with 10^6 events per production channel and charge state for each NP direction resp. 2×10^6 events per lepton flavor ($\ell = e, \mu$) and charge for the SM part (statistics is increased for the SM samples because they form the basis for the detector response discussed later on). The squared NP directions are produced by setting only one of the couplings in Eq. (5.17) to unit at the top production vertex while keeping the dominant SM contribution to the decay. The remaining interference direction is obtained from an additional sample where both V_L and V_L^{off} are set to unit. From these samples, we then infer normalized differential matrix element shapes as well as overall normalizations with respect to the SM point along each NP direction (the analogs of the on-shell κ coefficients in the previous section).

For the binned likelihood test, we extend the χ^2 function introduced in Eq. (5.13) by

$$\chi^2(\vec{g}) = \sum_i \left(\frac{w_i^{\text{exp}} - w_i^{\text{th}}(\vec{g})}{\delta_i} \right)^2 \tag{5.19}$$

with the sum running over all bins of all normalized histograms included in the likelihood test. The uncertainty δ_i of each bin weight is

$$\delta_i = \sqrt{\frac{1}{N}\left(w_i + w_i^2\right) + \delta_{\text{sys}}^2\, w_i^2}\ , \tag{5.20}$$

with the total number of events in a given final state selection $N = \int L \cdot \sigma_{\text{tot}}$ taken at $\int L = 100\,\text{fb}^{-1}$, and a tentative systematic error assumed to be $\delta_{\text{sys}} = 3\,\%$ as was done before in Sec. 5.1.2 for normalized observables. The higher order dependence of the statistical error on w_i in Eq. (5.20) simply comes from the fact that we are considering normalized bin weights rather than absolute entries in order to reduce the systematic uncertainty. The sample sizes stated above are chosen such that the MC statistics is at least ten times the expected N_{exp}, while the binning is adjusted such that each bin contains at least $\mathcal{O}(10)$ events at the SM point so that the Poisson statistics is

[10] This increases the sensitivity to the NP contributions in the t channel with respect to the SM single top contribution, but in a more involved study addressing the reducible backgrounds in more detail, it must be checked to what extent the forward tagging can be relaxed without spoiling the single top signal altogether.

well approximated by the Gaussian assumed in the χ^2 function.[11] 1σ limits on the couplings are then inferred as in Sec. 5.1.2 by scanning the parameter space and accepting all points satisfying Eq. (5.14).

Partonic Level

At parton level, it is at first interesting to examine the sensitivities of each production channel to the various couplings. To that end, we examine various kinematic distributions of the final state objects. Specifically, apart from the missing transverse energy $\not{E}_T$ we consider transverse momentum (p_T) and pseudorapidity (η) distributions of the objects in the final state selection, namely the b jet and the charged lepton ℓ reconstructing the top momentum, as well as the hardest spectator jet (j) in the event. In addition, we include the total event energy $\sqrt{s} = m_{tj}$, but also the top spin analyzer angle $\cos\theta_\ell$ defined in Eq. (2.56) in order to become sensitive to the top production polarization. As shown in Fig. 5.12 for the s channel resp. Fig. 5.13 for the t channel, there are many distributions (most prominently $\sqrt{s}$ and $p_T(j)$, but also $|\eta(j)|$) which are very sensitive to anomalous contact contributions in general but mostly blind to their relative admixture. The former is no surprise given the very different energy scaling of the contact terms with respect to the SM piece. However, the spin analyzer $\cos\theta_\ell$ but also $p_T(\ell)$ indeed turn out to be discriminative observables in both channels for an anomalous right-handed top production mode, as parametrized here by S_R. On the other hand, it should be much harder to tell the anomalous left-handed couplings V_L^{off} and S_L apart from normalized matrix element shapes only, with the most promising observables being the pseudorapidity distributions $|\eta(b)|$ and $|\eta(j)|$ in both channels. As a side remark, note that the $|\eta(j)|$ histogram in Fig. 5.13 justifies the relaxed forward tagging of the spectator jet in the t channel introduced before, as restricting to the SM-like forward phase space $|\eta| \gtrsim 2.5$ would indeed kill most of the signal one is looking for.

Finally, in Fig. 5.14 we compare the 1σ contours in the two different production channels at parton level, finding that the s channel generally is much more sensitive to the contact couplings than the t channel. This could be expected from the fact that the s channel is maximally sensitive to the high energy tails of the contact interactions, which is particularly evident in the S_L–S_R plane. The fact that the s channel sensitivity to the scalars supersedes the t channel one by roughly an order of magnitude is not only due to more sensitive shapes, but also due to the much larger overall sizes of the matrix elements (i. e. κ factors), a feature which is not displayed in the normalized shapes of Fig. 5.14. Note that the different relative sensitivities in the two channels when comparing the scalar plane to the vector plane can in principle be used to distinguish V_L^{off} from the scalar couplings by a separate analysis of each individual channel. However, the detector level analysis below will address the question whether they can be separated at all with a sufficient purity. Moreover,

[11] This criterion is not always strictly fulfilled, particularly in the small s channel, but it was checked that the results obtained are stable against rebinnings and also against replacement of Eq. (5.19) by the full Poisson statistics. Hence we stick to the χ^2 method for simplicity, and consistency with Sec. 5.1.

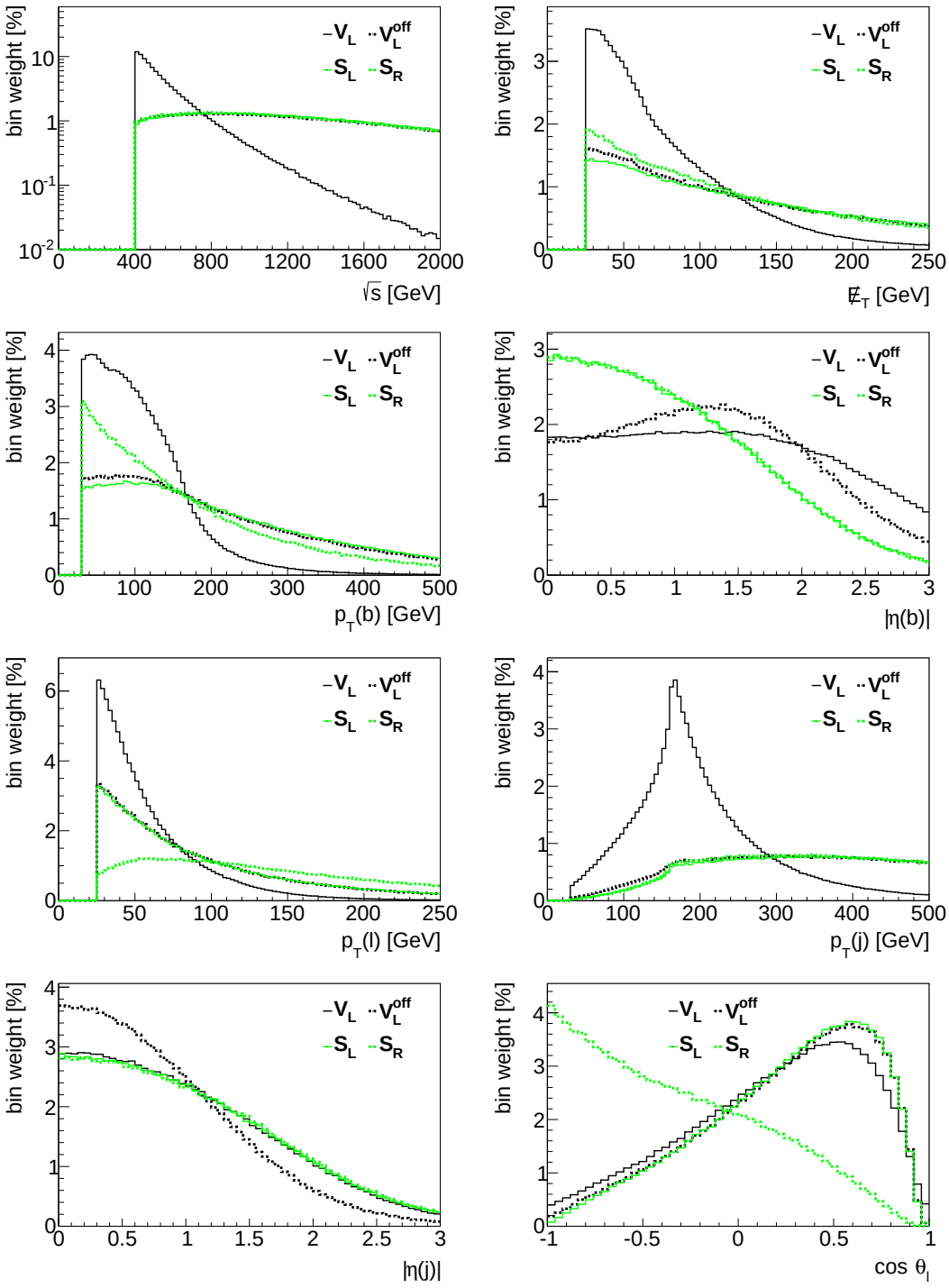

Figure 5.12.: Normalized s channel distributions at parton level.

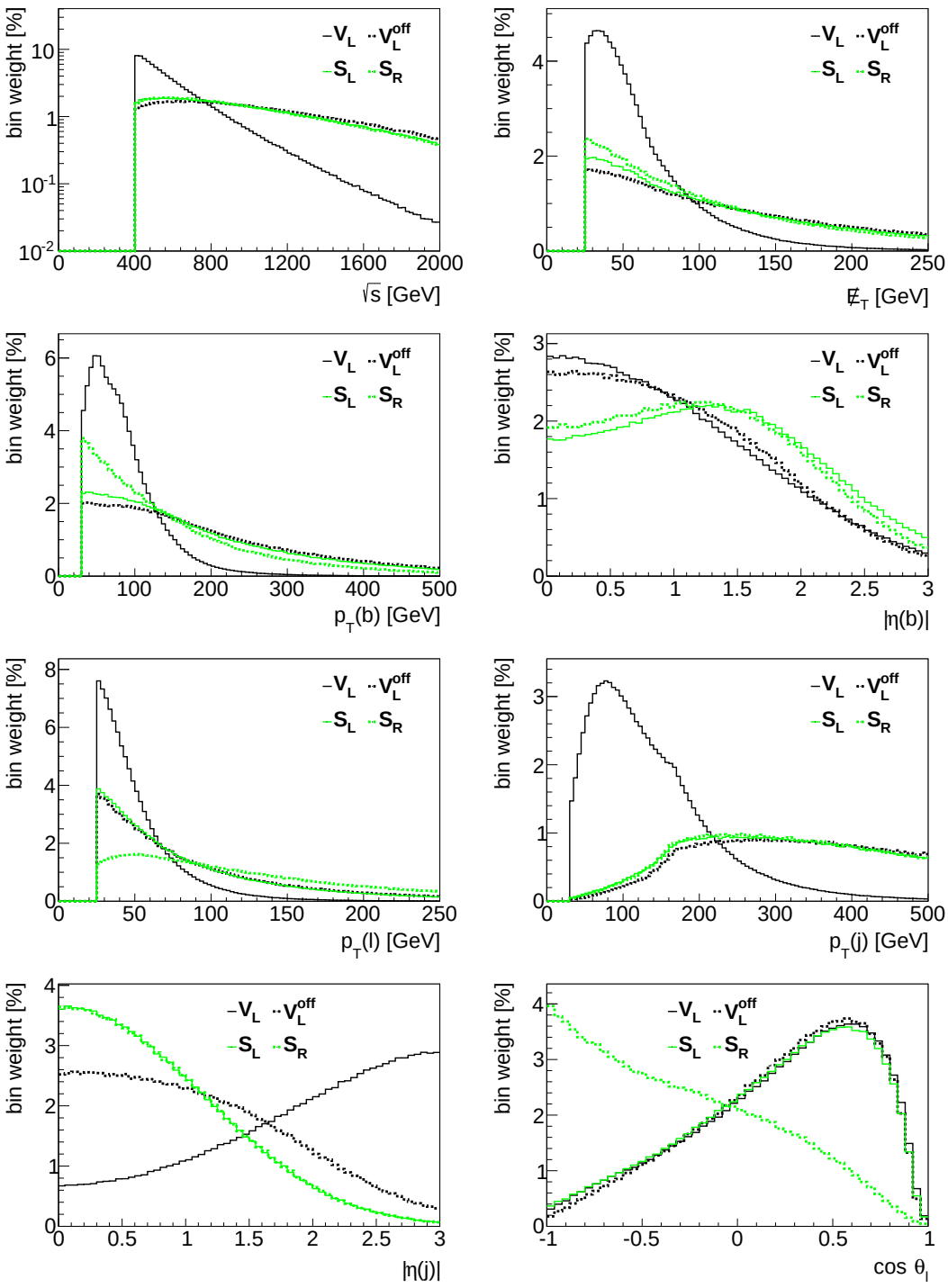

Figure 5.13.: Normalized t channel distributions at parton level.

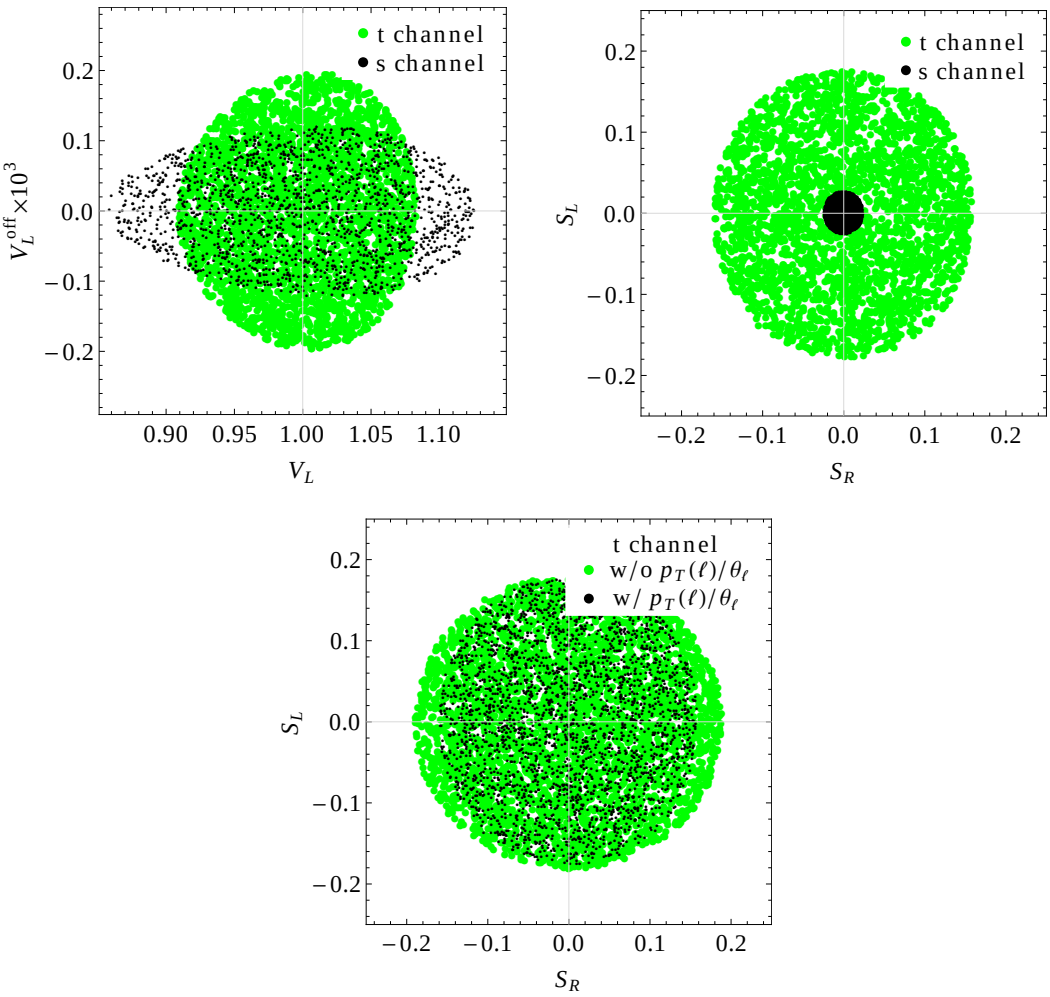

Figure 5.14.: Channel specific coupling sensitivities (top) and effect of the S_R sensitive observables $p_T(\ell)$ and $\cos\theta_\ell$ in the t channel (bottom) at parton level.

if one compares the sensitivity to V_L with the one obtained in Sec. 5.1.2, there is obviously no significant gain from the binned analysis: this is actually a consistency requirement, since V_L only sets the overall normalization of the SM shapes but does not distort them, while on the other hand, the sensitivity to V_L^{off} increases by more than two orders of magnitude. Finally, as also illustrated in Fig. 5.14, the observables $p_T(\ell)$ and $\cos\theta_\ell$ are indeed specifically sensitive to S_R, potentially amounting to a $\sim 20\,\%$ gain on the S_R limit with respect to the S_L one, and could hence be employed to distinguish any anomalous right-handed part in single top production. To conclude this paragraph, one may state that the LHC sensitivity reach to the four-fermion interactions vitally depends on the capability to cleanly separate the s channel signal at the detector level, a task that shall be addressed

now in more detail.

Detector Level

Detector effects are being accounted for by processing the SM samples with PYTHIA and DELPHES, as described in Sec. 4.2, to obtain detector level samples. On these samples the adapted final state selections stated above for the s and t channel are then applied before filling the histograms of the kinematic observables introduced at parton level in Fig. 5.12 and 5.13. All histograms are then rebinned appropriately, so that the efficiency matrix is given by the ratio of detector level events over the partonic ones, for each bin included in the analysis. However, there remains a subtlety in the approach: b tagging should be part of the detector response, so in a strict sense one cannot use flavor information at parton level. On the other hand, the spectator kinematics (a b jet in the s channel resp. a light jet in the t channel) is a vital property of the final states, so it should be accounted for in the analysis, including off-diagonal elements of the detector response. This is resolved by leaving the spectator jet untagged in both channels *after* the final state selection (i. e. demanding only one or exactly two b jets in the t resp. s channel). The spectator, globally denoted "j", is then simply identified in both selections as the hardest jet remaining in the event after the b tagged one reconstructing the top momentum has been removed.

The outcome of the procedure is displayed in Fig. 5.15 for some characteristic observables in each final state, showing the binned detector efficiencies in percent as well as resulting absolute event counts at detector level, normalized to the reference luminosity $\int L = 100\,\text{fb}^{-1}$. Fig. 5.15 illustrates how the s channel selection efficiently suppresses the t channel sample, whereas the t channel selection is less restrictive against an s channel admixture. However, this high s channel purity is mandatory because the total cross sections deviate by more than an order of magnitude in the two production channels, so that the s channel still suffers from sizeable t channel pollution, as reflected in the total event numbers resolved by partonic sample input. On the other hand, for the same reason the t channel selection is indeed very clean, despite the fact that the efficiencies of the partonic input samples only deviate roughly by a factor of two. In the last bin of the $|\eta(j)|$ spectator histogram, the tj selection efficiencies even become identical on both inputs, which is actually a consistency requirement: since b tagging does not work any more above $|\eta| \gtrsim 2.5$, the hard b in the s channel mimics the hard light jet in the t channel and hence passes the respective selection criteria with almost the same efficiency as an original partonic tj event.

Having thus set up the machinery, let us now turn to the actual study of NP effects from the contact interactions on the final states. It is at first instructive to keep the binned likelihood analysis switched off for another moment and just repeat the total cross section analysis performed in Sec. 5.1 in the V_L–V_L^{off} plane, based now on the adapted final state selections. The result is displayed in Fig. 5.16, which should be compared with the reference Fig. 5.9 in the previous section. Consistently, the two final states show the same qualitative interference behavior in both setups,

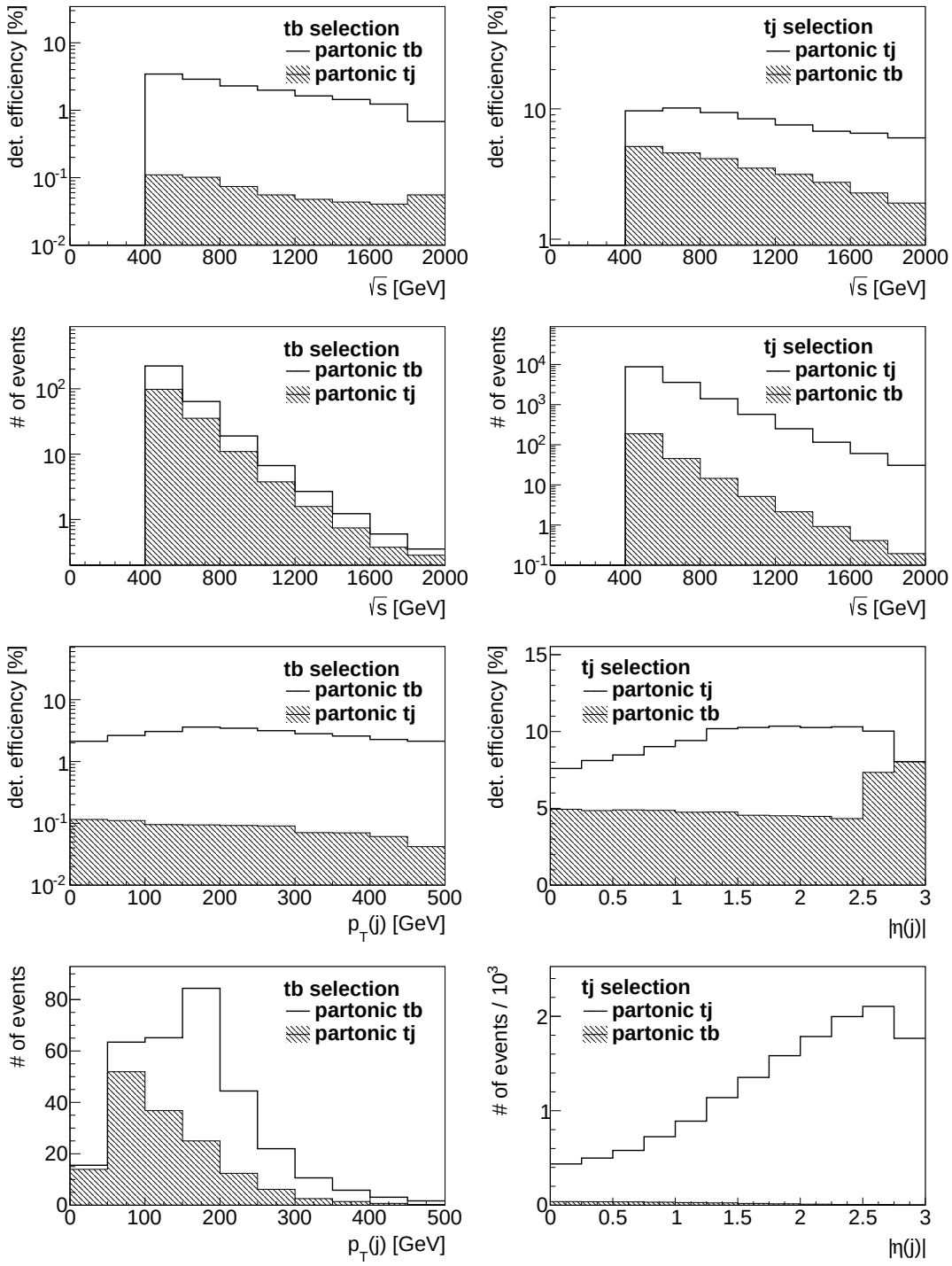

Figure 5.15.: Detector efficiencies resp. background suppression and resulting binned event numbers corresponding to $\int L = 100\,\mathrm{fb}^{-1}$ at detector level (tb sel. left, tj sel. right) for various kinematic distributions.

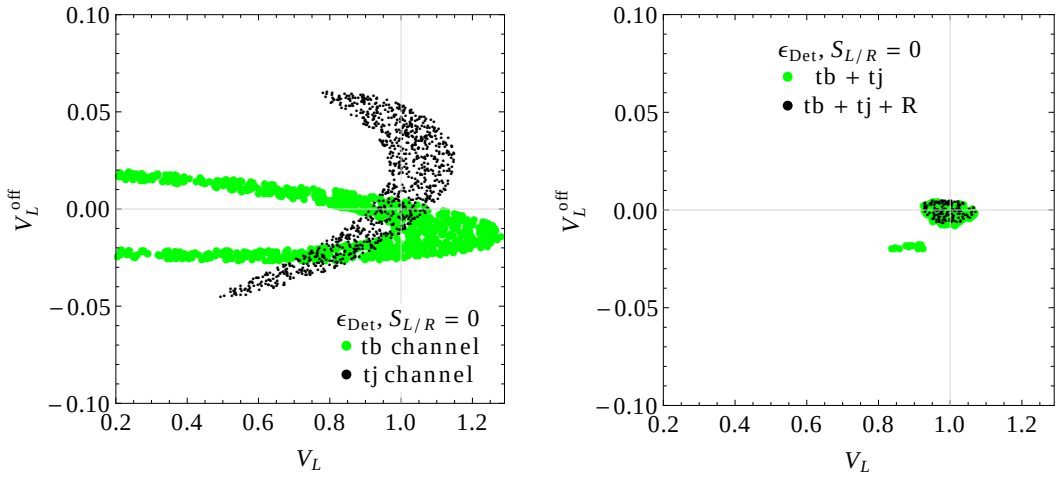

Figure 5.16.: Combined limits on V_L and V_L^{off} derived from total cross sections in the adapted final state selections, resolved by channels (left) and the channel combination illustrating the effect of R (right).

while the minor quantitative differences (slightly altered curves of the interference "bananas") stem from the adapted final state selection, resulting in shifted relative sensitivities to V_L^{off} and V_L contributions: the former is increased while the latter gets poorer, simply because the SM shape is considered as background and reduced by the selection in this study. Correspondingly, after combining the channels the 1σ bounds in Fig. 5.16 on V_L^{off} get stricter while the V_L bounds are a little looser than in Fig. 5.9.

Going on now to the results based on the binned likelihood test which are summarized in Fig. 5.17, let us first compare the 1σ bounds resolved by final state selections displayed in the top row with the ones on partonic level (top row in Fig. 5.14). It is no surprise that generally the limits tend to get worse at detector level, especially in the s channel which gets considerably diluted by t channel events. However, in the scalar plane (right column in Fig. 5.17) one observes the superficially counter-intuitive result that the t channel sensitivity *increases* at the detector level, but actually this can also be explained by the selection impurity, however tiny in the t channel at the SM point. Once the scalar NP couplings are turned on, the s channel events also significantly populate the t channel bins at detector level, due to the fact that the respective κ factors differ by orders of magnitude, as already pointed out in the parton level discussion above. A simple cross-check is given by switching off the s channel partonic input to the t channel selection, as was done in the center right plot in Fig. 5.17, highlighting that the t channel sensitivity to the scalar couplings is indeed governed by the s channel admixture. It follows that the best limits on the scalar couplings are entirely inferred from the s channel alone, numerically amounting to $|S_L| \lesssim 0.08$ resp. $|S_R| \lesssim 0.06$ in this study (varying both couplings independently), where the enhanced sensitivity to the right-handed part is again

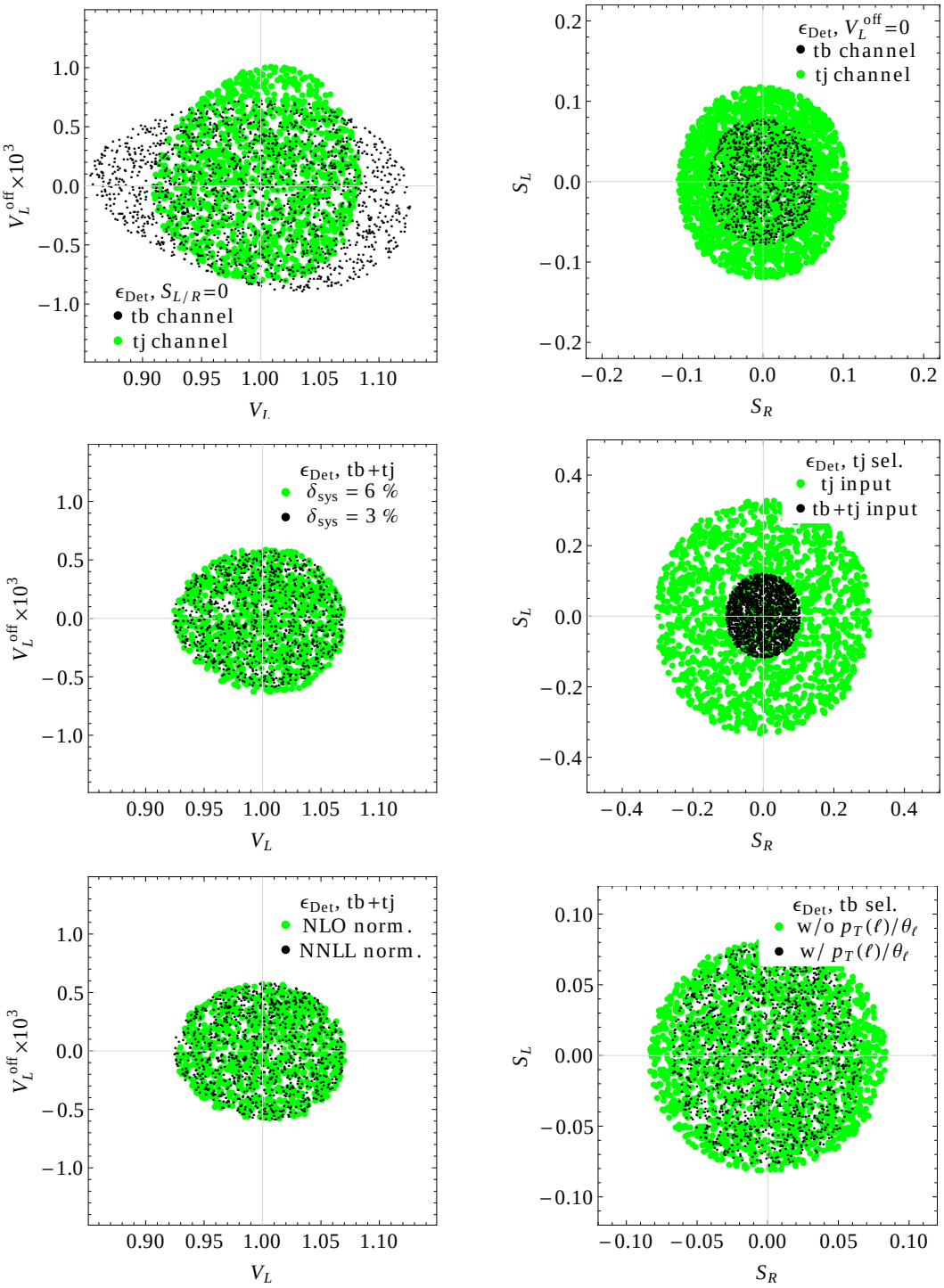

Figure 5.17.: Combined 1σ limits at detector level in the V_L–V_L^{off} plane (left) and the S_L–S_R plane (right), always setting the other couplings to their SM values. Comparison of the final state selections (top) and additional features (center and bottom, see text).

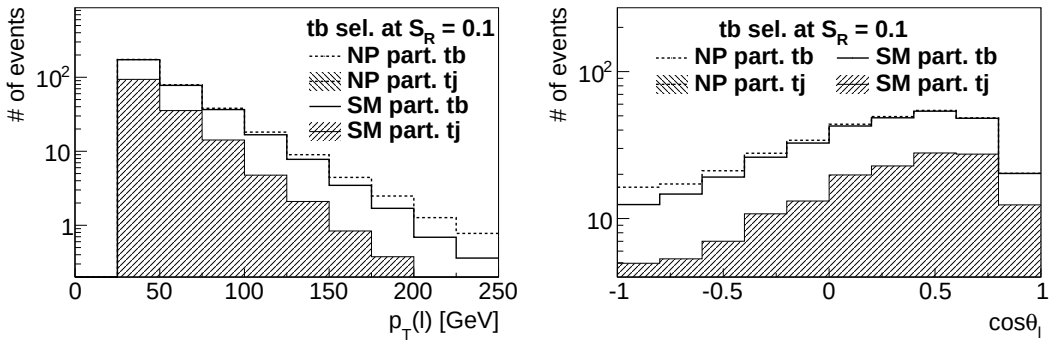

Figure 5.18.: Detector level histograms of $p_T(\ell)$ (left) and $\cos\theta_\ell$ (right) after s channel selection at the reference point $S_R = 0.1$ (event numbers normalized to $\int L = 100\,\mathrm{fb}^{-1}$).

due to the discriminative observables $p_T(\ell)$ and $\cos\theta_\ell$ that were already discussed at parton level. For illustration, Fig. 5.18 shows the effect of an NP contribution corresponding to $S_R = 0.1$ which is allowed at the 2σ level in our analysis, to the sensitive kinematic distributions $p_T(\ell)$ and $\cos\theta_\ell$ in the s channel selection.

In the vector plane (left column of Fig. 5.17), the relative matrix element sizes of the two channels do not deviate that much, so that the sensitivities generally drop at detector level. Varying only the vector couplings independently, the best limits are obtained by a combination of both channels, numerically resulting in $0.93 \lesssim V_L \lesssim 1.07$ and $|V_L^{\mathrm{off}}| \lesssim 5 \times 10^{-4}$, i. e. almost exactly two orders of magnitude better than the result of Sec. 5.1.3. Fig. 5.17 also displays some more consistency checks that have been carried out, namely doubling the systematic error δ_{sys} (center left) and changing the SM normalization from NNLL to NLO (bottom left), finding in both cases only negligible effects on the coupling limits.[12] Finally, comparing once more the top rows of Fig. 5.14 and Fig. 5.17 with special attention to the relative sensitivities resolved by final state, it must be stated that the vector versus scalar disambiguation proposed in the partonic discussion by a separate analysis of both channels might fail at detector level due to the final state selection impurity. On the basis of the basic detector study performed here, the most important ingredient in this respect seems to be the b tagging purity, which should certainly be optimized for this kind of analysis in a more involved detector study.

To conclude this section, one may state that the binned likelihood analysis is well suited to assess and exclude any anomalous contribution from contact interactions to the charged-current vertex normalization with high precision. Particularly, the interference in the V_L–V_L^{off} plane which caused the bounds to leak out to negative V_L^{off} resp. small V_L values still allowed by the total cross section analysis of Sec. 5.1.3 is cleanly cut away here. Moreover, the scalar sector has the interesting feature

[12] The latter test is nontrivial because as already mentioned in Sec. 5.1.2 the K factors, though assumed global in the kinematic sense, are channel specific and hence potentially influence the mutual signal pollution at detector level.

that the sensitivity reach is completely dominated by the s channel, so that the resulting limits are directly connected to the performance of single top s channel measurements at the LHC experiments. Finally, the different behavior of the two production channels to anomalous scalar and vector contact couplings also delivers the key to the disambiguation of V_L^{off} and $S_{L/R}$, depending again on the experimental performance to cleanly discriminate the channels. Therefore, including the chirality sensitive observables $p_T(\ell)$ and $\cos\theta_\ell$, a binned analysis of single top production could assess not only anomalous charged-current contact interactions with respect to the SM normalization V_L, but also discriminate the various types of possible Lorentz structures, if the two different final states are sufficiently under control in the LHC experiments.

Conclusions

In this thesis, we have revisited the model-independent parametrization of anomalous top couplings to SM gauge bosons within the effective operator approach, paying special attention to the charged-current (CC) sector and its phenomenological implications at the LHC. Existing trilinear coupling parametrizations were extended by a minimal general set of anomalous CC four-fermion interactions in the minimal flavor violation scheme. In addition, all anomalous trilinear and quartic top couplings in the effective operator approach were implemented into the the parton level Monte Carlo generator WHIZARD. It thus represents a powerful tool for anomalous top studies in general, also because we have added the facility to perform on the fly the matching of matrix elements containing b flavor in the initial state as e. g. required in the single top t channel. However, first addressing the minimal fully general set of anomalous trilinear tbW couplings coming from dimension six effective operators, there is still a controversy regarding the meaning of "fully general", namely whether an off-shell interaction contained in the original operator basis can be dropped for reasons of simplicity, because it turns out to be related to four fermion contact interactions after application of the equations of motion. While dropping it and sticking to the usual coupling basis (V_L, V_R, g_L, g_R) naturally simplifies the analysis, there are strong arguments to include it: Since the choice of a minimal operator basis is not unique due to the equations of motion, the respective coupling size V_L^{off} can be related to V_L by the same underlying operator coefficient. Furthermore, the coupling basis $(V_L, V_R, g_L, g_R, V_L^{\text{off}})$ parametrizes the complete set of anomalous diagrams which interfere with the SM diagram in a minimal way, so including it is consistent at the level of the objects which are measured in the end, namely physical matrix elements.

The phenomenological part comprises two studies, where in the first one the dependence of total single top cross sections on anomalous tbW couplings in s and t channel production is examined. We pay special attention to the fact that the couplings do not only affect the total cross sections but also final state distributions, which determine the selection efficiencies within the detector acceptance region. Usually these effects are considered small, thus justifying to work with constant detector efficiencies and model the whole coupling dependence on the basis of on-shell top production amplitudes. In contrast, we have gone beyond the on-shell approach and used the WHIZARD machinery to scan the full off-shell matrix element dependence on all couplings including V_L^{off} inside the acceptance window defined by the final state selection cuts. Comparing to the on-shell approach, one finds considerable deviations in many regions of the parameter space, especially where the momentum-dependent couplings $g_{L,R}$ and V_L^{off} are involved. This affects the sensitivities of the various production channels to those couplings and therefore also the limits derived

from the experiment. Finally, an adapted polynomial approach is discussed, which is based on quadratic fits to the full off-shell matrix element response including detector acceptance, and turns out to parametrize the full scan rather well while still being fast and efficient. In summary, there are tow main results of this study: firstly, that going beyond the on-shell parametrization and adapting the theoretical modelling of the coupling dependence as closely as possible to a given experimental analysis improves the sensitivity and at the same time minimizes the systematic uncertainty of the derived limits; secondly, that dropping V_L^{off} ignores interference effects and thus overestimates the sensitivity to V_L.

The second study attends to the regions of the parameter space where single top cross sections actually provide the crucial input to the overall bounds, especially the contribution of contact interactions to the tbW vertex normalization. In this respect, we address the impact of including anomalous four-fermion terms in the coupling basis, and point out the possibilities to assess their size and specifically resolve the remaining ambiguity between the interfering V_L and V_L^{off} couplings experimentally. The strategy is to employ a binned likelihood test over a set of sensitive kinematic observables, thus exploiting the different kinematic behavior of the four-fermion interactions. In this context, we have first discussed the minimal set of independent contact interactions originally consisting of six couplings emerging from dimension six operators. However, it is then argued that there are scalar operators in different color representations leading to kinematically degenerate coupling directions, so that the parameter space for this study is reduced to two scalar couplings $S_{L,R}$ in addition to the vector coupling V_L^{off}, while V_L is kept also because of the V_L–V_L^{off} interference. Detector effects have been taken into account for each bin, including off-diagonal elements among the s and t channel from selection impurity. It turns out that this mutual signal pollution is crucial for the quality of the resulting bounds, because particularly in the scalar directions the s channel sensitivity exceeds the t channel one by orders of magnitude, with the immediate consequence that any gain in the s channel signal purity is directly reflected in improved limits on the scalars, which poses an interesting challenge to the LHC experiments for the next high luminosity run. Finally, numerical bounds were obtained from the analysis normalized to $\int L = 100\,\text{fb}^{-1}$ at 14 TeV, illustrating the excellent sensitivity reach to such charged-current contact interactions in single top production. Particularly, in this analysis the contact couplings including V_L^{off} can be definitely discriminated from an anomalous V_L normalization. In terms of disambiguating the various contact couplings in the case that a deviation from the SM should become significant, two differential observables are identified which are sensitive to anomalous right-handed top production, namely the charged lepton momentum $p_T(\ell)$ as well as the spin analyzer angle $\cos\theta_\ell$, which becomes a clean window to right-handed top production once the values of the spin analyzers are fixed with respect to the trilinear couplings from W helicity fractions. On the other hand, scalar and vector contributions can be told apart by exploiting the different separate sensitivities in the two production channels, if the experimental signal purities permit it.

A. Notation and Sign Conventions in Gauge Theories

In Yang-Mills theories such as the SM, the fundamental interactions of matter, which comes in the form of fermions Ψ with half-integer spin, are described by local gauge symmetries imposed on the theory. Hence a generic Lagrangian may be written

$$\mathcal{L} = \mathcal{L}_{\text{matter}} + \mathcal{L}_{\text{gauge}} \,. \tag{A.1}$$

In the non-interacting case, $\mathcal{L}_{\text{matter}}$ is just the Lagrangian of the Dirac equation describing the free propagation of fermions,

$$\mathcal{L}_{\text{Dirac}} = \overline{\Psi}\left(\mathrm{i}\partial\!\!\!/ - m\right)\Psi \tag{A.2}$$

with fermion mass m and $\partial\!\!\!/ \equiv \gamma^\mu\partial_\mu$ the contraction of the 4-derivative with the Dirac matrices γ^μ. However, in the interacting case $\mathcal{L}_{\text{matter}}$ must by construction be invariant under local transformations of the postulated gauge symmetry group G, e. g. one of the special unitary Lie groups $\mathbf{SU}(N)$. Then the matter part of Eq. (A.1) reads

$$\mathcal{L}_{\text{matter}} = \overline{\Psi}\left(\mathrm{i}D\!\!\!/ - m\right)\Psi \tag{A.3}$$

introducing the covariant derivative

$$D_\mu = \partial_\mu - \mathrm{i}\,gA_\mu \,. \tag{A.4}$$

g denotes the coupling constant of the gauge group and A_μ is the gauge field of the symmetry group, which must come in the right representation of G to act on the Ψ living themselves in a particular representation of G. For instance, in the SM the matter fields are always in fundamental N-plets (if not singlets) under the various gauge groups, so that the gauge fields must be in the adjoint representation for which the infinitesimal group generators t^a form a basis: $A_\mu \equiv A_\mu^a t^a$ with $a = 1\cdots d(G) = 2N-1$ and a corresponding generator algebra

$$[t_a, t_b] = \mathrm{i}f_{abc}t_c \tag{A.5}$$

defining the structure constants f_{abc}. In this form $\mathcal{L}_{\text{matter}}$, Eq. (A.3), is manifestly invariant under infinitesimal local transformations

$$\delta\Psi = \mathrm{i}\,g\alpha^a(x)t^a\Psi \,, \qquad \delta A_\mu^a = \frac{1}{g}\partial_\mu\alpha^a(x) - gf^{abc}A_\mu^b\alpha^c(x) \,, \tag{A.6}$$

because $D_\mu\Psi$ by construction transforms just like Ψ itself. From Eqs. (A.3) and (A.4), one can see that in the interacting case $\mathcal{L}_{\text{matter}}$ decomposes into

$$\mathcal{L}_{\text{matter}} = \mathcal{L}_{\text{Dirac}} + \mathcal{L}_{\text{int}} \tag{A.7a}$$

$$\equiv \mathcal{L}_{\text{Dirac}} + gA_\mu^a J^{a\mu} \,, \tag{A.7b}$$

where the gauge field components couple to vector currents given by

$$J^{a\mu} = \overline{\Psi}\gamma^{\mu}t^{a}\Psi \ , \tag{A.8}$$

which are indeed the conserved Noether currents associated with the postulated gauge symmetry, $\partial_{\mu}J^{a\mu} \equiv 0$.

Turning to $\mathcal{L}_{\text{gauge}}$, after defining the field strength tensor

$$A_{\mu\nu} = \frac{1}{\mathrm{i}g}[D_{\mu}, D_{\nu}] = \partial_{\mu}A_{\nu} - \partial_{\nu}A_{\mu} - \mathrm{i}g[A_{\mu}, A_{\nu}] \ , \tag{A.9}$$

it is easily verified that an invariant expression is given by

$$\mathcal{L}_{\text{gauge}} = -\frac{1}{2}\mathrm{tr}[A_{\mu\nu}A^{\mu\nu}] = -\frac{1}{4}A^{a}_{\mu\nu}A^{a\mu\nu} \tag{A.10}$$

with the trace taken over the fundamental group indices, so that the generators are orthonormal, $\mathrm{tr}[t_a t_b] = \frac{1}{2}\delta_{ab}$. Eq. (A.10) contains the kinetic part of the gauge field as well as trilinear and quartic gauge self interactions which are typical for Yang-Mills theories of non-Abelian Lie groups. Finally, note that in the special case of an Abelian $\mathbf{U}(1)$ gauge group such as QED there is just one generator, so that the commutator (A.5) and hence all structure constants as well as self-interactions vanish.

B. Analytical Expressions

B.1. Equations of Motion

For reference, we give here the explicit analytical expression of the SM equations of motion (EOM) as e. g. found in [46], which are used during the operator rewriting in Sec. 2.1.3.

Gauge Fields

Beginning with the gauge fields, the EOM are

$$\partial^\nu B_{\nu\mu} = g'\big(-\frac{1}{2}\bar{\ell}_{Li}\gamma_\mu\ell_{Li} - \bar{e}_{Ri}\gamma_\mu e_{Ri} + \frac{1}{6}\bar{q}_{Li}\gamma_\mu\tau^I q_{Li} + \frac{2}{3}\bar{u}_{Ri}\gamma_\mu u_{Ri} - \frac{1}{3}\bar{d}_{Ri}\gamma_\mu d_{Ri} + \mathrm{i}\phi^\dagger \overleftrightarrow{D}_\mu \phi\big) \ , \tag{B.1a}$$

$$\big(D^\nu W_{\nu\mu}\big)^I = \frac{g}{2}\left(\bar{\ell}_{Li}\gamma_\mu\tau^I\ell_{Li} + \bar{q}_{Li}\gamma_\mu\tau^I q_{Li} + \mathrm{i}\phi^\dagger \overleftrightarrow{D}^I_\mu \phi\right) \ , \tag{B.1b}$$

$$\big(D^\nu G_{\nu\mu}\big)^a = \frac{g_s}{2}\left(\bar{q}_{Li}\gamma_\mu\lambda^a q_{Li} + \bar{u}_{Ri}\gamma_\mu\lambda^a u_{Ri} + \bar{d}_{Ri}\gamma_\mu\lambda^a d_{Ri}\right) \ , \tag{B.1c}$$

with generation indices $i = 1, 2, 3$ being summed over.

Fermions

The EOM of the fermions read

$$\mathrm{i}\not{D} q_{Li} = Y^u_{ij} u_{Rj}\tilde{\phi} + Y^d_{ij} d_{Rj}\phi \ , \tag{B.2a}$$

$$\mathrm{i}\not{D} u_{Ri} = Y^{u\dagger}_{ij}\tilde{\phi}^\dagger q_{Lj} \ , \tag{B.2b}$$

$$\mathrm{i}\not{D} d_{Ri} = Y^{d\dagger}_{ij}\phi^\dagger q_{Lj} \ . \tag{B.2c}$$

Scalar

The EOM of the scalar are

$$D^2\phi = m^2\phi - \lambda\big(\phi^\dagger\phi\big)\phi - Y^{e\dagger}_{ij}\bar{e}_{Rj}\ell_{Lj} - Y^u_{ij}\left(\bar{q}_{Lj}\epsilon\right)^T u_{Rj} - Y^{d\dagger}_{ij}\bar{d}_{Rj}q_{Lj} \ , \tag{B.3a}$$

$$D^2\tilde{\phi} = m^2\tilde{\phi} - \lambda\big(\tilde{\phi}^\dagger\tilde{\phi}\big)\tilde{\phi} - Y^e_{ij}\left(\bar{\ell}_{Lj}\epsilon\right)^T e_{Rj} - Y^{u\dagger}_{ij}\bar{u}_{Rj}q_{Lj} - Y^d_{ij}\left(\bar{q}_{Lj}\epsilon\right)^T d_{Rj} \tag{B.3b}$$

with $\epsilon \equiv \mathrm{i}\tau_2$ acting on left-handed $\mathbf{SU}(2)_L$ doublets.

B.2. Operator Rewritings

Operators $O_{\phi q}^{(1)}$, $O_{\phi q}^{(3)}$ and $O_{\phi u}$

Consider the operators

$$O_{\phi q}^{(1,ij)} = \mathrm{i}\big(\phi^\dagger D_\mu \phi\big)\big(\bar{q}_{Li}\gamma^\mu q_{Lj}\big) \ , \tag{B.4a}$$

$$O_{\phi q}^{(3,ij)} = \mathrm{i}\big(\phi^\dagger \tau^I D_\mu \phi\big)\big(\bar{q}_{Li}\gamma^\mu \tau^I q_{Lj}\big) \ , \tag{B.4b}$$

$$O_{\phi u}^{ij} = \mathrm{i}\big(\phi^\dagger D_\mu \phi\big)\big(\bar{u}_{Ri}\gamma^\mu u_{Rj}\big) \ , \tag{B.4c}$$

whose hermitian part is obviously given by the operators (2.2a)–(2.2c). By partial integration and application of the quark EOM the anti-hermitian part can be explicitly written in the redundant form [47]

$$\Big[O_{\phi q}^{(1,ij)} - \big(O_{\phi q}^{(1,ji)}\big)^\dagger\Big] = \Big[-Y_{jk}^u O_{u\phi}^{ik} - Y_{jk}^d O_{d\phi}^{ik} + Y_{jk}^{u\dagger}\left(O_{u\phi}^{ik}\right)^\dagger + Y_{jk}^{d\dagger}\left(O_{d\phi}^{ik}\right)^\dagger\Big] \ , \tag{B.5a}$$

$$\Big[O_{\phi q}^{(3,ij)} - \big(O_{\phi q}^{(3,ji)}\big)^\dagger\Big] = \Big[Y_{jk}^u O_{u\phi}^{ik} - Y_{jk}^d O_{d\phi}^{ik} - Y_{jk}^{u\dagger}\left(O_{u\phi}^{ik}\right)^\dagger + Y_{jk}^{d\dagger}\left(O_{d\phi}^{ik}\right)^\dagger\Big] \ , \tag{B.5b}$$

$$\Big[O_{\phi u}^{ij} - \big(O_{\phi u}^{ji}\big)^\dagger\Big] = \Big[Y_{ki}^u O_{u\phi}^{kj} - Y_{jk}^{u\dagger}\left(O_{u\phi}^{ki}\right)^\dagger\Big] \ , \tag{B.5c}$$

with

$$O_{d\phi}^{ij} = \big(\phi^\dagger\phi\big)\big(\bar{q}_{Li} d_{Rj}\phi\big) \ . \tag{B.6}$$

Operators O_{qW}, O_{qB}, O_{uB}, O_{qG} and O_{uG}

Following the procedure outlined in Sec. 2.1.3 for O_{qW}, all operators (2.6a)–(2.6e) can be brought into the form [47]

$$\begin{aligned} O_{qW}^{ij} =& + \frac{g}{4}\Big[O_{\phi q}^{(3,ij)} + O_{qq}^{(3,ijkk)} + O_{q\ell}^{(3,ijkk)}\Big] \\ & - \frac{1}{4}\Big[Y_{jk}^u\, O_{uW}^{ik} + Y_{jk}^d\, O_{dW}^{ik} - Y_{ki}^{u\dagger}\big(O_{uW}^{jk}\big)^\dagger - Y_{ki}^{d\dagger}\big(O_{dW}^{jk}\big)^\dagger\Big] \ , \end{aligned} \tag{B.7a}$$

$$\begin{aligned} O_{qB}^{ij} =& + g'\Big[\frac{1}{4}O_{\phi q}^{(1,ij)} + \frac{1}{12}O_{qq}^{(1,ijkk)} - \frac{1}{4}O_{q\ell}^{(1,ijkk)} \\ & \qquad + \frac{1}{3}O_{qu}^{(1,ijkk)} - \frac{1}{6}O_{qd}^{(1,ijkk)} - \frac{1}{2}O_{qe}^{(1,ijkk)}\Big] \\ & - \frac{1}{4}\Big[Y_{jk}^u\, O_{uB\phi}^{ik} + Y_{jk}^d\, O_{dB\phi}^{ik} - Y_{ki}^{u\dagger}\big(O_{uB\phi}^{jk}\big)^\dagger - Y_{ki}^{d\dagger}\big(O_{dB\phi}^{jk}\big)^\dagger\Big] \ , \end{aligned} \tag{B.7b}$$

$$\begin{aligned} O_{uB}^{ij} =& + g'\Big[\frac{1}{4}O_{\phi u}^{ij} + \frac{1}{12}O_{qu}^{(1,ijkk)} - \frac{1}{4}O_{\ell u}^{(1,ijkk)} \\ & \qquad + \frac{1}{3}O_{uu}^{(1,ijkk)} - \frac{1}{6}O_{ud}^{(1,ijkk)} - \frac{1}{2}O_{ue}^{(1,ijkk)}\Big] \\ & - \frac{1}{4}\Big[Y_{ki}^u\, O_{uB\phi}^{kj} - Y_{jk}^{u\dagger}\big(O_{uB\phi}^{ki}\big)^\dagger\Big] \ , \end{aligned} \tag{B.7c}$$

$$O_{qG}^{ij} = +\frac{g_s}{4}\left[O_{qq}^{(8,ijkk)} + O_{qu}^{(8,ijkk)} + O_{qd}^{(8,ijkk)}\right] - \frac{1}{4}\left[Y_{jk}^{u}\, O_{uG\phi}^{ik} + Y_{jk}^{d}\, O_{dG\phi}^{ik} - Y_{ki}^{u\dagger}\left(O_{uG\phi}^{jk}\right)^{\dagger} - Y_{ki}^{d\dagger}\left(O_{dG\phi}^{jk}\right)^{\dagger}\right] , \tag{B.7d}$$

$$O_{uG}^{ij} = +\frac{g_s}{4}\left[O_{qu}^{(8,ijkk)} + O_{uu}^{(8,ijkk)} + O_{ud}^{(8,ijkk)}\right] - \frac{1}{4}\left[Y_{ki}^{u}\, O_{uG\phi}^{kj} - Y_{jk}^{u\dagger}\left(O_{uG\phi}^{ki}\right)^{\dagger}\right] , \tag{B.7e}$$

where

$$O_{dB\phi}^{ij} = \left(\bar{q}_{Li}\sigma^{\mu\nu}d_{Rj}\right)\phi\, B_{\mu\nu} , \tag{B.8a}$$

$$O_{dG\phi}^{ij} = \left(\bar{q}_{Li}\sigma^{\mu\nu}\lambda^{a}d_{Rj}\right)\phi\, G_{\mu\nu}^{a} \tag{B.8b}$$

do not contribute to anomalous top interactions.

Four-fermion Operators

As explained in Sec. 2.1.2 (cf. [49]), a classification of all quartic fermion terms which are built out of hypercharge singlet bilinears results in subsets of definite chirality $(\overline{L}L)(\overline{L}L)$, $(\overline{R}R)(\overline{R}R)$, and $(\overline{L}L)(\overline{R}R)$. Within this basis, one can make use of the completeness relations of the symmetry generators,

$$\tau_{pr}^{I}\tau_{st}^{I} = 2\delta_{pt}\delta_{rs} - \delta_{pr}\delta_{st} \tag{B.9a}$$

$$\lambda_{pr}^{a}\lambda_{st}^{a} = \frac{1}{2}\delta_{pt}\delta_{rs} - \frac{1}{6}\delta_{pr}\delta_{st} \tag{B.9b}$$

(small letters p, r, s, t indicating fundamental group indices) in combination with the Fierz rearrangement for vectors,

$$\left(\overline{\psi}_L\gamma^{\mu}\psi_L\right)\left(\overline{\chi}_L\gamma_{\mu}\chi_L\right) = \left(\overline{\psi}_L\gamma^{\mu}\chi_L\right)\left(\overline{\chi}_L\gamma_{\mu}\psi_L\right) \quad \text{and} \quad L \leftrightarrow R , \tag{B.10}$$

to identify redundancies inside the subsets $(\overline{L}L)(\overline{L}L)$ and $(\overline{R}R)(\overline{R}R)$. For instance [49]

$$\left(\bar{u}_{Ri}\gamma^{\mu}\lambda^{a}u_{Rj}\right)\left(\bar{u}_{Rk}\gamma_{\mu}\lambda^{a}u_{Rl}\right) \overset{(B.9)}{=} \frac{1}{2}\left(\bar{u}_{Ri}^{p}\gamma^{\mu}u_{Rj}^{r}\right)\left(\bar{u}_{Rk}^{r}\gamma_{\mu}u_{Rl}^{p}\right) - \frac{1}{6}O_{qq}^{(1,ijkl)} \tag{B.11a}$$

$$\overset{(B.10)}{=} \frac{1}{2}O_{uu}^{(1,ilkj)} - \frac{1}{6}O_{uu}^{(1,ijkl)} . \tag{B.11b}$$

Similarly, one finds [49]

$$\left(\bar{d}_{Ri}\gamma^{\mu}\lambda^{a}d_{Rj}\right)\left(\bar{d}_{Rk}\gamma_{\mu}\lambda^{a}d_{Rl}\right) = \frac{1}{2}O_{dd}^{(1,ilkj)} - \frac{1}{6}O_{dd}^{(1,ijkl)} , \tag{B.12a}$$

$$\left(\bar{q}_{Li}\gamma^{\mu}\lambda^{a}q_{Lj}\right)\left(\bar{q}_{Lk}\gamma_{\mu}\lambda^{a}q_{Ll}\right) = \frac{1}{4}O_{qq}^{(3,ilkj)} + \frac{1}{4}O_{qq}^{(1,ilkj)} - \frac{1}{6}O_{qq}^{(1,ijkl)} , \tag{B.12b}$$

$$\left(\bar{q}_{Li}\gamma^{\mu}\lambda^{a}\tau^{I}q_{Lj}\right)\left(\bar{q}_{Lk}\gamma_{\mu}\lambda^{a}\tau^{I}q_{Ll}\right) = -\frac{1}{4}O_{qq}^{(3,ilkj)} + \frac{3}{4}O_{qq}^{(1,ilkj)} - \frac{1}{6}O_{qq}^{(1,ijkl)} . \tag{B.12c}$$

B.3. Neutral-current Contact Couplings

The mapping of the NC contact interaction couplings introduced in Sec. 2.3.2 onto respective operator coefficients will be listed here. The eight real color-singlet vector couplings are

$$\chi^{(1)}_{LLu} = C^{(1,33kk)}_{qq} + C^{(1,kk33)}_{qq} + 2\big(C^{(3,33kk)}_{qq} + C^{(3,kk33)}_{qq}\big)\,, \tag{B.13a}$$
$$\chi^{(1)}_{LLd} = C^{(1,33kk)}_{qq} + C^{(1,kk33)}_{qq} - 2\big(C^{(3,33kk)}_{qq} + C^{(3,kk33)}_{qq}\big)\,, \tag{B.13b}$$
$$\chi^{(1)}_{RRu} = C^{(1,33kk)}_{uu} + C^{(1,kk33)}_{uu}\,, \tag{B.13c}$$
$$\chi^{(1)}_{RRd} = C^{(1,33kk)}_{ud}\,, \tag{B.13d}$$
$$\chi^{(1)}_{LRu} = C^{(1,33kk)}_{qu}\,, \tag{B.13e}$$
$$\chi^{(1)}_{LRd} = C^{(1,33kk)}_{qd}\,, \tag{B.13f}$$
$$\chi^{(1)}_{RLu} = C^{(1,kk33)}_{qu}\,, \tag{B.13g}$$
$$\chi^{(1)}_{RLd} = C^{(1,kk33)}_{qu}\,. \tag{B.13h}$$

The five real color-octet vector couplings read

$$\chi^{(8)}_{RRd} = C^{(8,33kk)}_{ud}\,, \tag{B.14a}$$
$$\chi^{(8)}_{LRu} = C^{(8,33kk)}_{qu}\,, \qquad \chi^{(8)}_{LRd} = C^{(8,33kk)}_{qd}\,, \tag{B.14b}$$
$$\chi^{(8)}_{RLu} = C^{(8,kk33)}_{qu}\,, \qquad \chi^{(8)}_{RLd} = C^{(8,kk33)}_{qu}\,. \tag{B.14c}$$

In addition, there are two complex color-singlet resp. color-octet scalar couplings,

$$\eta^{(1)}_{L} = \big(C^{(1,33kk)}_{quqd}\big)^*\,, \qquad \eta^{(1)}_{R} = C^{(1,33kk)}_{quqd}\,, \tag{B.15a}$$
$$\eta^{(8)}_{L} = \big(C^{(8,33kk)}_{quqd}\big)^*\,, \qquad \eta^{(8)}_{R} = C^{(8,33kk)}_{quqd}\,. \tag{B.15b}$$

C. Whizard Default Setup

As a compact reference, we provide here a list of all relevant input parameters to WHIZARD together with the respective numerical values employed (corresponding to the default setup of the WHIZARD 2 SM model). The independent parameters are

$$\begin{aligned}
&\text{Fermi's constant:} && G_F = 1.16639 \times 10^{-5}\,\text{GeV}^{-2} && \text{(C.1a)}\\
&Z \text{ boson mass:} && m_Z = 91.1882\,\text{GeV} && \text{(C.1b)}\\
&W \text{ boson mass:} && m_W = 80.419\,\text{GeV} && \text{(C.1c)}\\
&\text{Higgs mass:} && m_h = 125\,\text{GeV} && \text{(C.1d)}\\
&\text{strong coupling:} && \alpha_s = 0.1178 \quad \text{(at the } Z \text{ point)} && \text{(C.1e)}\\
&\text{bottom quark mass:} && m_b = 4.2\,\text{GeV} && \text{(C.1f)}\\
&\text{top quark mass:} && m_t = 173.1\,\text{GeV} && \text{(C.1g)}\\
&\text{top width:} && \Gamma_t = 1.523\,\text{GeV} \quad \text{(SM reference value)} && \text{(C.1h)}\\
&Z \text{ width:} && \Gamma_Z = 2.443\,\text{GeV} && \text{(C.1i)}\\
&W \text{ width:} && \Gamma_W = 2.049\,\text{GeV} && \text{(C.1j)}\\
&h \text{ width:} && \Gamma_h = 0.004143\,\text{GeV}\ . && \text{(C.1k)}
\end{aligned}$$

From these values, the dependent parameters are fixed as

$$\begin{aligned}
&\text{electroweak vev:} && v = \frac{1}{\sqrt{\sqrt{2}G_F}} && \text{(C.2a)}\\
&\text{Weinberg angle (cosine):} && c_w = \frac{m_W}{m_Z} && \text{(C.2b)}\\
&\text{Weinberg angle (sine):} && s_w = \sqrt{1 - c_w^2} && \text{(C.2c)}\\
&\text{electromagnetic coupling:} && \mathrm{e} = 2 s_w \frac{m_W}{v}\ . && \text{(C.2d)}
\end{aligned}$$

In addition to these numerical values, the pdf employed by default for the initial state protons is CTEQ6L [144], dynamically setting the factorization scale to the partonic $\sqrt{\hat{s}}$ in each event.

D. O'Mega Code

D.1. Naming Conventions in the Model File

All anomalous couplings discussed in Secs. 2.2 and 2.3.1 are available as parameters in the model file `SM_top_anom.mdl`. For the trilinear couplings, we provide two normalization conventions controlled by the switch `norm_conv`. For `norm_conv` > 0 (default), the convention is exactly the one of Sec. 2.2 (which follows [46, 47]), while for `norm_conv` < 0 the ratio of scales v^2/Λ^2 is kept explicitly, so that the coupling values become of the order of magnitude of the underlying Wilson coefficients. The model parameter `Lambda` sets the overall normalization when `norm_conv` < 0, and also normalizes the the momentum transfer q^2 when a form factor approach (cf. Sec. 3.2.1) is chosen by setting the parameter `fun_flag` $\neq 0$.

In the default setup (`norm_conv` > 0), the dictionary for all the trilinear couplings of Secs. 2.2.2–2.2.6 reads

$$V_L = \texttt{vl\_tbW\_Re} + \mathrm{i}\,\texttt{vl\_tbW\_Im} \qquad V_R = \texttt{vr\_tbW\_Re} + \mathrm{i}\,\texttt{vr\_tbW\_Im} \tag{D.1a}$$

$$g_L = \texttt{tl\_tbW\_Re} + \mathrm{i}\,\texttt{tl\_tbW\_Im} \qquad g_R = \texttt{tr\_tbW\_Re} + \mathrm{i}\,\texttt{tr\_tbW\_Im} \tag{D.1b}$$

$$X_{tt}^L = \texttt{vl\_ttZ} \qquad X_{tt}^R = \texttt{vr\_ttZ} \tag{D.1c}$$

$$d_V^Z = \texttt{tv\_ttZ} \qquad d_A^Z = \texttt{ta\_ttZ} \tag{D.1d}$$

$$d_V^\gamma = \texttt{tv\_ttA} \qquad d_A^\gamma = \texttt{ta\_ttA} \tag{D.1e}$$

$$d_V^g = \texttt{tv\_ttG} \qquad d_A^g = \texttt{ta\_ttG} \tag{D.1f}$$

$$Y_t^V = \texttt{s\_ttH} \qquad Y_t^A = \texttt{p\_ttH}\,, \tag{D.1g}$$

cf. Eq. (D.3) below for V_L^{off}. Some of these couplings are not independent but related to others and to anomalous bottom couplings by gauge invariance, as discussed in Sec. 2.4. These relations can be switched on (default) and off by setting the model parameter `gauge_inv` > 0 or < 0.

The dictionary for the four-fermion CC contact interactions of Sec. 2.3.1 is

$$V^{(3)} = \texttt{v3\_4f} \tag{D.2a}$$

$$S_L^{(1)} = \texttt{s1l\_4f\_Re} + \mathrm{i}\,\texttt{s1l\_4f\_Im} \qquad S_R^{(1)} = \texttt{s1r\_4f\_Re} + \mathrm{i}\,\texttt{s1r\_4f\_Im} \tag{D.2b}$$

$$S_L^{(8)} = \texttt{s8l\_4f\_Re} + \mathrm{i}\,\texttt{s8l\_4f\_Im} \qquad S_R^{(8)} = \texttt{s8r\_4f\_Re} + \mathrm{i}\,\texttt{s8r\_4f\_Im}\,. \tag{D.2c}$$

Finally, note that the vector coupling $V^{(3)}$ was also labeled V_L^{off} in Secs. 2.2.2 and 5.1 (up to a normalization factor), in order to emphasize its relation to the trilinear coupling V_L. Instead of explicitly introducing it as a parameter in `SM_top_anom.mdl`,

we just repeat here the normalization factor, Eq. (2.28), times the model parameter:

$$V_L^{\text{off}} = \frac{\upsilon^2}{2\Lambda^2}\,\texttt{v3\_4f}\,. \tag{D.3}$$

D.2. Implementation of the $\overline{\Psi}$–T–Ψ Fusions

For reference, we give here the FORTRAN vertex functions which were added to `omegalib.nw` in order to provide the antisymmetric Lorentz tensor structure $\sigma^{\mu\nu}$ between two fermions. The respective functions fuse two wave functions given as arguments into one wave function returned as result. For instance, the fusion direction $\overline{\Psi}\sigma^{\mu\nu}(g_V + g_A\gamma_5)\Psi \to T^{\mu\nu}$ is implemented as

```
pure function tva_ff (gv, ga, psibar, psi) result (t)
 type(tensor2odd) :: t
 complex(kind=default), intent(in) :: gv, ga
 type(conjspinor), intent(in) :: psibar
 type(spinor), intent(in) :: psi
 complex(kind=default) :: gl, gr
 complex(kind=default) :: g12, g21, g1m2, g34, g43, g3m4
 gr     = gv + ga
 gl     = gv - ga
 g12    = psibar%a(1)*psi%a(2)
 g21    = psibar%a(2)*psi%a(1)
 g1m2   = psibar%a(1)*psi%a(1) - psibar%a(2)*psi%a(2)
 g34    = psibar%a(3)*psi%a(4)
 g43    = psibar%a(4)*psi%a(3)
 g3m4   = psibar%a(3)*psi%a(3) - psibar%a(4)*psi%a(4)
 t%e(1) = (gl * ( - g12 - g21) + gr * (   g34 + g43)) * (0, 1)
 t%e(2) =  gl * ( - g12 + g21) + gr * (   g34 - g43)
 t%e(3) = (gl * ( - g1m2     ) + gr * (   g3m4     )) * (0, 1)
 t%b(1) =  gl * (   g12 + g21) + gr * (   g34 + g43)
 t%b(2) = (gl * ( - g12 + g21) + gr * ( - g34 + g43)) * (0, 1)
 t%b(3) =  gl * (   g1m2     ) + gr * (   g3m4     )
end function tva_ff
```

where all components of $T^{\mu\nu}$ are fixed by two independent 3-vectors, `t%e` and `t%b`, analog to the construction of the electromagnetic field strength $F^{\mu\nu}$ from $\vec{E}$ and $\vec{B}$ vectors. This function is reused in various ways, e. g. to implement other coupling parametrizations like $\overline{\Psi}\sigma^{\mu\nu}(g_L P_L + g_R P_R)\Psi \to T^{\mu\nu}$ as

```
pure function tlr_ff (gl, gr, psibar, psi) result (t)
 ...
 t = tva_ff (gr+gl, gr-gl, psibar, psi)
end function tlr_ff
```

Note that in this convention (complying with O'Mega standard) the projectors $P_{L,R}$ do *not* include the factor 1/2 of Eq. (1.5), so that it has to be multiplied explicitly during the initialization of the chiral couplings in the parameters module. Furthermore, since $\sigma^{\mu\nu}$ does not conserve chirality, the chiral vertex parametrizations $\propto g_{L,R}$ also need flipped variants, e. g. `trl_ff` with $g_L \leftrightarrow g_R$ in the argument. In addition, dipole vertices with a contracted 4-momentum, like $\overline{\Psi}\mathrm{i}\sigma^{\mu\nu}q_\nu(g_V + g_A\gamma_5)\Psi \to J^\mu$, are constructed as

```
pure function tvam_ff (gv, ga, psibar, psi, p) result (j)
  ...
  j = (tva_ff(gv, ga, psibar, psi) * p) * (0,1)
end function tvam_ff
```

with obvious generalizations to `tlrm_ff` and `trlm_ff`.

It remains to give the implementations of the other two possible vertex fusion directions, namely $T^{\mu\nu}(g_V + g_A\gamma_5)\Psi \to \Psi$,

```
pure function f_tvaf (gv, ga, t, psi) result (tpsi)
  type(spinor) :: tpsi
  complex(kind=default), intent(in) :: gv, ga
  type(tensor2odd), intent(in) :: t
  type(spinor), intent(in) :: psi
  complex(kind=default) :: gl, gr
  complex(kind=default) :: e21, e21s, b12, b12s, be3, be3s
  gr   = gv + ga
  gl   = gv - ga
  e21  = t%e(2) + t%e(1)*(0,1)
  e21s = t%e(2) - t%e(1)*(0,1)
  b12  = t%b(1) + t%b(2)*(0,1)
  b12s = t%b(1) - t%b(2)*(0,1)
  be3  = t%b(3) + t%e(3)*(0,1)
  be3s = t%b(3) - t%e(3)*(0,1)
  tpsi%a(1) =   2*gl * (   psi%a(1) * be3  + psi%a(2) * ( e21 +b12s))
  tpsi%a(2) =   2*gl * ( - psi%a(2) * be3  + psi%a(1) * (-e21s+b12 ))
  tpsi%a(3) =   2*gr * (   psi%a(3) * be3s + psi%a(4) * (-e21 +b12s))
  tpsi%a(4) =   2*gr * ( - psi%a(4) * be3s + psi%a(3) * ( e21s+b12 ))
end function f_tvaf
```

giving rise to the functions `f_tlrf` and `f_trlf`, plus momentum versions like $\mathrm{i}\sigma^{\mu\nu}A_\mu q_\nu(g_V + g_A\gamma_5)\Psi \to \Psi$,

```
pure function f_tvamf (gv, ga, v, psi, k) result (vpsi)
  ...
  type(tensor2odd) :: t
  t = (v.wedge.k) * (0, 0.5)
  vpsi = f_tvaf(gv, ga, t, psi)
end function f_tvamf
```

and `f_tlrmf`, `f_trlmf`, as before. The last fusion direction is $\overline{\Psi} T^{\mu\nu}(g_V + g_A\gamma_5) \to \overline{\Psi}$,

```
pure function f_ftva (gv, ga, psibar, t) result (psibart)
 type(conjspinor) :: psibart
 complex(kind=default), intent(in) :: gv, ga
 type(conjspinor), intent(in) :: psibar
 type(tensor2odd), intent(in) :: t
 complex(kind=default) :: gl, gr
 complex(kind=default) :: e21, e21s, b12, b12s, be3, be3s
 gr   = gv + ga
 gl   = gv - ga
 e21  = t%e(2) + t%e(1)*(0,1)
 e21s = t%e(2) - t%e(1)*(0,1)
 b12  = t%b(1) + t%b(2)*(0,1)
 b12s = t%b(1) - t%b(2)*(0,1)
 be3  = t%b(3) + t%e(3)*(0,1)
 be3s = t%b(3) - t%e(3)*(0,1)
 psibart%a(1) = 2*gl * ( psibar%a(1)*be3  +psibar%a(2)*(-e21s+b12 ))
 psibart%a(2) = 2*gl * (-psibar%a(2)*be3  +psibar%a(1)*( e21 +b12s))
 psibart%a(3) = 2*gr * ( psibar%a(3)*be3s +psibar%a(4)*( e21s+b12 ))
 psibart%a(4) = 2*gr * (-psibar%a(4)*be3s +psibar%a(3)*(-e21 +b12s))
end function f_ftva
```

with respective functions `f_ftlr` and `f_ftrl` as well as momentum versions `f_ftvam`, `f_ftlrm` and `f_ftrlm`.

D.3. Implementation of Contact interactions

As already stated in Sec. 3.2.2, we first define the auxiliary field Π, called `Aux_top` in `modellib_SM.ml`, and assign to it a set of quantum numbers:

```
type other = ... | Aux_top of int*int*int*bool*f_aux_top
                          (*i lorentz*color*charge*top-side*flavor *)
```

where *lorentz* labels the possible Lorentz representations (scalar, 4-vector or anti-symmetric tensor), mapped by the function

```
let lorentz_aux = function
     | 2 -> Tensor_1
     | 1 -> Vector
     | 0 -> Scalar
     | _ -> invalid_arg ("SM.lorentz_aux: wrong value")
```

with a similar function `prop_aux` onto a constant propagator. *color* switches between color representations,

```
let color = function
```

```
...
| 0 (Aux_top (_,co,_,_,_)) ->
   if co == 0 then Color.Singlet else Color.AdjSUN 3
| _ -> Color.Singlet
```

and *charge* is the ordinary electromagnetic charge. *top-side* is the new boolean quantum number n discussed in Sec. 3.2.2, while *flavor* labels the various contact interactions. Now we implement the conjugation behavior described in Sec. 3.2.2 for an off-diagonal propagator:

```
let conjugate = function
    ...
      | Aux_top (l,co,ch,n,f) -> Aux_top (l,co,(-ch),(not n),f)
```

Finally, O'Mega needs the vertex Feynman rules, Eq. (3.13a). Sticking to the CC interactions for illustration, the *tbWA* term, cf. Eqs. (2.21) and (2.22), is stated as

```
((M (D (-3)), 0 (Aux_top (2,0,-1,true,TBWA)), M (U 3)),
                              FBF (1, Psibar, TLR, Psi), G_TLR_btWA);
((0 (Aux_top (2,0,1,false,TBWA)), G Ga, G Wm),
                              Aux_Gauge_Gauge 1, I_G_weak);
((M (U (-3)), 0 (Aux_top (2,0,1,true,TBWA)), M (D 3)),
                              FBF (1, Psibar, TRL, Psi), G_TRL_tbWA);
((0 (Aux_top (2,0,-1,false,TBWA)), G Wp, G Ga),
                              Aux_Gauge_Gauge 1, I_G_weak)
```

with a *flavor* label `TBWA` for this interaction. Here the generalized $\overline{\Psi}$–T–Ψ structure, cf. Eq. (3.10) and appendix D.2 above, pays off: in order to correctly fuse the tensorial `Aux_top` to the fermion line, we just call the same vertex functions without the momentum contraction, using the keywords `TLR` and `TRL` (`TVA` also exists). Concerning the couplings, `I_G_weak` $= g_0$ and `G_TLR_btWA` $= g_1$ are in this case fixed relative to the trilinear *tbW* couplings $g_{L,R}$ by gauge invariance. We choose

$$g_1 = -s_w g_{L,R}, \qquad g_0 = \mathrm{i}g \tag{D.4}$$

from Eqs. (2.21), (2.22) and (2.24b), also inserting the sign of Eq. (3.11). The fusion of the tensor with the two gauge bosons is done by the set of fusion functions labeled `Aux_Gauge_Gauge` which compute $A \wedge A' \to T$ (and the other fusion directions). The explicitly antisymmetrized product accounts for the asymmetry of the field strength tensor from which the term originates. In addition, in QCD amplitudes like *ttgg* (cf. Sec. 3.3) the $\wedge$ is required to internally handle the color structure in the color flow basis [56, 142, 143], where all adjoint indices are removed in favor of fundamental ones. In our case, the vertex $\sim g_s f_{abc} \Pi_a^{\mu\nu} G_\mu^b G_\nu^c$ needed for the *ttgg* contact interaction is internally represented as $g_s \Pi \cdot (G \wedge G)$ with a globally rescaled strong coupling $g_s \to g_s/\sqrt{2}$, where all three fields carry two (suppressed) indices of the color product representation $3 \otimes \overline{3}$. The generalization of the procedure to the other top–gauge interactions *tbWZ*, *ttWW* and *bbWW*, as well as the four-fermion interactions is straightforward: just state the vertices and give the correct representation to `Aux_top`.

Bibliography

[1] S. L. Glashow, Nuclear Physics **22**, 579 (1961).

[2] S. Weinberg, Phys. Rev. Lett. **19**, 1264 (1967).

[3] A. Salam, Conf.Proc. **C680519**, 367 (1968).

[4] UA1 Collaboration, G. Arnison *et al.*, Physics Letters B **122**, 103 (1983).

[5] UA2 Collaboration, M. Banner *et al.*, Physics Letters B **122**, 476 (1983).

[6] UA1 Collaboration, G. Arnison *et al.*, Phys.Lett. **B126**, 398 (1983).

[7] S. L. Glashow, J. Iliopoulos, and L. Maiani, Phys. Rev. D **2**, 1285 (1970).

[8] J. J. Aubert *et al.*, Phys. Rev. Lett. **33**, 1404 (1974).

[9] J. E. Augustin *et al.*, Phys. Rev. Lett. **33**, 1406 (1974).

[10] S. W. Herb *et al.*, Phys. Rev. Lett. **39**, 252 (1977).

[11] CDF Collaboration, F. Abe *et al.*, Phys.Rev.Lett. **74**, 2626 (1995), [arXiv:hep-ex/9503002].

[12] D0 Collaboration, S. Abachi *et al.*, Phys.Rev.Lett. **74**, 2632 (1995), [arXiv:hep-ex/9503003].

[13] Tevatron Electroweak Working Group, for the CDF and D0 Collaborations, M. Lancaster, (2011), [arXiv:1107.5255].

[14] V. Flyagin and V. Glagolev, Phys.Part.Nucl. **43**, 106 (2012).

[15] CDF Collaboration, T. Aaltonen *et al.*, (2012), [arXiv:1207.6758].

[16] CDF Collaboration, D0 Collaboration, T. Aaltonen *et al.*, (2012), [arXiv:1202.5272].

[17] Atlas Collaboration, G. Aad *et al.*, Eur.Phys.J. **C71**, 1577 (2011), [arXiv:1012.1792].

[18] CMS Collaboration, S. Chatrchyan *et al.*, Eur.Phys.J. **C71**, 1721 (2011), [arXiv:1106.0902].

[19] CMS Collaboration, S. Chatrchyan *et al.*, JHEP **1107**, 049 (2011), [arXiv:1105.5661].

[20] ATLAS Collaboration, G. Aad *et al.*, JHEP **1205**, 059 (2012), [arXiv:1202.4892].

[21] CMS Collaboration, S. Chatrchyan *et al.*, Phys.Rev. **D85**, 112007 (2012), [arXiv:1203.6810].

[22] ATLAS Collaboration, G. Aad *et al.*, (2012), [arXiv:1205.2067].

[23] CMS Collaboration, S. Chatrchyan *et al.*, (2012), [arXiv:1209.3489].

[24] CERN Report No. ATLAS-CONF-2011-104, 2011 (unpublished).

[25] CMS Collaboration, S. Chatrchyan *et al.*, Phys.Rev.Lett. **107**, 091802 (2011), [arXiv:1106.3052].

[26] ATLAS Collaboration, G. Aad *et al.*, (2012), [arXiv:1205.3130].

[27] CMS Collaboration, S. Chatrchyan *et al.*, (2012), [arXiv:1209.4533].

[28] D0 Collaboration, V. M. Abazov *et al.*, (2013), [arXiv:1307.0731].

[29] ATLAS Collaboration, G. Aad *et al.*, Physics Letters B **716**, 1 (2012), [arXiv:1207.7214].

[30] CMS Collaboration, S. Chatrchyan *et al.*, Physics Letters B **716**, 30 (2012), [arXiv:1207.7235].

[31] P. W. Higgs, Phys.Lett. **12**, 132 (1964).

[32] P. W. Higgs, Phys.Rev.Lett. **13**, 508 (1964).

[33] F. Englert and R. Brout, Phys.Rev.Lett. **13**, 321 (1964).

[34] G. Guralnik, C. Hagen, and T. Kibble, Phys.Rev.Lett. **13**, 585 (1964).

[35] R. Contino, L. Da Rold, and A. Pomarol, Phys.Rev. **D75**, 055014 (2007), [arXiv:hep-ph/0612048].

[36] G. Giudice, C. Grojean, A. Pomarol, and R. Rattazzi, JHEP **0706**, 045 (2007), [arXiv:hep-ph/0703164].

[37] H. S. Fukano and K. Tuominen, (2012), [arXiv:1210.6756].

[38] W. Buchmuller and D. Wyler, Nucl.Phys. **B268**, 621 (1986).

[39] C. Arzt, M. Einhorn, and J. Wudka, Nucl.Phys. **B433**, 41 (1995), [arXiv:hep-ph/9405214].

[40] G. Gounaris, M. Kuroda, and F. Renard, Phys.Rev. **D54**, 6861 (1996), [arXiv:hep-ph/9606435].

[41] G. Gounaris, D. Papadamou, and F. Renard, Z.Phys. **C76**, 333 (1997), [arXiv:hep-ph/9609437].

[42] L. Brzezinski, B. Grzadkowski, and Z. Hioki, Int.J.Mod.Phys. **A14**, 1261 (1999), [arXiv:hep-ph/9710358].

[43] K. Whisnant, J.-M. Yang, B.-L. Young, and X. Zhang, Phys.Rev. **D56**, 467 (1997), [arXiv:hep-ph/9702305].

[44] J. M. Yang and B.-L. Young, Phys.Rev. **D56**, 5907 (1997), [arXiv:hep-ph/9703463].

[45] B. Grzadkowski, Z. Hioki, K. Ohkuma, and J. Wudka, Nucl.Phys. **B689**, 108 (2004), [arXiv:hep-ph/0310159].

[46] J. Aguilar-Saavedra, Nucl.Phys. **B812**, 181 (2009), [arXiv:0811.3842].

[47] J. Aguilar-Saavedra, Nucl.Phys. **B821**, 215 (2009), [arXiv:0904.2387].

[48] J. Aguilar-Saavedra, Nucl.Phys. **B843**, 638 (2011), [arXiv:1008.3562].

[49] B. Grzadkowski, M. Iskrzynski, M. Misiak, and J. Rosiek, JHEP **1010**, 085 (2010), [arXiv:1008.4884].

[50] S. Weinberg, Phys.Lett. **B91**, 51 (1980).

[51] J. Gasser and H. Leutwyler, Annals Phys. **158**, 142 (1984).

[52] H. Georgi, Nucl.Phys. **B361**, 339 (1991).

[53] A. De Rujula, M. Gavela, P. Hernandez, and E. Masso, Nucl.Phys. **B384**, 3 (1992).

[54] C. Arzt, Phys.Lett. **B342**, 189 (1995), [arXiv:hep-ph/9304230].

[55] F. Bach and T. Ohl, Phys.Rev. **D86**, 114026 (2012), [arXiv:1209.4564].

[56] W. Kilian, T. Ohl, and J. Reuter, Eur.Phys.J. **C71**, 1742 (2011), [arXiv:0708.4233].

[57] T. Sjostrand, S. Mrenna, and P. Z. Skands, JHEP **0605**, 026 (2006), [arXiv:hep-ph/0603175].

[58] S. Ovyn, X. Rouby, and V. Lemaitre, (2009), [arXiv:0903.2225].

[59] J. de Favereau *et al.*, (2013), [arXiv:1307.6346].

[60] E. Fermi, Z.Phys. **88**, 161 (1934).

[61] J. J. Sakurai, *Modern quantum mechanics* (Pearson Education, 2009).

[62] Gargamelle Neutrino Collaboration, F. Hasert *et al.*, Phys.Lett. **B46**, 138 (1973).

[63] M. Peskin and D. Schroeder, *An introduction to quantum field theory* (Addison-Wesley Publishing Company, 1995).

[64] T. Appelquist and J. Carazzone, Phys.Rev. **D11**, 2856 (1975).

[65] C. Burges and H. J. Schnitzer, Nucl.Phys. **B228**, 464 (1983).

[66] C. N. Leung, S. Love, and S. Rao, Z.Phys. **C31**, 433 (1986).

[67] A. V. Manohar, (1996), [arXiv:hep-ph/9606222].

[68] S. Kamefuchi, L. O'Raifeartaigh, and A. Salam, Nucl.Phys. **28**, 529 (1961).

[69] M. Bergere and Y.-M. P. Lam, Phys.Rev. **D13**, 3247 (1976).

[70] A. Salam and J. Strathdee, Phys.Rev. **D2**, 2869 (1970).

[71] R. Kallosh and I. Tyutin, Yad.Fiz. **17**, 190 (1973).

[72] H. D. Politzer, Nucl.Phys. **B172**, 349 (1980).

[73] H. Kluberg-Stern and J. Zuber, Phys.Rev. **D12**, 3159 (1975).

[74] C. Grosse-Knetter, Phys.Rev. **D49**, 6709 (1994), [arXiv:hep-ph/9306321].

[75] J. Wudka, Int.J.Mod.Phys. **A9**, 2301 (1994), [arXiv:hep-ph/9406205].

[76] A. J. Buras, Acta Phys.Polon. **B34**, 5615 (2003), [arXiv:hep-ph/0310208].

[77] A. L. Kagan, G. Perez, T. Volansky, and J. Zupan, Phys.Rev. **D80**, 076002 (2009), [arXiv:0903.1794].

[78] J. Aguilar-Saavedra, J. Carvalho, N. F. Castro, A. Onofre, and F. Veloso, Eur.Phys.J. **C53**, 689 (2008), [arXiv:0705.3041].

[79] J. Aguilar-Saavedra, Nucl.Phys. **B804**, 160 (2008), [arXiv:0803.3810].

[80] J. Aguilar-Saavedra, N. Castro, and A. Onofre, Phys.Rev. **D83**, 117301 (2011), [arXiv:1105.0117].

[81] ATLAS Collaboration, G. Aad *et al.*, JHEP **1206**, 088 (2012), [arXiv:1205.2484].

[82] B. Grzadkowski, Z. Hioki, and M. Szafranski, Phys.Rev. **D58**, 035002 (1998), [arXiv:hep-ph/9712357].

[83] Q.-H. Cao, J. Wudka, and C.-P. Yuan, Phys.Lett. **B658**, 50 (2007), [arXiv:0704.2809].

[84] E. L. Berger, Q.-H. Cao, and I. Low, Phys.Rev. **D80**, 074020 (2009), [arXiv:0907.2191].

[85] B. Grzadkowski and M. Misiak, Phys.Rev. **D78**, 077501 (2008), [arXiv:0802.1413].

[86] J. Drobnak, S. Fajfer, and J. F. Kamenik, Phys.Lett. **B701**, 234 (2011), [arXiv:1102.4347].

[87] J. Drobnak, S. Fajfer, and J. F. Kamenik, Nucl.Phys. **B855**, 82 (2012), [arXiv:1109.2357].

[88] G. Buchalla, A. J. Buras, and M. E. Lautenbacher, Rev.Mod.Phys. **68**, 1125 (1996), [arXiv:hep-ph/9512380].

[89] T. Hurth, G. Isidori, J. F. Kamenik, and F. Mescia, Nucl.Phys. **B808**, 326 (2009), [arXiv:0807.5039].

[90] Heavy Flavor Averaging Group, D. Asner *et al.*, (2010), [arXiv:1010.1589].

[91] T. Huber, T. Hurth, and E. Lunghi, Nucl.Phys. **B802**, 40 (2008), [arXiv:0712.3009].

[92] Particle Data Group, J. Beringer *et al.*, Phys.Rev. **D86**, 010001 (2012).

[93] R. Dalitz and G. R. Goldstein, Phys.Rev. **D45**, 1531 (1992).

[94] J. Aguilar-Saavedra, J. Carvalho, N. F. Castro, F. Veloso, and A. Onofre, Eur.Phys.J. **C50**, 519 (2007), [arXiv:hep-ph/0605190].

[95] D0 Collaboration, V. M. Abazov *et al.*, Phys.Rev. **D85**, 091104 (2012), [arXiv:1201.4156].

[96] M. Jezabek and J. H. Kuhn, Phys.Lett. **B329**, 317 (1994), [arXiv:hep-ph/9403366].

[97] M. Jezabek, Nucl.Phys.Proc.Suppl. **37B**, 197 (1994), [arXiv:hep-ph/9406411].

[98] A. Czarnecki, M. Jezabek, and J. H. Kuhn, Phys.Lett. **B346**, 335 (1995), [arXiv:hep-ph/9411282].

[99] A. Brandenburg, Z. Si, and P. Uwer, Phys.Lett. **B539**, 235 (2002), [arXiv:hep-ph/0205023].

[100] W. Bernreuther, A. Brandenburg, Z. Si, and P. Uwer, Nucl.Phys. **B690**, 81 (2004), [arXiv:hep-ph/0403035].

[101] J. Aguilar-Saavedra and J. Bernabeu, Nucl.Phys. **B840**, 349 (2010), [arXiv:1005.5382].

[102] P. Nason, S. Dawson, and R. K. Ellis, Nucl.Phys. **B303**, 607 (1988).

[103] M. Czakon, P. Fiedler, and A. Mitov, (2013), [arXiv:1303.6254].

[104] N. Kidonakis, (2013), [arXiv:1304.7775].

[105] K. Melnikov and M. Schulze, JHEP **0908**, 049 (2009), [arXiv:0907.3090].

[106] F.-P. Schilling, Int.J.Mod.Phys. **A27**, 1230016 (2012), [arXiv:1206.4484].

[107] K.-m. Cheung, Phys.Rev. **D53**, 3604 (1996), [arXiv:hep-ph/9511260].

[108] Z. Hioki and K. Ohkuma, Eur.Phys.J. **C65**, 127 (2010), [arXiv:0910.3049].

[109] D. Choudhury and P. Saha, Pramana **77**, 1079 (2011), [arXiv:0911.5016].

[110] J. H. Kuhn and G. Rodrigo, Phys.Rev. **D59**, 054017 (1999), [arXiv:hep-ph/9807420].

[111] CDF Collaboration, T. Aaltonen *et al.*, Phys. Rev. D 87, **092002** (2013), [arXiv:1211.1003].

[112] D0 Collaboration, V. M. Abazov *et al.*, Phys.Rev. **D84**, 112005 (2011), [arXiv:1107.4995].

[113] D0 Collaboration, V. M. Abazov *et al.*, (2012), [arXiv:1207.0364].

[114] D. Choudhury, R. M. Godbole, S. D. Rindani, and P. Saha, Phys.Rev. **D84**, 014023 (2011), [arXiv:1012.4750].

[115] D.-W. Jung, P. Ko, J. S. Lee, and S.-h. Nam, Phys.Lett. **B691**, 238 (2010), [arXiv:0912.1105].

[116] ATLAS Collaboration, G. Aad *et al.*, Eur.Phys.J. **C72**, 2039 (2012), [arXiv:1203.4211].

[117] CMS Collaboration, S. Chatrchyan *et al.*, Phys.Lett. **B717**, 129 (2012), [arXiv:1207.0065].

[118] K. Melnikov, M. Schulze, and A. Scharf, Phys.Rev. **D83**, 074013 (2011), [arXiv:1102.1967].

[119] S. Biswas, E. Gabrielli, and B. Mele, JHEP **1301**, 088 (2013), [arXiv:1211.0499].

[120] X.-G. He, Y. Tang, and G. Valencia, (2013), [arXiv:1305.5420].

[121] D. Choudhury and P. Saha, JHEP **1208**, 144 (2012), [arXiv:1201.4130].

[122] L. Labun and J. Rafelski, (2012), [arXiv:1209.1046].

[123] N. Kidonakis, Phys.Rev. **D81**, 054028 (2010), [arXiv:1001.5034].

[124] N. Kidonakis, Phys.Rev. **D83**, 091503 (2011), [arXiv:1103.2792].

[125] N. Kidonakis, Phys.Rev. **D82**, 054018 (2010), [arXiv:1005.4451].

[126] A. Papanastasiou, R. Frederix, S. Frixione, V. Hirschi, and F. Maltoni, (2013), [arXiv:1305.7088].

[127] CERN Report No. ATLAS-CONF-2011-118, 2011 (unpublished).

[128] B. Harris, E. Laenen, L. Phaf, Z. Sullivan, and S. Weinzierl, Phys.Rev. **D66**, 054024 (2002), [arXiv:hep-ph/0207055].

[129] S. Zhu, Physics Letters B **524**, 283 (2002).

[130] S. Zhu, Physics Letters B **537**, 351 (2002).

[131] G. Mahlon and S. J. Parke, Phys.Lett. **B476**, 323 (2000), [arXiv:hep-ph/9912458].

[132] J. C. Collins, D. E. Soper, and G. F. Sterman, Adv.Ser.Direct.High Energy Phys. **5**, 1 (1988), [arXiv:hep-ph/0409313].

[133] M. Moretti, T. Ohl, and J. Reuter, (2001), [arXiv:hep-ph/0102195].

[134] A. Pukhov, (2004), [arXiv:hep-ph/0412191].

[135] F. Caravaglios and M. Moretti, Phys.Lett. **B358**, 332 (1995), [arXiv:hep-ph/9507237].

[136] A. Kanaki and C. G. Papadopoulos, Comput.Phys.Commun. **132**, 306 (2000), [arXiv:hep-ph/0002082].

[137] C. Speckner, (2010), [arXiv:1011.1851].

[138] G. P. Lepage, J.Comput.Phys. **27**, 192 (1978).

[139] T. Ohl, Comput.Phys.Commun. **120**, 13 (1999), [arXiv:hep-ph/9806432].

[140] N. D. Christensen, C. Duhr, B. Fuks, J. Reuter, and C. Speckner, Eur.Phys.J. **C72**, 1990 (2012), [arXiv:1010.3251].

[141] N. D. Christensen and C. Duhr, Comput.Phys.Commun. **180**, 1614 (2009), [arXiv:0806.4194].

[142] G. 't Hooft, Nucl.Phys. **B72**, 461 (1974).

[143] W. Kilian, T. Ohl, J. Reuter, and C. Speckner, JHEP **1210**, 022 (2012), [arXiv:1206.3700].

[144] J. Pumplin *et al.*, JHEP **0207**, 012 (2002), [arXiv:hep-ph/0201195].

[145] Z. Sullivan, Phys.Rev. **D70**, 114012 (2004), [arXiv:hep-ph/0408049].

[146] E. Boos, V. Bunichev, L. Dudko, V. Savrin, and A. Sherstnev, Phys.Atom.Nucl. **69**, 1317 (2006).

[147] G. P. Salam and J. Rojo, Comput.Phys.Commun. **180**, 120 (2009), [arXiv:0804.3755].

[148] S. Moch, J. Vermaseren, and A. Vogt, Nucl.Phys. **B688**, 101 (2004), [arXiv:hep-ph/0403192].

[149] A. Vogt, S. Moch, and J. Vermaseren, Nucl.Phys. **B691**, 129 (2004), [arXiv:hep-ph/0404111].

[150] V. Gribov and L. Lipatov, Sov.J.Nucl.Phys. **15**, 438 (1972).

[151] G. Altarelli and G. Parisi, Nucl.Phys. **B126**, 298 (1977).

[152] Y. L. Dokshitzer, Sov.Phys.JETP **46**, 641 (1977).

[153] M. Bahr *et al.*, Eur.Phys.J. **C58**, 639 (2008), [arXiv:0803.0883].

[154] P. Z. Skands, Phys.Rev. **D82**, 074018 (2010), [arXiv:1005.3457].

[155] CMS Collaboration, S. Chatrchyan *et al.*, JINST **3**, S08004 (2008).

[156] ATLAS Collaboration, G. Aad *et al.*, JINST **3**, S08003 (2008).

[157] M. Cacciari, G. P. Salam, and G. Soyez, JHEP **0804**, 063 (2008), [arXiv:0802.1189].

[158] P. Falgari, F. Giannuzzi, P. Mellor, and A. Signer, Phys.Rev. **D83**, 094013 (2011), [arXiv:1102.5267].

[159] J. M. Campbell and R. K. Ellis, (2012), [arXiv:1204.1513].

[160] J. Gao, C. S. Li, L. L. Yang, and H. Zhang, Phys.Rev.Lett. **107**, 092002 (2011), [arXiv:1104.4945].

[161] J. Drobnak, S. Fajfer, and J. F. Kamenik, Phys.Rev. **D82**, 114008 (2010), [arXiv:1010.2402].

List of Publications

Publications on the results presented in this thesis:

- F. Bach and T. Ohl, "Anomalous Top Couplings at Hadron Colliders Revisited," Phys. Rev. D **86** (2012) 114026 [arXiv:1209.4564 [hep-ph]].

Earlier publications:

- F. Bach and T. Ohl, "Discovery Prospects of an Almost Fermiophobic W' in the Three-Site Higgsless Model at the LHC," Phys. Rev. D **85**, 015002 (2012) [arXiv:1111.1551 [hep-ph]].

Talks given on various subjects of this thesis:

- ATLAS Kick-off Meeting "Wtb Vertex Combination", CERN phone conference (24.06.13);
- DPG-Frühjahrestagung 2013, Technische Universität Dresden (04.03.13);
- Terascale Alliance Annual Workshop 2012, DESY Hamburg (03.12.12);
- Terascale Alliance Workshop on Top Quark Physics 2012, Humboldt-Universität zu Berlin (23.03.12);
- DPG-Frühjahrestagung 2012, Georg-August-Universität Göttingen (27.02.12);
- Terascale Alliance Workshop on Top Quark Physics 2011, Bergische Universität Wuppertal (07.04.11);
- DPG-Frühjahrestagung 2011, KIT Karlsruhe (31.03.11).

Danksagung

Obwohl wir Doktoranden in Würzburg wie überall sonst zu stets gewissenhaftem und sachlich sauberem Arbeiten angehalten werden, ist es bei einer solchen Arbeit letztlich unvermeidlich, dass sich die erste Ungenauigkeit bereits auf der Titelseite findet: Denn dort steht notwendigerweise ein einziger Name, dessen Besitzer sich mit den folgenden Seiten um einen akademischen Titel bewirbt. Damit verbunden ist das Fehlen einer Vielzahl weiterer Namen, ohne die der erfolgreiche Abschluss zumindest dieser Dissertation zum scheitern verurteilt gewesen wäre. Mit dieser letzten Seite kann ich nur versuchen, die wichtigsten von ihnen zu erwähnen und ihnen damit meinen herzlichen Dank für ihre Hilfe und Unterstützung auszudrücken.

Zuallererst möchte ich meinem Betreuer Prof. Dr. Thorsten Ohl danken, der es mir überhaupt ermöglicht hat mich in dieses Thema zu stürzen, und mich über all die Jahre mit offenen Ohren, viel Zeit und unentbehrlichen Tipps und Diskussionen begleitet hat. Dazu gehört sicherlich auch die freundschaftliche und ungezwungene Atmosphäre in der Arbeitsgruppe, so dass auch deren (über die Jahre wechselnden) Mitgliedern mein Dank gebührt.

Weiterhin möchte ich Prof. Dr. Juan Antonio Aguilar-Saavedra für seine Zeit und Expertise dankbar erwähnen, die er während meines Forschungsaufenthaltes am IFCA in Santander aufgewendet hat, um unseren Code zu vergleichen und über verschiedene Aspekte meines Themas zu diskutieren. Auch Prof. Dr. Sven Heinemeyer gehört mein Dank für seine Einladung nach Santander sowie schöne Pincho-Abende. Da das Wort “Code” nun schon gefallen ist, möchte ich hier auch den WHIZARDlern für die angenehme Zusammenarbeit danken, vor allem Dr. Christian Speckner, der trotz seines Abschieds aus der Physik auch in dieser Danksagung nicht fehlen darf.

Ganz wichtig für meine Arbeit war natürlich auch die weitere Umgebung am Lehrstuhl sowie im Rahmen des Graduiertenkollegs GRK1147. Weit über den finanziellen Aspekt hinaus, war die lockere und freundschaftliche Gesellschaft meiner Mitstipendiaten und Bürogenossen oft erhellend, manchmal aber auch einfach eine tolle Ablenkung von den schlimmsten physikalischen Baustellen. An ganz anderer Stelle, nämlich Bürokratie und Papierkram, hat Brigitte Wehner für unentbehrliche Entlastung gesorgt.

Dieser letzte, aber sicher nicht unwichtigste Absatz ist all denjenigen gewidmet, deren Unterstützung ich mir außerhalb meiner fachlichen Probleme immer sicher sein konnte. Dazu gehören zuallererst meine Eltern Ralf und Gundela Bach, die mich zeit meines Lebens in allen Lagen und Entscheidungen bedingungslos unterstützt haben, aber auch meine Freundin Heide Kempf, die mich vor allem während der letzten stressigen Zeit geduldig ertragen und immer wieder aufgebaut hat. Zuletzt sollen hier auch meine engen Freunde, unter denen tatsächlich einige Physiker sind, Erwähnung finden, deren Beitrag zu dieser Arbeit hauptsächlich in der wohldosierten Ablenkung von derselben bestand: Danke SB, FF, AH, HK, SK, PM, MO, LP, JS, MS, MW.